



**HAL**  
open science

# Self-Assembly of Colloidal Semiconducting Nanoplatelets

Benjamin Abécassis

► **To cite this version:**

Benjamin Abécassis. Self-Assembly of Colloidal Semiconducting Nanoplatelets. Soft Condensed Matter [cond-mat.soft]. Université Paris Sud Orsay, 2016. tel-01564412

**HAL Id: tel-01564412**

**<https://hal.science/tel-01564412v1>**

Submitted on 18 Jul 2017

**HAL** is a multi-disciplinary open access archive for the deposit and dissemination of scientific research documents, whether they are published or not. The documents may come from teaching and research institutions in France or abroad, or from public or private research centers.

L'archive ouverte pluridisciplinaire **HAL**, est destinée au dépôt et à la diffusion de documents scientifiques de niveau recherche, publiés ou non, émanant des établissements d'enseignement et de recherche français ou étrangers, des laboratoires publics ou privés.

THÈSE D'HABILITATION À DIRIGER LES RECHERCHES  
DE L'UNIVERSITÉ PARIS SUD

Présentée par

**Benjamin ABÉCASSIS**

**Auto-assemblage de Nanoplaquettes Colloïdales Semiconductrices**

**Self-Assembly of Colloidal Semiconducting Nanoplatelets**

Défendue le 7 juin 2016

devant le jury composé de:

M. Franck ARTZNER	Rapporteur
M. Érik DUJARDIN	Rapporteur
M. Stephan FÖRSTER	Rapporteur
M. Benoit DUBERTRET	Examineur
M. Peter REISS	Examineur
M. Jonathan OWEN	Examineur
Mme. Odile STÉPHAN	Présidente du Jury





# Contents

<b>1</b>	<b>Introduction and state of the art</b>	<b>5</b>
1.1	Colloidal nanocrystals	6
1.2	Quantum confinement	7
1.3	Interband absorption, excitons and photoluminescence	9
1.4	Colloidal semi-conducting nanoplatelets	10
1.5	Colloidal forces between semi-conducting colloidal nanocrystals	14
1.6	Optical coupling between Nanoplatelets	24
<b>2</b>	<b>Colloidal stability and stacking of colloidal CdSe nanoplatelets</b>	<b>27</b>
2.1	Stability of quantum well dispersions	27
2.2	Structure of the precipitate	29
2.3	Stability criteria	31
2.4	Effect of oleic acid concentration	32
2.5	Effect of water on the colloidal stability	33
2.6	Stabilization by polymers	34
2.7	A dipole moment in the nanoplatelets ?	36
2.8	Effect of self-assembly on optical properties	36
2.9	Conclusion	38
<b>3</b>	<b>Self-assembly of CdSe nanoplatelets into anisotropic superparticles</b>	<b>39</b>
3.1	Introduction	39
3.2	Results and discussion	40
3.3	Conclusion	45
<b>4</b>	<b>Hybrid polymer nanoplatelet films</b>	<b>47</b>
4.1	Introduction	47
4.2	Results and discussion	47
4.3	Conclusion	52
<b>5</b>	<b>CdSe Nanoplatelets Polymers</b>	<b>55</b>
5.1	Introduction	55
5.2	Results and discussion	55

5.3	Conclusion	63
<b>6</b>	<b>Twisted Threads</b>	<b>65</b>
6.1	Formation and structure of twisted threads	65
6.2	Formation mechanism	68
6.3	Twisting of individual nanoplatelets	68
6.4	Discussion	71
6.5	Conclusion	73
	<b>Bibliography</b>	<b>75</b>
<b>A</b>	<b>Experimental techniques</b>	<b>85</b>
A.1	Syntheses	85
A.2	Small Angle X-ray Scattering	87
A.3	Electron microscopy	87
A.4	Other technical details	88
<b>B</b>	<b>Curriculum vitae</b>	<b>89</b>

## Introduction and state of the art

This manuscript presents part of my work since my recruitment as a CNRS research associate at the Laboratoire de Physique des Solides in Orsay. A part of my research project when i arrived at LPS was on the self-assembly of colloidal semiconducting nanoplatelets which (at the time) had been discovered two years earlier in B. Dubertret's lab by Sandrine Ithurria. Hence, i started to work in close collaboration with Benoit's group and learned how to synthesize these fascinating objects with the help of two graduate students (M. Tessier and C. Bouet). The initial goal was to make colloidal liquid crystals with these platelets in the fashion of what had previously been achieved at LPS on clays or goetite nanorods. However, these organized phases require an important volume fraction in nanocrystals (commonly tens of percent) which was difficult to achieve with the current synthesis methods. We also quickly realized that colloidal stability issues would prevent us from reaching this goal in the short term. Nevertheless, we noticed that these platelets had a strong tendency towards stacking and tried to better understand and to control this stacking. The main part of this manuscript is dedicated to our efforts towards this goal. We drew our inspiration from the literature available on CdSe nanorods and spheres to craft self-assembly schemes adapted for nanoplatelets. In this endeavor, I have been lucky enough to collaborate with Santanu Jana who arrived as a post-doc in january 2014. He has performed most of the experiments presented in chapters 2, 5 and 6. The work on the nanoplatelets/polymer composite (chapter 4) is a collaboration with Emmanuel Beaudoin, associate professor at Paris-Sud.

The manuscript organizes as follows. In this introduction, i give an overview of the basic knowledge on quantum dots and nanoplatelets necessary to follow the rest of the manuscript. I recall the basics on quantum confinement, colloidal nanocrystals and the specificities of colloidal quantum wells. Then, i review the forces acting between colloidal nanocrystals which lead to their self-assembly. This part has been written in the context of an invited mini-review article on the self-assembly of semi-conducting nanocrystals published recently in a special issue of ChemPhysChem dedicated to quantum dots [1]. The second chapter deals with the colloidal stability of colloidal quantum wells and is adapted from a recent publication [2]. Chapters 3 to 7 describe our

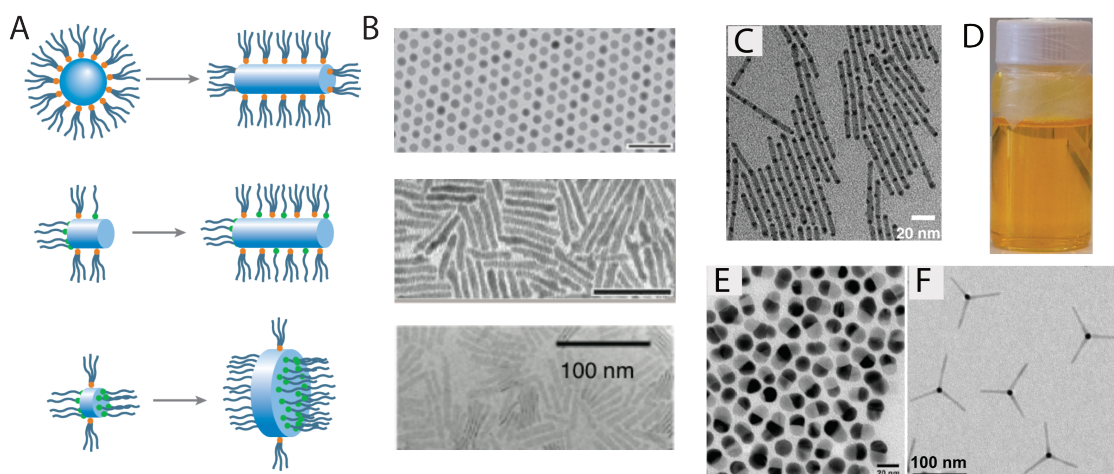


**Figure 1.1:** A. Schematic representation of colloidal nanocrystals: spheres, rods and platelets from top to bottom (from [5]). B. Electron microscopy of the corresponding shapes. C. and E. Multicomponent nanostructures. D. dispersion of colloidal nanocrystal in hexane. E. Nano-tetrapods.

recent work on the self-assembly of colloidal nanoplatelets into different kind of superstructures, from anisotropic supra-particles to (twisted) threads. Chapters 3 and 4 have already been published [3, 4] while chapters 5 and 6 have not appeared in the literature yet. Finally, i describe the main research direction in which i intend to work in a near future.

## 1.1 Colloidal nanocrystals

Colloidal nanocrystals can be defined as solution grown inorganic crystals with one dimension below 10 nm and covered with a mono-layer of surfactant bound to its surface (Figure 1.1). The inorganic core provides the colloidal nanocrystals with size dependent physical properties while the surfactant mono-layer makes them dispersible in common organic solvent. Research on these objects has been triggered by the discovery of solution synthesis using organo-metallic precursors. The high temperature (between 100 and 300 °C) reaction of precursors in the presence of surfactant such as long chain amines, carboxylic acids or phosphorous compound, allows the formation of monodisperse nanocrystals. Often, the size distribution has a relative standard deviation below 10% and can sometimes reach values lower than 5%. This kind of chemistry has initially been crafted for semi-conducting materials such as CdSe [6] but has proven efficient in the synthesis of a wide range of other materials like metals, metal oxides, fluorides etc... Since then, a new branch of chemistry, blending organometallic chemistry and materials science has emerged whose goal is to synthesize such nanocrystals with the highest control possible in terms of shape and size monodispersity or yield. The synthesis of these nanoparticles usually takes place in high-boiling point organics solvents such a

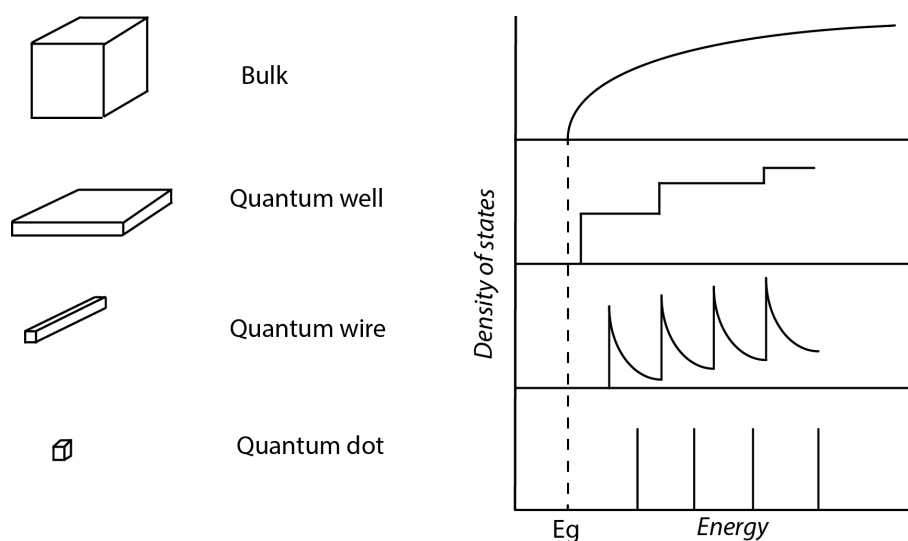


Figure 1.2: Schematic representation of quantum dots, wire and well. The typical shape of the density of states function for electrons in the conduction band for a semiconductor with band-gap  $E_g$  is represented for the three types of confined structures.

octadecene, hexadecene. A typical experimental set-up involves a round-bottom flask connected to a condenser and a schlenk-line. The flask is equipped with a temperature controller, a magnetic stirrer and precursors can be injected in the reacting medium at different stages of the reaction. After the synthesis, the nanocrystals are purified through precipitation-redispersion cycles. An antisolvent (usually an alcohol) is added to the crude product which makes the nanocrystals precipitate while the byproducts remain in solution. After centrifugation, the nanocrystals are redispersed in an organic solvent and precipitated again for further washing. This cycle is repeated until the desired degree of purity is achieved. This purification cycles can have an effect on the density and composition of the ligand brush.

This manuscript is focused on semiconductor colloidal quantum dots which exhibit fascinating optical properties due to a quantum confinement, in the following, we detail the physical principles underlying this effect.

## 1.2 Quantum confinement

When a solid reaches dimensions sufficiently small, new physical properties can appear which depend on the extent of this confinement [7]. This is the case for semi-conducting materials whose optical properties change when the size of the crystal reaches nanometric dimensions. This effect is called “quantum confinement” since it is of pure quantum origin. The Heisenberg uncertainty principle states that when a particle is confined to a region  $\Delta x$  of the  $x$  axis in space, its momentum can not be known with arbitrary

precision. If the uncertainty on the momentum is  $\Delta p_x$ , a formal inequality follows:

$$\Delta p_x \geq \frac{\hbar}{\Delta x}. \quad (1.1)$$

Hence, for a particle of mass  $m$ , a confinement in the  $x$  direction gives an additional energy ( $E_c$ ) of:

$$E_c = \frac{(\Delta p_x)^2}{2m} \sim \frac{\hbar^2}{2m(\Delta x)^2}. \quad (1.2)$$

The energy induced by the confinement will only be noticeable if it is of the same order of magnitude as the thermal energy i.e.  $1/2k_b T$ . This yields an order of magnitude of the dimension over which the quantum confinement starts to be significant:

$$\Delta x \lesssim \sqrt{\frac{\hbar^2}{mk_b T}}. \quad (1.3)$$

For an electron in a semi-conductor, the typical effective mass is  $0.1m_0$  where  $m_0$  is the mass of an electron at rest ( $9.11 \times 10^{-31}$  kg). With  $\hbar = 1.05 \times 10^{-34}$  J.s and  $kT = 4.11 \times 10^{-21}$  J, this yields a typical  $\Delta x$  value of **5 nm**.

The properties of the confined material and its precise band-structure will depend on the number of dimensions over which the material is confined. Three types of quantum-confined structures can be produced with a confinement in 1, 2 or 3 dimensions. They have been named accordingly quantum wells, quantum wires and quantum dots (Figure 1.2). In the bulk, the density of state is proportional to  $(E - E_g)^{1/2}$ . In the case of confined structures, the band-edge is shifted to higher energies due to the quantum confinement energy and the functional form of the density of states is completely changed. It is beyond the subject of the manuscript to go provide a complete mathematical description of the energy levels in these confined structures, however we can describe qualitatively the shape of the density of states in the case of quantum wells and dots.

In the case of quantum wells, it is possible to show that the density of states of the electrons in the valence band does not depend on the energy. Hence, the density of state versus energy curve is just a step function with jumps at every quantized level of the energy. By solving the Schrödinger equation for an infinite potential well, it is possible to show that the energy levels are given by:

$$E_n = \frac{\hbar^2}{2m^*} \left( \frac{n\pi}{d} \right)^2, \quad (1.4)$$

where  $n$  is an integer corresponding to the energy level number,  $d$  is the thickness of the quantum well and  $m^*$  is the effective mass of the particle.

In quantum dots, the motion is quantized in all three directions and no continuous band is visible in the. These particles behave like artificial atoms in which the electrons have discrete energies in contrast to bands as observed in the solid state. The density of states consists of a series of Dirac  $\delta$ -functions at the quantized level.

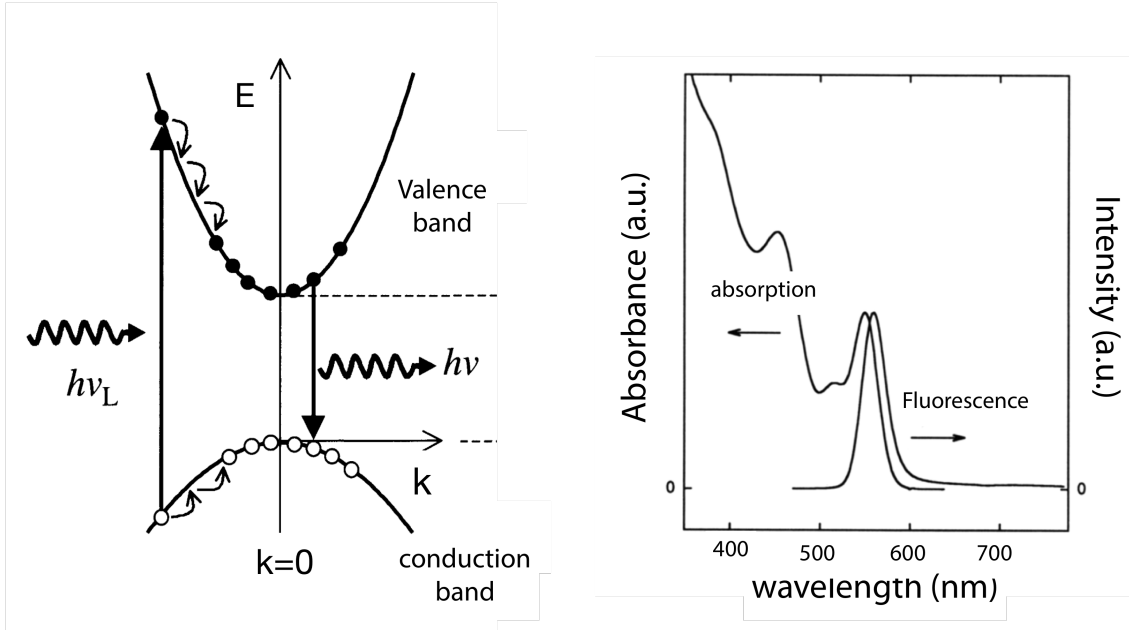


Figure 1.3: Left: Simplified schematic diagram of the processes occurring in a direct gap semiconductor when a photon of energy  $h\nu_L$  is absorbed, populating the valence band and creating a hole in the conduction band. Both the electron and the hole relax through thermalization and a photon is emitted. Right: Typical absorption and emission spectra for a quantum dot.

### 1.3 Interband absorption, excitons and photoluminescence

Like in any other semiconductor, electrons in quantum dots interact with light through a series of physical phenomena leading to valuable properties. As described in Figure 1.3, a photon with energy larger than the band gap can be absorbed through the interaction with an electron, creating an exciton, i.e. an electron/hole pair. The transition rate between these two electronic states is given by the Fermi golden rule:

$$W_{i \rightarrow f} = \frac{2\pi}{\hbar} |M|^2 g(\hbar\omega) \quad (1.5)$$

where  $M$  is the matrix element describing the photon/electron interaction and  $g(\hbar\omega)$  is the density of states. Both the electron, now in the valence band, and the hole will relax towards the bottom (or top) of their band through interactions with phonons. This thermalization process is very fast and usually occurs within 100 fs. Once at the top (bottom) of their bands, holes (electron) must wait to recombine through the emission of a photon with energy close to the band gap or through non-radiative pathways (such as Auger recombination or coupling with surface trap states). The efficiency of the radiative recombination can be measured through the quantum yield and is linked to the radiative lifetime which is of the order of a nanosecond in the case we are interested in. Experimentally, these processes can be probed by absorption and emission spectroscopy.



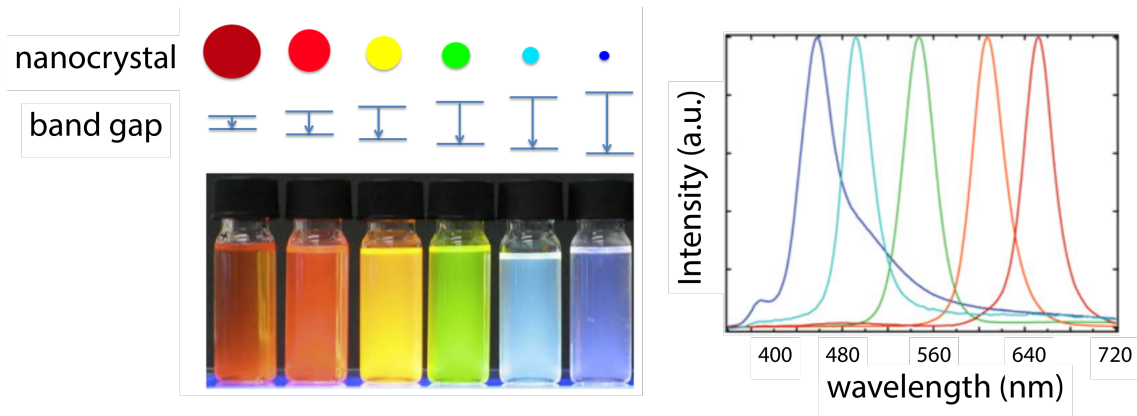


**Figure 1.4:** Left: evolution of the quantum dots band gap as a function of their size, photograph showing the glowing fluorescence of quantum dots under UV illumination. Right: emission spectra of quantum dot of varying size from 2 to 5 nm.

Figure 1.3 shows the typical absorption and emission spectra of a dispersion of quantum dots. Starting from low energy photons, the absorbance is close to zero from the infrared until the band-gap energy is reached. Then, photons start to be absorbed and the absorbance increases as the wavelength decreases. The features visible in the absorption spectra are the signature of the fine band structure of the quantum dots. The emission spectra exhibits a single peak corresponding to the recombination of band-edge excitons.

As explained in the previous paragraph, a quantum confinement effect leads to the increase of the band gap in semiconductors. The emission wavelength is thus directly related to the size of the quantum dots. For CdSe, the bulk band gap is 1.74 eV (corresponding to a wavelength of 712 nm). As the size of the particle decreases, the band gap increases and the emission wavelength shifts through the visible spectrum from the red to the ultra-violet (Figure 1.4).

The width of the emission line is related to two distinct effects. First, the polydispersity of the quantum dots can induce a broadening of the emission line since the emission wavelength is directly related to their size. Second, thermal agitation authorizes electrons to have energy levels higher than the ground state in the conduction band. This leads to a dispersion in the emitted photon energy directly linked to temperature. The observed width of the line results from the largest of the two dispersions.

## 1.4 Colloidal semi-conducting nanoplatelets

Semi-conducting nanoplatelets have recently been discovered [8–10]. They are the colloidal equivalent of epitaxial quantum wells, studied a lot in the 90's (mostly of the III-VII semiconductor family), which are still of great applicative interest for lighting devices. They are also called colloidal quantum wells in the literature. These nanoplatelets (NPL) are 2D nanocrystals with thicknesses ranging from 0.5 to 2 nm and lateral di-

Peak position (nm)	Structure	number of monolayers	designation	Thickness (nm)
394	3Cd-2Se	2.5	2ML	0.6
463	4Cd-3Se	3.5	3ML	0.9
512	5Cd-4Se	4.5	4ML	1.2
552	6Cd-5Se	5.5	5ML	1.5

Table 1.1: Structural and spectroscopic characteristics of zinc-blende nanoplatelets.

mensions one or two orders of magnitude larger. CdSe, PbS, ZnS Both wurtzite and zinc-blende NPL can be synthesized depending on the ligand and reaction temperature. Zinc-blende platelets [11, 12] are obtained with carboxylic acid ligands and temperatures ranging from 150 to 240 °C while amines and lower temperatures yield wurtzite type particles [13–16].

In the present manuscript, we focus on zinc blende colloidal NPL. A striking feature of these nanoparticles is the ability to control their thickness at the atomic level. Several electron microscopy studies and recent X-ray diffraction experiments have shown that NPL have their large dimension perpendicular to the [001] direction of the lattice with flat cadmium planes terminating the particle at the top and bottom. The carboxylic acid ligands are linked to the cadmium atoms *via* X-type ligand-metal bond [17–19]. Atomic models showing the structure of these nanoplatelets are shown in Figure 1.5.

Since the quantum confinement only occurs in the thickness direction, the band gap and hence the electronic band structure solely depends on that dimension. Theoretical calculations have shown that, in the case of CdSe, important shifts (tens of nanometers) are observed in the band gap luminescence when the thickness is changed by just one atomic layer. Furthermore it is possible to obtain through proper synthesis and purification, colloidal dispersion containing only one population of NPL of a given thickness. In this respect, nanoplatelets share similarities with atomically defined particles such as polyoxometallates or magic size clusters. This is easily assessed by UV-VIS spectroscopy. Their absorbance spectra have very sharp features whose position depend on the NPL thickness (Figure 1.6). The thinnest NPL which can be synthesized using this chemistry has its first excitonic feature in the absorbance spectrum at 394 nm (table 1.1). This class of NPL is difficult to image with an electron microscope due to their small thickness and have a low quantum yield. The next population in thickness, emitting at 463 nm, can yield very extended NPL which roll into tubes along the [110] direction [20]. Thicker NPL, emitting at 512 and 552 nm have the greatest quantum yield (which can be as high as 50%) and have been used in most of the recent work on the optical properties of NPL [21–24]. Their thickness is respectively 1.2 and 1.5 nm and their lateral extension ranges between 10 and 30 nm.

The correspondence between the absorbance spectra and the thickness of the NPL have been the subject of conflicting reports in the literature. The first reports were based

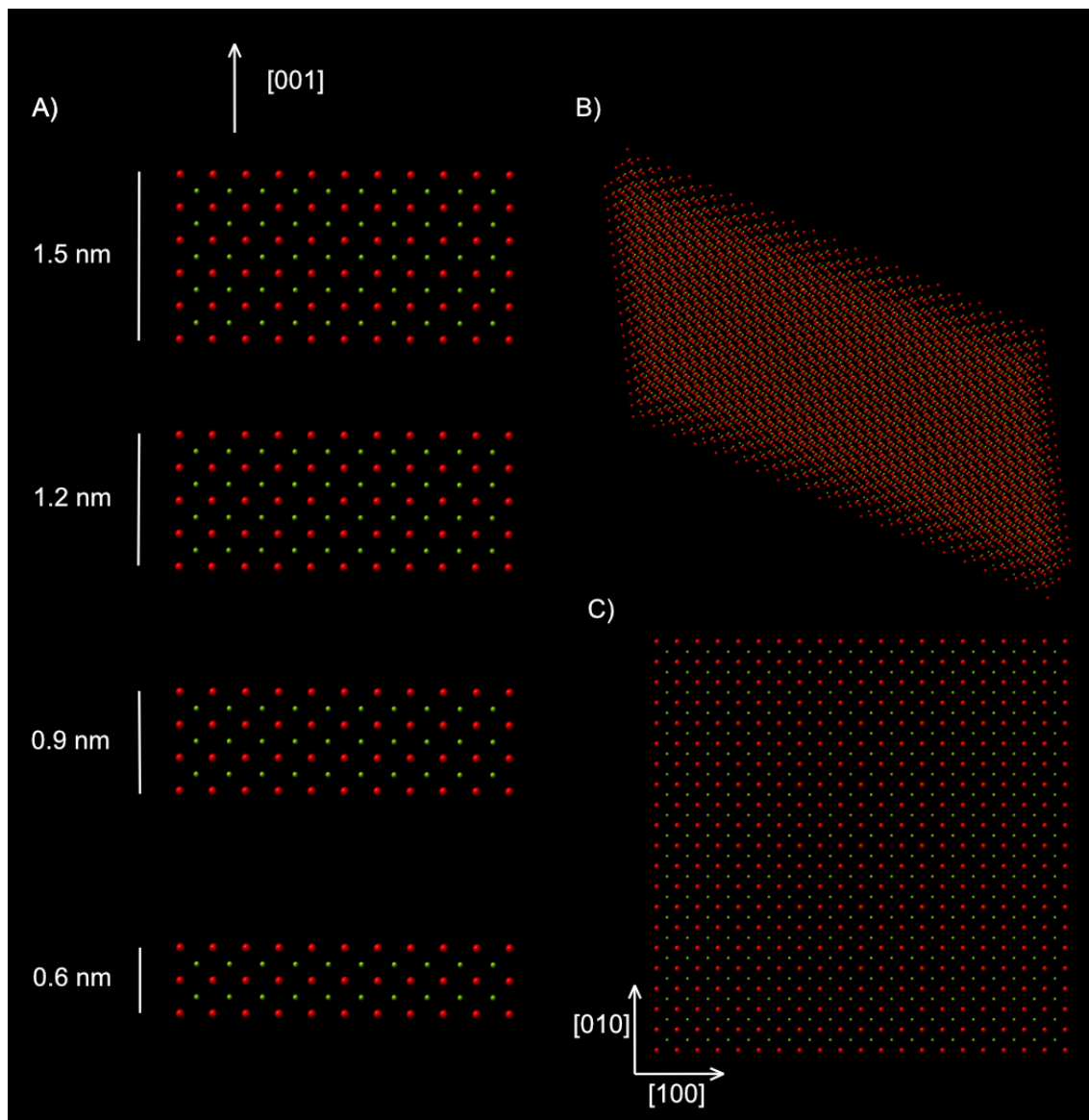
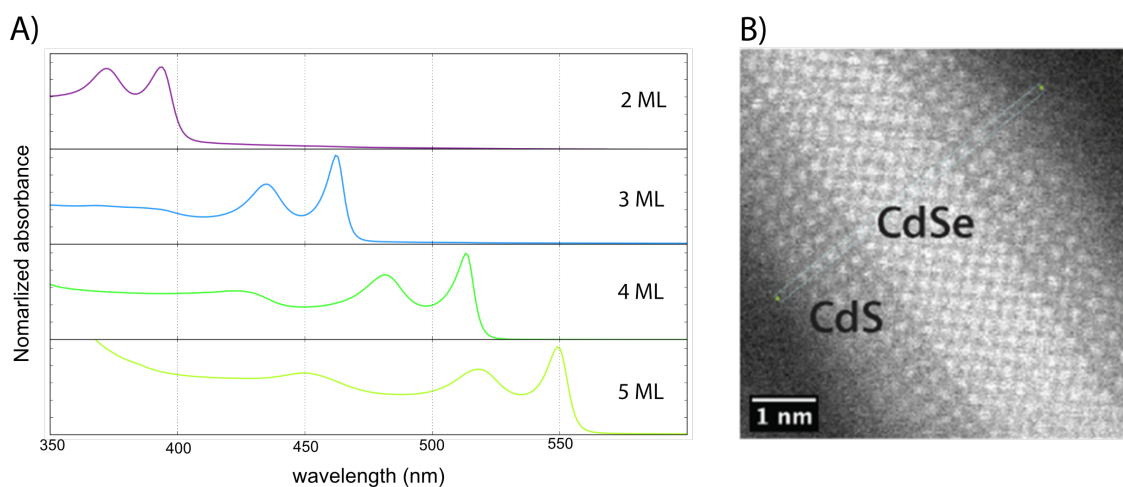


Figure 1.5: Atomistic models of colloidal CdSe quantum wells. A) quantum wells of different thicknesses with a side view angle perpendicular to the [001] direction. B) view with a C) view from the top perpendicular to the plane of the platelet.



**Figure 1.6:** A) Absorbance UV-VIS spectra of colloidal nanoplatelets with increasing thickness from top to bottom. The sharpness of the excitonic features are due to the atomic level control of the C NPL thickness. B) HAADF-STEM image of a CdSe-CdS core shell nanoparticles where atoms can be counted. The picture was taken by G. Patriarche at LPN, Marcoussis.

on theoretical calculations which linked the optical transition energies to the thickness through confined electron models. These models use constants of bulk CdSe to calculate the thickness and predicted a 7 monolayers structures (2.1 nm thickness) for the thicker platelets emitting at 552 nm. The model also predicted that the other populations were separated by one Cd-Se unit. A direct measurement of the number of atoms in a single platelet by electron microscopy is difficult since one has to find a perfectly oriented particle along the electron beam. A very high resolution is also necessary. High angle annular dark field scanning electron microscopy (HAADF-STEM) images of core/shell CdSe/CdS nanoplatelets were obtained and enabled the absolute determination of the CdSe core atomic composition. The platelets emitting at 552 nm were found to be 1.5 nm thick with a 5 monolayers structures as presented in the table above. These values have recently been confirmed by X-ray diffraction.

All the synthesis of zinc-blende colloidal nanoplatelets published so far involves the use of cadmium acetate as a precursor. Its role in the anisotropic growth is not clear yet and is the subject of current studies. An increase of temperature synthesis yields thicker platelets. While 2ML NPL can be synthesized at temperatures as low as 130 °C, 5ML NPL are usually made at 240 °C. It is important to note that 2 or 3 populations of NPL (and often quantum dots) are present in solution at the end of a synthesis. Since 3ML NPL are more extended laterally, they are heavier and hence can be easily separated by centrifugation. Platelets and dots are separated using selective precipitation. Since they do not have the same colloidal stability, upon addition of an antisolvent, the NPL precipitate earlier while quantum dots remain in solution. After centrifugation, the solvent containing quantum dots can be discarded while the NPL can be redispersed. Detailed

synthesis protocol of the NPLs used in this work are described in the experimental section at the end of this manuscript.

## 1.5 Colloidal forces between semi-conducting colloidal nanocrystals

This section is adapted from an invited review article [1] whose topic was the self-assembly of colloidal semi-conducting nanoparticles in general (including rods and spheres). We present here a modified shortened and updated version.

The field of supra-molecular chemistry has fueled impressive progresses at the interface of chemistry, biology and physics by enabling the synthesis of complex structures whose shapes are encoded at the molecular level [25, 26]. Synthetic chemistry of colloidal nanocrystals has expanded in recent years and the degree of control achievable over the structure of nanocrystals is truly remarkable. Self-assembly of colloidal nanocrystals is a route towards larger architectures composed of nanoparticles as building blocks. The ambition in trying to self-assemble nanocrystals is to exploit their size depend physical properties in devices or to forge new collective properties through short-range interactions such as plasmon coupling or exciton transfer.

Previously, other reviews have dealt with self-assembly of (colloidal) nanocrystals and the reader should refer to these papers for a wider perspective on this topic [27–33]. Other reviews are focused on specific topics such as one dimensional nanocrystals [34], nanoparticle-polymer composites [35, 36], applications in solar cells [37, 38], lead chalcogenide nanocrystals [39] or charge transport in self-assembled nanostructures [40].

We start by describing the different inter-particle forces acting in the self-assembly process of nanocrystals. The basic understanding and experimental validation of these potentials is a pre-requisite for predictive design of new nanoparticles-based assemblies [41]. Most of the time, these forces have been thoroughly described in the past for colloidal particles which are one to two orders of magnitude larger. However, some specificities to the nanoscale exists. Most of the simplifying assumptions which are valid for large colloids break down when the size of the particles reaches the nanometer scale. For example, a classical assumption is to consider the solvent as a continuum. This is not realistic for nanoparticles in long chain alkanes. This specificities to the nanoscale are described in details in a recent review [42].

### 1.5.1 Dipole-dipole interaction

In semi-conducting nanoparticles, an inhomogeneous repartition of the electrons within the material can yield to a permanent dipole. This can have important consequences on the spectroscopic properties of the nanocrystals since electronic transitions forbidden by symmetry are allowed if the nanocrystals are not centro-symmetric. Such parity-forbidden transitions have been observed in CdSe nanocrystals and were explained by the presence of a permanent dipole [43]. Following these findings, screened dipole moment comprised between 20 and 100 Debye were measured through impedance measurements of a concentrated colloid's complex dielectric constant [44, 45]. Surprisingly, a significant

dipolar moment was also measured in ZnSe nanoparticles whereas, contrary to wurtzite, their zinc-blende structure is not polar and exhibit an inversion symmetry center [45]. Different physical explanations have been provided such as a small shape asymmetry, surface strain induced by ligands causing a distortion of the lattice at the liquid-solid interface [46] or surface localized charges due to dangling bonds. Simple orders of magnitude calculations yield dipole values and trends consistent with experiments in the case of surface localized charges [45]. More recently, semi-empirical quantum calculations [47] showed that truncations of regular tetrahedral CdS nanocrystal could yield dipole moment comprised between 50 and 100 D, similar to experimentally measured values.

In wurtzite CdSe nanorods, a very large dipolar moment comprised between 100 and 200 D has been measured in solution by transient electric birefringence [48]. Measurements on different nanorod samples with varying dimensions showed that the dipolar moment scales linearly with nanocrystal volume. Small crystallographic deviations from the ideal wurtzite structure explains the origin, the magnitude and the trend observed in experiments [49]. In the case of PbSe nanocrystals, the growth mechanism induces a non-centrosymmetric distribution of the polar {111} facets and hence a dipolar moment larger for small spherical nanoparticle than for larger nanocubes which are almost symmetric [50]. This large dipolar moment induces a strong attraction between the PbSe nanocrystals during their formation and their oriented attachment yielding long, anisotropic PbSe nanowires [51].

Such large dipolar moments affect the interaction between nanoparticles through dipolar coupling. The interaction potential between two dipoles of moment  $\mu$  separated by a distance  $r$  is given by [52]:

$$V_{dipole} = -\frac{\mu^2}{4\pi\epsilon_0\epsilon r^2} [2\cos\theta_1\cos\theta_2 - \sin\theta_1\sin\theta_2\cos\phi], \quad (1.6)$$

where the orientation of the dipoles are given in Figure 1.7.

This equation shows that the attraction is maximum when the two dipoles are lying in line for a given  $r$ . However, depending on the relative orientation of the dipole inside the nanoparticle, the configuration where the two dipoles are parallel can also be favored. As a matter of fact, if the parallel configuration is higher in energy at a given  $r$ , steric constraint can authorize smaller  $r$  values in the parallel configuration. This is the case, for example, if the dipole is oriented along the high dimension of a rod: orienting the rods in a parallel orientation enables closer contact and hence a smaller  $r$  value.

It is important to notice that while these dipolar interaction are usually neglected in the case of large colloids, they play an important role in semi-conducting nanocrystals. As already pointed out by Rabani *et al.* [53], dipole-dipole interactions scale like  $r^{-3}$  whereas van der Waals interactions decay much more rapidly ( $r^{-6}$ ). In this respect, nanocrystals are closer to molecules, which often hold a permanent dipole, than to colloidal particles. Talapin *et al.* have indeed shown that dipole-dipole interactions could explain the rich phase diagram observed in some nanocrystal superlattices [51]. In particular, non closed-packed simple hexagonal superlattice can not form in hard-spheres



systems. Analytical calculations [54] confirmed that clusters having original geometries such as planar, tubular or Mobius could be observed in systems of dipolar spheres with weak van der Waals coupling.

### 1.5.2 van der Waals interactions

van der Waals forces, also called London dispersion forces have been extensively studied in the past [55]. Their physical origin lies in the induced dipole-induced dipole interactions present in every material. Qualitatively, even if an atom or a molecule has no net time-average dipole, an instantaneous dipolar moment is always present due to the movement of the electrons around the nucleus [52]. This instantaneous dipole creates a field which will affect the surrounding and induce a net attractive force. At long distances, the van der Waals forces are dominated by semi-conductor/semi-conductor interaction through the solvent. The general form of the interaction is given by the Hamaker pairwise summation:

$$V_{vdw}^{ij} = -\frac{A}{\pi^2} \int_{V_i} \int_{V_j} \frac{1}{r^6} d\vec{r}_i d\vec{r}_j, \quad (1.7)$$

where  $A$  is the Hamaker constant and  $V_{i,j}$  are the volumes of the particles. In the general case, the integration has to be performed numerically but analytical expressions can be found for classical geometries. The interaction potential depends on the geometry of the nanoparticles and on the Hamaker constant of the material (1) considered through the solvent (2). In the case of identical particles interacting through a solvent, this constant ( $A_{121}$ ) can be calculated through a combining relation [52]:

$$A_{121} \simeq \left( \sqrt{A_1} - \sqrt{A_2} \right)^2. \quad (1.8)$$

The Hamaker constant for semi-conducting nanoparticles are not known exactly and depend on their precise structure. In general, they are not the same as the Hamaker constant of the bulk material. In any case, even the bulk Hamaker constant for the materials where are interested in have never been published to the best of our knowledge. An exception is CdS, whose Hamaker constant is  $11 \times 10^{-20}$  J as quoted in ref [56]. This value is quoted in several publications as the more precise value available for CdSe [57]. Rabani calculated theoretically the value of the Hamaker constant for CdSe as an application of a new interatomic pair potential for this material [53] and found 0.388 eV i.e.  $6.21 \times 10^{-20}$  J. Hence, for a CdSe nanocrystal in an apolar solvent such as hexane (for which the Hamaker constant is  $3.8 \times 10^{-20}$  J), we found  $A_{121} = 1.87 \times 10^{-20}$  J with the bulk Hamaker constant of CdS and  $0.3 \times 10^{-20}$  for the value calculated by Rabani.

For two flat plates, following the notations described in Figure 1.7, the interaction potential per area unit is given by:

$$V_{vdw}^{\text{plates}} = -\frac{A_{121}}{12\pi d^2}, \quad (1.9)$$

where  $d$  is the distance between the plates.

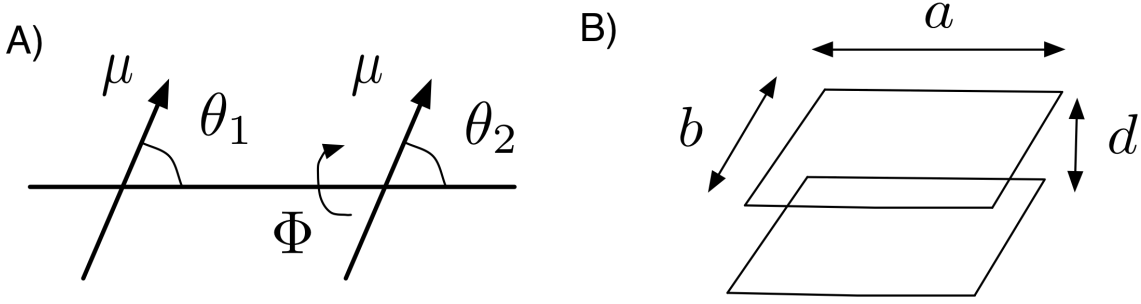


Figure 1.7: Notations used for the description of the different interactions: A) dipolar interaction B) van der Waals interaction in the plate geometry

In the case of two rectangles of length  $a$  and width  $b$  separated by a distance  $d$  where  $d \ll \ell$ , the thickness of the rectangle, the van der Waals potential is given by:

$$V_{vdw} = -\frac{A_{121}\ell^2}{\pi^2} \mathcal{F}(d; a, b), \quad (1.10)$$

where:

$$\begin{aligned} \mathcal{F}(d; a, b) = & \left[ \frac{bd^2 + 2a^2b}{2d^4(d^2 + a^2)^{1/2}} \right] \tan^{-1} \left[ \frac{b}{(d^2 + a^2)^{1/2}} \right] \\ & + \left[ \frac{d^2 + 2ab^2}{2d^4(d^2 + b^2)^{1/2}} \right] \tan^{-1} \left[ \frac{b}{(d^2 + b^2)^{1/2}} \right] \\ & - \frac{b}{2d^3} \tan^{-1} \left( \frac{b}{d} \right) - \frac{a}{2d^3} \tan^{-1} \left( \frac{a}{d} \right). \end{aligned} \quad (1.11)$$

### 1.5.3 Electrostatic interaction

Electrostatics are known to be an important force governing self-assembly of nanoparticles [58]. However, these interactions are less well studied in non-polar solvent. This topic has essentially been considered for its applicative relevance in various domains such as ink jet printing or safe petroleum processing. Two thorough reviews have been dedicated to this subject [59, 60] and i will only describe here the most important points. In polar media, charges dissociate easily due to the high dielectric constant ( $\epsilon \simeq 80$  for water). A quantity of interest to consider in this respect is the Bjerrum length  $\lambda_b$  which is the distance between two unit charges where their Coulomb energy equals the thermal energy  $kT$ :

$$\lambda_b = e^2 / 4\pi\epsilon_0\epsilon kT. \quad (1.12)$$

In water (at 25°C), the Bjerrum length is only 0.72 nm. In contrast, it reaches 30 nm for hexane. This shows that charges do not dissociate easily in non-polar media and that the energetic barrier to overcome in order to tear apart too opposite non-polar media is



40 larger in hexane than in water. In fact, it is possible to show that the solubility of a 1:1 electrolyte in a solvent scales like  $\exp(-\lambda_b)$  [52]. However, the difficulty of solute to dissolve in low dielectric permittivity media does not imply that charges are absent and that we should ignore these effects in the theoretical treatment of interaction potential between colloidal nanoparticles. On the contrary, charges may have an important effect on the colloidal stability and self-assembly of nanocrystals. A direct consequence of the scarcity of charges is the lack of screening of electrostatic interaction. The Debye length is directly proportional to the Bjerrum length and quantifies the length-scale over which a counterion cloud is perturbed by a charged surface:

$$\chi^{-1} = \ell_b = \sum_i (4\pi\lambda_B\rho_\infty z_i^2)^{1/2}, \quad (1.13)$$

where  $\rho_\infty$  is the ion concentration far from the surface and  $z_i$  is the ion valence. In aqueous media, the Debye length can be tuned by adding salt from 30 nm (for  $10^{-4}$  M in NaCl) to a fraction of nm (for 1M in salt) whereas in apolar solvent,  $1/\chi$  is usually two orders of magnitude larger and ranges from 1 to 100  $\mu\text{m}$ . Hence, charges are rare but they are very weakly screened meaning that even a small quantity of charges will have effects over large distances. Moreover, this low screening length induces a very small double-layer capacitance. In other terms, a small amount of charge will generate significant surface potentials. For example, surface potentials of -140 mV have been measured in non-aqueous 800 nm colloids with only 200 to 900 electrons [61]. This represents a charge density of  $-4 \cdot 10^{-6}$  C  $\text{m}^{-2}$ , almost five orders of magnitude smaller than the charge density necessary to reach such a high potential in a  $10^{-2}$ M NaCl aqueous solution. Hence, even if charge are not numerous, they induce large surface potentials and act over long distances which makes them play an important role in the self-assembly of nanocrystals.

More quantitatively, if we consider an isolated spherical particle of radius  $a$  and charge per surface area  $\sigma_0$ , the  $\zeta$ -potential induced by this charge is given by:

$$\sigma_0 = \epsilon\epsilon_0\zeta/a. \quad (1.14)$$

This expression is valid for isolated particles and hence at extreme dilution where double-layers of several nanoparticles do not overlap. This highlights one of the difficulties when dealing with electrostatic in non-polar media: the break-down of the thin-double layer limit:  $\chi a \gg 1$  where  $a$  is the particle size. This approximation simplifies a lot the mathematical treatment of electrostatic equations. Furthermore, the nanocrystals we are interested in are small compared to classically studied colloids. Hence, we are always situated in the thick double-layer regime:  $\chi a \ll 1$ . Another consequence of the large Debye length is that we can rarely consider that nanoparticles are independent since the double-layers of several nanoparticles are inter-penetrating. Unless very high dilutions are considered, individual properties of nanoparticles depend on first or even second neighboring nanoparticles. Electrostatics in colloidal nanocrystals is hence in the **large and overlapping Debye layers regimes** and one has to be very careful one using classical theories in electrostatics that they are still valid in this regime. This is often not the case.

A critical volume fraction  $\Phi_0$  over which a double-layer overlap occurs can be calculated following Dukhin *et al.* [62]:

$$\Phi_0 \simeq \frac{0.52}{\left(1 + \frac{1}{\kappa a}\right)^3}. \quad (1.15)$$

The electrophoretic mobility of a colloid in a solvent is given by:

$$\mu = \frac{\zeta \epsilon \epsilon_0 f(\kappa a)}{\eta}, \quad (1.16)$$

where  $\eta$  is the viscosity of the solvent and  $f(\kappa a)$  is a function of the radius  $a$  and the inverse Debye length  $\kappa$ . In the case of an apolar solvent,  $\kappa a \ll 1$  and  $f(\kappa a) = 1/3$  (Huckel limit) [63].

In the limit of low  $\kappa a$ , where  $a$  is the particle radius, the DLVO theory yields the following expression for the interaction potential between two spheres:

$$V_{el} = \frac{\epsilon \epsilon_0 a^2 \zeta^2}{R} \exp(-\kappa(r - 2a)), \quad (1.17)$$

where  $r$  is the distance between the particle centers. In the regime of small  $\kappa a$  the Deryagin approach, classically used in the DLVO theory, breaks down and using these approximate expressions can lead to a gross overestimation of the electrostatic interaction [64].

Since we are interested in electrostatic interactions, we may ask by which mechanisms charges can appear at the surface of nanocrystals. In an ideal system of colloidal nanocrystal, ligands are strongly bound to the surface of the particle and exactly compensate the charges carried by the surface ions [65–69]. NMR techniques have proven that Pb and Cd surface atoms are bound to two carboxylic acid molecules through a X-type bond. However, defects in this surface coverage can lead to charges and, as pointed out below, a small number of charge can have an important impact on the interactions between nanocrystals in organic solvents. Reports on  $\zeta$ -potential measurements of semi-conducting nanocrystals are scarce. This is due to the fact that these small electrophoresis mobilities are difficult to measure using standard instrumentation. However, electrostatic effects are thought to be at the origin of the structural diversity of binary nanoparticle superlattices in which two nanoparticles of opposite signs self-assemble at a liquid-air interface [70]. In this case, the stoichiometry of the binary superlattice is dictated by the charges of the two components.

#### 1.5.4 Surfactant monolayer interaction

After their synthesis, colloidal nanocrystals are coated with a monolayer of surfactant which binds their surface. This monolayer makes the nanocrystals dispersible in organic solvents and provides colloidal stability to the dispersion. The surfactant chains are usually considered to behave like polymer chains in good solvent, however, we will see at the end of this section that this view is currently challenged by recent computational

and experimental findings.

When two nanoparticles approach at a distance smaller than twice the ligand brush length, the alkane chains have to compress, yielding a repulsive force between the nanoparticles. If we consider a flat plate covered with a brush of polymer, the interaction free energy has been devised by Hesselink *et al* [71, 72] and comprises two terms. The first term comes from the fact that upon mutual approach, the polymer chains at the surface of the particles lose configurational entropy since the volume they can explore is reduced. This can be viewed as an elastic contribution yielding a short ranged repulsion. The second “osmotic” contribution is caused by the mixing of the polymer chains which might be energetically favored or unfavored depending on the goodness of the solvent. The free energy, taking into account these two terms, reads:

$$\Delta G = 2\nu kT V(d) + 2(2\pi/9)^{3/2} \nu^2 kT (\alpha^2 - 1) \langle r^2 \rangle M(d), \quad (1.18)$$

where  $\nu$  is the density of polymer chains,  $\alpha$  is an expansion factor depending on the goodness of the solvent. It can be related to the Flory-Huggins interaction parameter  $\xi$  and also depends on the nature and molecular weight of the polymer. For example, for polystyrene it ranges from 0.9 (very poor solvent) to 1.6 (good solvent).  $\sqrt{\langle r^2 \rangle}$  is the r.m.s. end-to-end distance of the polymer in solution while  $V(d)$  and  $M(d)$  are functions depending only on the distance between the particles. From this expression, it is clear that the different parameters which play a role in the ligand stabilization of nanocrystals are:

- the density of the ligand brush; a denser ligand monolayer will make the repulsion stronger;
- the molecular weight and hence the size of the ligand;
- the ligand solvent interaction since adding a bad solvent for the chains will significantly reduce the mixing entropy and hence decrease the repulsion between the particles.

In the case of spherical colloids, the qualitative features described below still hold but the free energy calculation is complicated by the curvature of the particles. For large colloids, the Derjaguin approximation [73] considers that the brush length is much smaller than the radius of curvature of the colloid, which makes the calculation similar to the one of two flat plates. Of course, this approximation breaks down in the case of small nanocrystals and more involved approaches such as self-consistent field theory have to be employed [74]. This study shows that the interaction induced by the surfactant chain are always repulsive, in contrast with previous claims using similar simulation techniques [75, 76]. Moreover, when two particles approach, an important inter-penetration of the ligand chains occurs before the repulsion becomes significant. Finally, these simulations explore the extent to which the Derjaguin approximation and its modified version can be applied. The actual interaction is overestimated by the approximation but the agreement is quite good for small compressions.

Surfactant monolayer induced interaction can also be analyzed theoretically by using integral equation theory, taking into account the discrete nature of the solvent [77, 78]. This approach is particularly suitable for nanoparticles since their small size, only

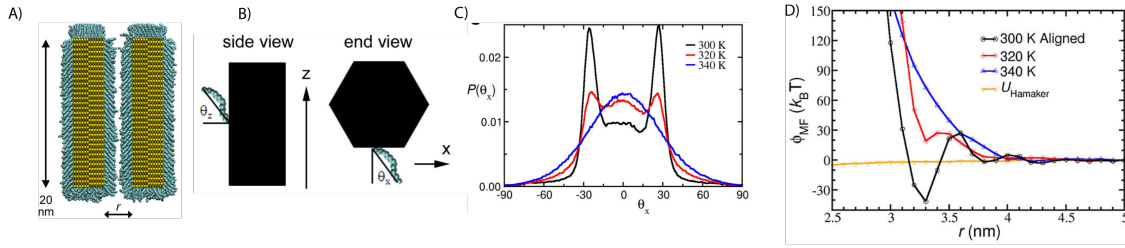


**Figure 1.8:** Molecular dynamics simulations on CdS nanorods in explicit solvent as described in [79, 80]. A) Scheme of the nanorods coated with ligands. B) orientation of the ligand with respect with the nanorod facet. C) orientation distribution of the ligand as a function of temperature. D) Potential of mean force between rods depending on the temperature. Note the deep potential well at 3.3 nm for the 300K temperature when the ligands are aligned.

an order of magnitude larger than the solvent molecule, makes questionable models considering the solvent as a continuum. Interestingly, these HNC calculations result in interaction potentials which differ from scaled potential based on continuous solvents. Several potential wells are predicted at short distances with depth comparable to  $kT$ , the deeper one being for a nanoparticles separated with one solvent molecule. These calculations also point the possibility to tune nanoparticle interactions by playing on the solvophilicity (or solvophobicity) of the ligand brush, through the use of solvent mixtures for example.

Orientalional ordering of the ligands at the nanocrystal surface can also generate strong inter-nanoparticle interaction. This has been shown by molecular simulations in the case of CdS nanorods coated by a monolayer of octadecyl ligands (Figure 1.8). In these simulations [79, 80], the solvent is taken explicitly into account. As temperature decreases, the ligand shell goes from a orientationally disordered state to a structure where the molecules have a preferred orientation with respect to the nanorods. This kind of phase transition has already been observed in self-assembled monolayers on macroscopic substrates. Solvent ordering occurs in the vicinity of the monolayer which causes a strong attraction between the nanorods. The potential of mean force between two nanorods can be measured from the simulations and potential wells as high as  $-30 kT$  have been found for a rod-rod distance of 3 nm. This important attraction can find its origin in the increase of the van der Waals attraction between the ligands since a denser ligand shell will be more polarizable. Subtle entropic effects can also contribute to the attraction since the entropic repulsion evoked earlier caused by a reduction of the conformational entropy of the ligand when they approach is absent in the case of ordered shells. The order-disorder transition temperature is also strongly dependent on the facet surface coverage. As the density of ligand increases on the nanoparticle, the transition temperature shifts towards higher values. Shifts of tens of degrees are observed for surface coverage varying from 75% to 100%. Hence, at a given temperature, increasing the surface coverage can yield to a destabilization of a colloidal solution caused by this ligand orientation induced attraction.

It is worth describing here recent experimental findings which highlight the complexity of the ligand induced interactions between colloidal nanocrystals. In a series of two papers, Peng *et al.* [81, 82] have investigated the solubility of carboxylic acid coated CdSe nanocrystals depending on temperature, particle size and ligand formula. Interestingly, they note that branched ligand (coined entropic ligands by the authors) are extremely efficient to stabilize large amounts of nanocrystals in solution. For example, 2-hexyl-decanoic acid increase the solubility by a factor 1000 to 10000 as compared with linear chain alkanes. This contradicts the belief that a longer alkane chain would induce a stronger repulsion and hence increase the colloidal stability. Overall, these recent studies show that colloidal nanocrystal interaction mediated by the ligand monolayer are richer than a simple repulsion whose magnitude solely depends on the length of the ligand.

Finally, a few words are in order to highlight the specificity of 2D systems as far as ligand mediated interaction are concerned. As a matter of fact, it has recently been pointed out that the interaction between the ligands covering the particle is far more effective when the curvature of the nanoparticle is as low as possible [83, 84]. This can easily be understood by considering the interaction between two particles with ligands bound on their surface. When spherical or rodlike particles approach, only a small fraction of the bound ligands interact as their orientation follows the curved geometry of the nanoparticle. On the contrary, when two plate-like particles are brought together, all the ligands on one face of one particle come in close contact with all the ligands on the opposing face of the other. Hence, in this geometry, the ligand-ligand interaction is of particular importance and since it is easily tunable through physico-chemical parameters, we expect this kind of interactions to be highly relevant in the case of nanoplatelets in which we are interested.

### 1.5.5 Depletion interaction

Depletion interactions are frequently manipulated in colloid/polymer mixtures in order to tune the interaction between colloids. The origin of this force is purely entropic and has been described in the past by Vrij as "attraction through repulsion" [85]. The physical principle is simple. Consider a dispersion of large colloids which also contains smaller objects such as polymer chains or micelles. When two colloids are getting close the small polymers are excluded from the space between the approaching colloids. This depletion of polymers between the particles induces an attraction between the colloids of osmotic origin, as if the polymers excluded from the depletion zone pushed the particles one towards the other. Another way of explaining this phenomenon is to notice that when the particles are separated, if we consider repulsive colloid-polymer interaction there is a depletion layer around each particle in which the concentration in polymer is lower than in the bulk. When the particles approach, these depletion layers overlap and the volume available for the polymer chains increases. This induces an attractive force of entropic nature.

In the limit of small depletant concentrations, the interaction potential is simply the

product of the osmotic pressure caused by the depletant and the overlap volume. The interaction strongly depends on the shape of the particles and Mason [86] showed that it is much stronger between platelets than between spheres. This shape dependent interaction can be put to good use for the separation of different shapes in (nano)-particles mixtures. For example, Park *et al.* [87] have used surfactant micelles to separate gold nanorods from gold nanocubes and nanospheres in multicomponent dispersions. Recently, Zhang *et al.* reported the self-assembly of squarelike  $\text{PbCrO}_4$  and nanoplatelets through depletion interactions induced by water-swollen reverse micelles [88]. Small angle neutron and X-ray scattering provided information on the structure of the microemulsion and quantitative comparisons with models showed that depletion by micelles was the likely mechanism. Depletion attraction has also been used to assemble semi-conducting CdSe/CdS nanorods in solution to yield 2D monolayers of close-packed hexagonally ordered arrays [89]. The addition of long chain fatty acids and amines, polymers, liquid crystals to a stable colloidal solution of nanorods induced an increase in the turbidity of the solution and the assembly of the nanorods.

### 1.5.6 Effect of water

The effect of trace water on the self-assembly of colloidal nanocrystals is a complex and maybe belittled issue. It has been proven long ago that small amount of water could play an important role on the colloidal stability of glass beads in organic solvent [90]. Even though water is not soluble in organic solvent classically used for self-assembly, trace amounts of water can be present in solution even after a brief contact with air or bounded to excess surfactant which has not been properly dried. Molar fractions of water in saturated solvents range from  $3.5 \times 10^{-4}$  for hexane to  $4 \times 10^{-3}$  for chloroform [60, 91]. Several reports [92, 93] observed that an air-free environment was mandatory for some features to be observed. For example, gelation occurs instead of nematic/isotropic transition in concentrated dispersions of CdSe nanorods.

Water may have several different effects on the interaction between nanocrystals in apolar solvents [60]. In the presence of surfactant, water can solubilize into reverse micelles which will modify the charging and screening of electrostatic interactions [61, 94]. Water can also adsorb at the surface of the nanocrystal and eventually change the sign and magnitude of the  $\zeta$ -potential. This effect has been demonstrated recently in dispersions of silica particles and should also apply for semi-conducting nanocrystals [95]. Using a surface force apparatus, Israelachvili *et al.* [96, 97]. studied the influence of water on the interaction between ZnS nanocrystals in dry and humid environment. The increase of water content in apolar solvents was found to induce capillary forces between the nanocrystals through the bridging of water pockets situated between the surface of the nanocrystal and the surfactant monolayers. This short range force enhances the adhesion between the nanocrystals and hence, induces the destabilization of the colloidal solution.



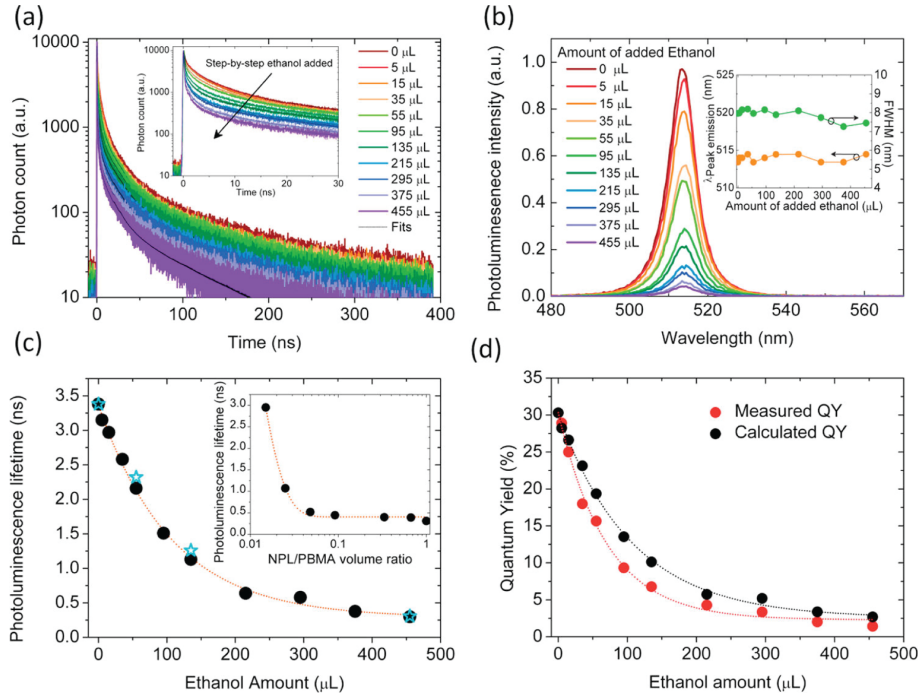


Figure 1.9: Effect of stacking on the fluorescence properties of CdSe NPLs. Upon addition of ethanol, the stacking of the NPLs induce a decrease in the fluorescence lifetime (a and c) and a decrease in quantum yield (b and d). Reprinted from ref [98].

## 1.6 Optical coupling between Nanoplatelets

The self-assembly of NPLs can be of interest in the perspective of their optical properties. When nanoparticles are in close contact collective properties can appear and the optical features of an ensemble is sometimes different from the sum of the individual properties. Such a collective effect has been demonstrated in the case of CdSe rods where clusters of rods blink less than individual rods. Using correlated electron microscopy and fluorescence imaging, Wang *et al.* [99] determined the blinking statistics of disorganized clusters of quantum rods. Interestingly, they found that clusters blink less than the sum of individual rods. Both maximum and mean on-times in a cluster of  $N$  nanorods increase by a factor of  $N$  or more as compared to individual nanocrystals. These results were rationalized in the framework of the Auger recombination model for blinking [100–104]. In this model, a quantum rod is dark if it is charged with the electron trapped in its environment and the hole left in the particle. When particles are clustered, exchange of electron can occur through tunneling between different particles. Other mechanisms such as trapping/detrapping or exciton rearrangement can also happen. Overall, these phenomena guarantee that clusters will remain bright even if some of the rods inside them are dark alternatively. Such collective effects on the blinking statistics have already been demonstrated in the case of spherical core/shell quantum dots [105, 106].

This kind of interaction can also occur in NPL and that was one of our motivations

to study these systems. Another type of coupling called FRET (fluorescence resonance energy transfer) [107] has been recently discovered in CdSe NPLs. This coupling occurs between the excited state of a donor and the ground state of an acceptor fluorophore. In this case, there is no photon appearing and the coupling occurs through a long-range dipole-dipole interaction. For this process to be efficient, there must be some overlap between the absorption spectrum of the acceptor and the emission spectrum of the donor. The two other parameters governing the rate of this process are the relative orientations of the donor and acceptor transition dipoles and the distance between the two fluorophores. In the case of NPLs, two different types of FRET can occur. Since there is a very small Stokes shift in these quantum wells, the emission and absorbance spectra of NPLs with a given thickness significantly overlap. Hence, homo-FRET where the energy transfer occurs between two platelets of the same thickness can occur. This phenomena has recently been shown to be the origin of the decrease in quantum yield of stacked NPLs. Upon addition of an anti-solvent, Guzelturk *et al.* [98] evidenced this loss of fluorescence and showed that it was coupled to a significant acceleration of the transient fluorescence decay. According to their interpretation, excitons are transferred from one well to another within the stacks until they arrive on a non-emissive platelet which anneals the exciton through nonradiative recombination. Hence, efficient and fast homo-FRET ultimately leads to a decrease of the quantum yield since a single non-emissive platelet within a stack will induce the quenching the whole stack. The same team has also investigated FRET between NPLs of two different thicknesses [108] (Figure 1.9). In this case, energy transfer occurs from the excited state of the thin NPLs to the ground state of the thicker one. An efficiency of only 60 % (as compared to 99% in the case of homo-FRET) was explained by the self-stacking of one population of NPLs which increases the mean distance between the accepting and donating platelet. In an independent study, Rowland *et al.* [109] used ultra-fast time-resolved spectroscopy to probe FRET in mixed films of 4 monolayers NPLs (donors) and 5 monolayers NPLs (acceptor). Their experimental study, backed-up by theoretical calculations show that FRET between NPLs in a co-facial arrangement occurs in the 6-23 ps time-regime which is almost two orders of magnitude faster than non-radiative Auger recombination. Since the latter process is very damaging as far as opto-electronic applications are concerned [110], ultra-fast FRET in these nanoparticles makes them particularly promising for lasers, photovoltaic devices or lightning.





# Colloidal stability and stacking of colloidal CdSe nanoplatelets

In this chapter, we examine the colloidal stability of CdSe nanoplatelets and relate it to their propensity towards stacking. Contrary to quantum dots or other colloidal nanocrystals, nanoplatelets are not stable in solution for a long time. This lead us to examine more closely the influence of various parameters on the colloidal stability of NPL dispersions.

## 2.1 Stability of quantum well dispersions

Colloidal nanoplatelets emitting at 513 nm were synthesized as described in the experimental section at the end of this manuscript, following a previous report [11]. TEM images of the as-synthesized CdSe nanoplatelets dispersed in hexane are shown in Figure 2.1. The low magnification micrographs show that the nanoplatelets are homogeneously dispersed on the substrate and that they lie flat on the substrate. At higher magnification, we observe that the platelets have a roughly square shape with sharp edges measuring 15.0 nm on average with a standard deviation of 2.5 nm (Figure 2.1.C). The UV-VIS absorption spectrum (figure 2.1.D) that displays sharp peaks is characteristic of CdSe nanoplatelets [12].

Just after the synthesis, a typical nanoplatelet solution has a transparent homogeneous yellow aspect and no trace of precipitation can be observed. After several days, however, a fluffy precipitate is visible at the bottom of the vial while some platelets are still present in solution. In order to quantify more precisely the kinetics of the precipitation, we conducted a series of experiments (see methods section) where a known quantity of dried platelets is first dispersed in hexane through sonication. We then record the optical density of the dispersion as a function of time for different platelet concentrations and report the normalized absorbance at 400 nm, a quantity proportional to the NPL concentration (Figure 2.2). As concentration decreases, the dispersion is less and less stable and flocculation occurs faster. This is qualitatively consistent with a von Smoluchowski coagulation kinetics [111] where the typical precipitation time is inversely pro-

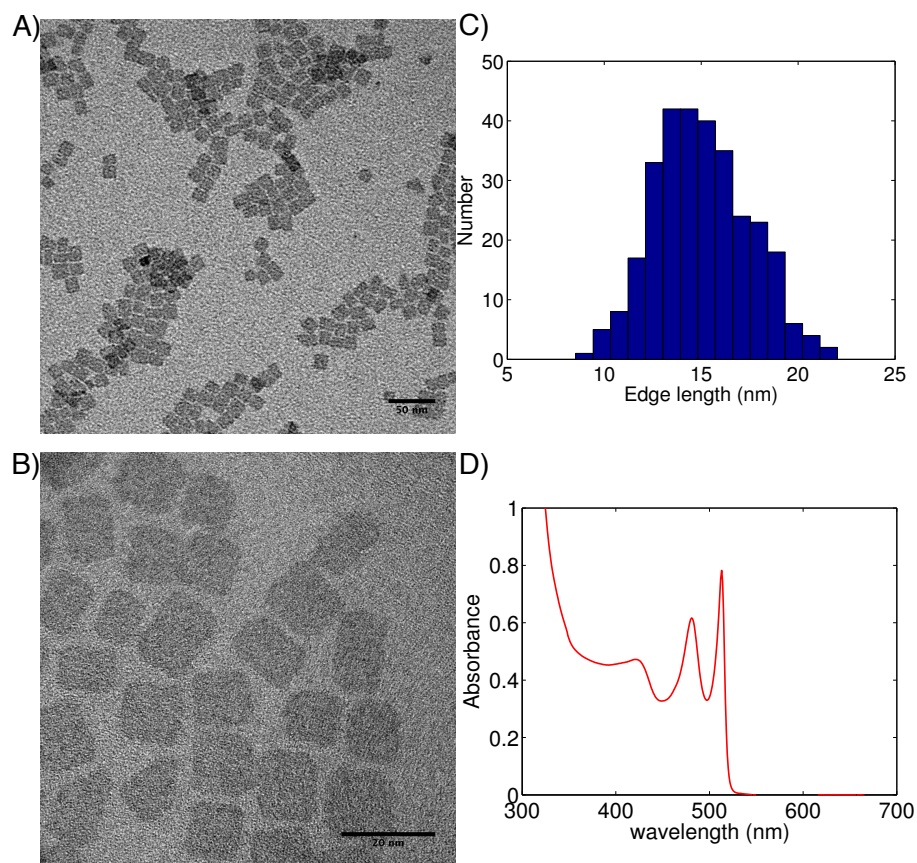


Figure 2.1: A) and B) represent TEM micrographs of the CdSe nanoplatelets as synthesized. Scale bars are 50 nm for A) and 20 nm for B). C) Histogram of the edge length measured on around 300 nanoparticles. D) Absorption spectrum of the diluted platelet dispersion.

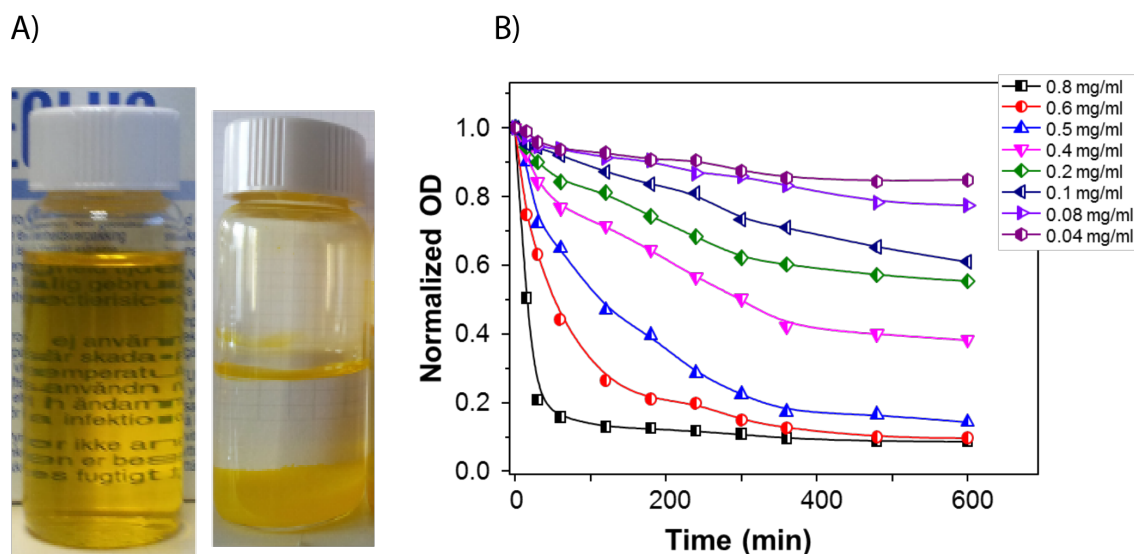


Figure 2.2: A) Photographs of QW dispersion in hexane. Left: just after the synthesis. Right: after a few weeks. B) Normalized absorbance at 400 nm of a colloidal dispersion of CdSe NPL as a function of time for different platelet concentrations.

portional to the density of the dispersion. The more concentrated the dispersion, the more probable the collisions between the platelets and hence, the less stable the dispersion.

We also investigated the influence of ligand chain on the precipitation kinetics by using carboxylic acids with increasing size alkyl chains (heptanoic, octanoic, decanoic, myristic and oleic acid). A similar trend is observed for all the acids: the stability of the dispersion increases with the platelet concentration (data not shown). Furthermore, we observe that the longer the acid chain, the more stable the dispersion.

## 2.2 Structure of the precipitate

Precipitates of inorganic particles can have different structures ranging from fractal aggregates or amorphous precipitates to colloidal crystals. A technique of choice to probe the structure is small angle X-ray scattering (SAXS). Hence, in order to better understand the structure of the nanoplatelet aggregates, they were transferred into glass capillaries and examined using SAXS (see methods section for details). Figure 2.3 shows SAXS patterns for a dilute stable NPL solution and for their self-assembled precipitate. The dilute dispersion exhibits an isotropic scattering pattern with a scattered intensity slowly decreasing with increasing scattering vector modulus  $q$ , characteristic of nanometric particles dispersed in solution. In contrast, intense scattering peaks are visible in the radially averaged intensity for the aggregated dispersion. These peaks correspond to sharp rings in the 2D scattering pattern visible in the inset.

The structure factor ( $S(q)$ , see inset of Figure 2.3) is obtained as  $I_s(q)/I_p(q)$  where

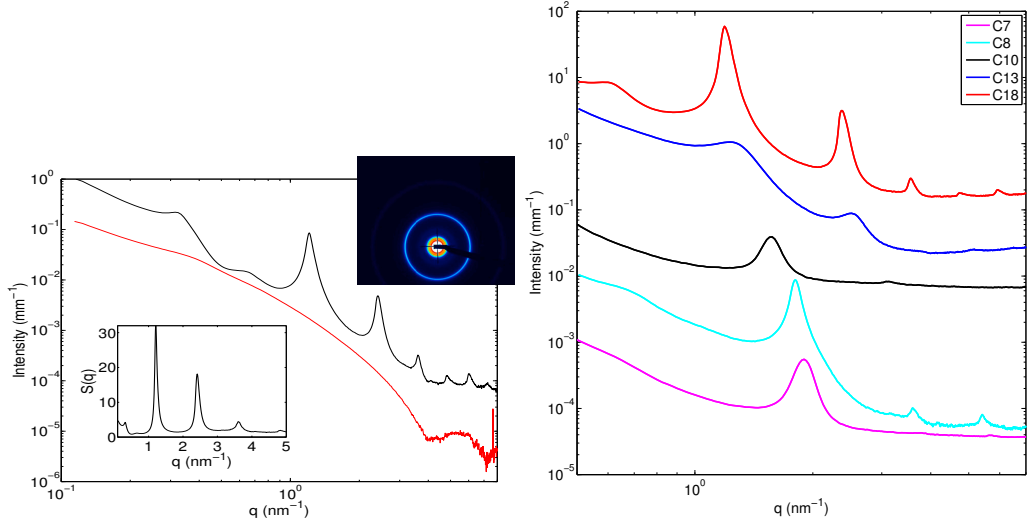


**Figure 2.3:** Left: SAXS patterns of stacked (black curve) and unstacked (red curve) CdSe nanoplatelets. Top inset : 2D SAXS image of the stacked nanoplatelets. Note the presence of rings in the pattern. Bottom inset : structure factor of the stacked platelets. Right: SAXS patterns of stacked CdSe nanoplatelets with different ligand chain lengths

$I_s(q)$  and  $I_p(q)$  are the background-corrected scattering patterns of the stacked platelets and of the free particles respectively. The position and full width at half maximum of the 6 visible peaks are determined through Lorentzian fitting of the structure factor. The peaks are located at scattering vectors  $q^*$ ,  $2q^*$ ,  $3q^*$ , ...,  $6q^*$  with  $q^* = 1.215 \text{ nm}^{-1}$ , corresponding to a distance of 5.17 nm in real space. The average number of Bragg planes scattering coherently is given by [112]  $\bar{N} = q^*/\Delta q^*$  where  $\Delta q^*$  is the full width at half maximum of the peak. In our case,  $\bar{N}=14$ , which is consistent with an average grain size (given by  $\bar{D} = 2\pi K/\Delta q^*$  where  $K$  is the Scherrer constant  $\simeq 0.93$ ) of 67 nm. We observe that the FWHM increases with the order of the Bragg reflection and goes from  $0.08667 \text{ nm}^{-1}$  for the first order peak to  $0.2589 \text{ nm}^{-1}$  for the 5th order. For true long-range order, the FWHM should remain constant with increasing order of the Bragg reflection whereas it increases in the present case [113]. This is consistent with the fact that a 1-dimensional order cannot really be long-ranged if only next-neighbor interactions are involved. [114] On the other hand, a liquid-like structure factor is much too shallow to represent the experimental data. Hence, we observe an intermediate state between a usual liquid and a solid with true long-range order.

In another series of experiments, we varied the length of the alkane chain of the ligand by replacing the original oleic acid ligand (18 carbon atoms) with saturated fatty acids with 7 to 14 carbon atoms. Figure 2.3 shows the SAXS patterns of the precipitate for the five chain lengths. As expected,  $d^* = 2\pi/q^*$  shifts towards larger values as the chain length increases (table 1). The center-to-center distances between the platelets is, in the case of oleic acid, smaller than the sum of the NPL thickness and two fully stretched molecules. Some degree of interdigitation of the chains linked to two different NPL

ligand	measured $d^*$ (nm)	expected $d^*$ (nm)	difference (nm)
oleic acid	5.27	6.05	0.78
myristic acid	5.13	4.79	-0.34
decanoic acid	3.99	4.03	0.04
octanoic acid	3.46	3.52	0.06
heptanoic acid	3.3	3.27	-0.03

Table 2.1: Measured center-to-center distance between the platelets deduced from the position of the scattering peak. The expected  $d^*$  value is calculated as  $e + 2\ell$  where  $e$  is the thickness of a platelet (1.2 nm) and  $\ell$  is the length of an aliphatic chain as calculated by the Tanford formula. [115]

is thus observed. However, this is not the case for the the other chain lengths, where the measured distance is either very close (for heptanoic, octanoic and decanoic acid) or smaller (for myristic acid)

## 2.3 Stability criteria

In order to rationalize these findings, we calculate a simple stability criterion for NPL. van der Waals attractions between the polarizable cores of the nanoparticles will tend to destabilize the dispersion while short-range repulsion caused by the oleic acid alkyl chain forbids close contact of the CdSe platelets. If we approximate the van der Waals attraction to the case of infinite flat plates, the interaction free energy per surface unit is given by:

$$\frac{\Delta G}{\mathcal{A}} = \frac{-A_{121}}{12\pi H^2}, \quad (2.1)$$

where  $A_{121}$  is the Hamaker constant for CdSe through hexane,  $H$  is the distance between the faces of the NPL and  $\mathcal{A}$  is the area of interaction. The colloidal stability of the platelets is assured if the ligand brush at the surface precludes small interparticle distances that would lead to  $\Delta G > kT$  where  $kT$  is the thermal energy. This stability criterion for a square platelet of edge length  $a$  ( $\mathcal{A} = a^2$ ) becomes:

$$\frac{H}{a} > \sqrt{\frac{A_{121}}{12\pi kT}} \quad (2.2)$$

where  $H$  is the distance between the platelets. The Hamaker constant for CdSe is  $A_1 = 11 \times 10^{-20}$  J and for hexane it is  $A_2 = 3.8 \times 10^{-20}$  J. By using combining relations for Hamaker constants [52], we can calculate the Hamaker constant of CdSe through hexane:  $A \simeq (\sqrt{A_1} - \sqrt{A_2})^2$ . This leads to an Hamaker constant for CdSe through hexane of  $1.87 \times 10^{-20}$  J. For a mean edge of 15 nm, we obtain  $H = 5.2$  nm, which is close to the length of two oleic acid molecules. In other terms, the van der Waals attraction energy is exactly equal to the thermal energy for a NPL separation corresponding to a non-interdigitated oleic acid bilayer. For a colloidal dispersion to be thermodynamically stable, the thermal

energy has to be much larger than van der Waals attraction at this distance ( $\Delta G \ll kT$ ). At the other extreme, if  $\Delta G \gg kT$ , colloidal solutions will be destabilized within seconds since the only barrier towards flocculation is the encounter of colloids through brownian motion, which in the case of nanoparticles is very fast. Here, we are in an intermediate state where colloids can be stable for a long time since but other factors affecting the interaction potential or the contact between the nanoparticles can have an important effect on the colloidal stability. In the following, we investigate two other factors: the concentration in ligand and trace amount of water which both importantly affect the stability of the dispersion.

## 2.4 Effect of oleic acid concentration

As oleic acid (OA) coats the NPL surface, it is expected that its concentration will affect the colloidal stability of the platelet dispersion. In order to quantify this effect, we added various OA amounts to a 0.4 mg/mL nanoplatelet dispersion and monitored its optical density at different times. Figure 2.4 shows the optical density (normalized by its value at time 0) as a function of time for increasing concentrations of oleic acid. For OA concentrations ranging from 0 to 10 mM, the stability of the dispersion improves since the NPL concentration decreases more slowly with time. However, we observe an optimum in OA concentration for colloidal stability at around 10 mM (Figure 2.4b) as adding more oleic acid leads to faster destabilization of the dispersion.

The increase of stability through initial addition of oleic acid can be understood in terms of better passivation of the nanocrystal surface. Thoroughly washed nanocrystals may lack a well packed ligand monolayer and addition of OA in the first place will increase the density of the ligand brush and stabilize the dispersion. The decrease in colloidal stability with further addition of acid is more surprising. We have identified four physical explanations for this destabilization. It could be explained by a depletion attraction induced by OA micelles. This interaction has been shown to induce precipitation in several cases. [34, 88, 89] However, it is usually observed to have a significant effect at higher concentrations (in the 100 mM range). Oleic acid may also have an influence on electrostatic interactions between the nanoplatelets. As previously shown [61, 94], surfactants can have two different effects on electrostatic interactions in non-polar solvent. They can change the surface charge of the nanoparticles and/or screen the electrostatic repulsion as ions do in polar media. To gain insight on this hypothesis, we conducted  $\zeta$ -potential measurements on samples with varying OA concentration (see methods section for experimental details). Without supplementary OA, we measured an electrophoretic mobility of  $0.07 \times 10^{-4}$  cm<sup>2</sup>/Vs consistent with weakly positively charged platelets. The sign of the mobility is consistent with positive charges created by surface Cd<sup>2+</sup> ions not passivated by the ligands. This mobility corresponds to a  $\zeta$ -potential of +13 mV in the Huckel approximation of large electrostatic double layers. Upon addition of oleic acid, we do not observe a measurable change in the electrophoretic mobility. Hence, these measurements are not consistent with a significant decrease of the surface charge of the nanocrystals upon addition of oleic acid. However, OA can still screen the electrostatic charges and reduce the range of the electrostatic re-



pulsion. Addition of OA can lead to a decrease of the solubility of the nanocrystals. As OA is more polar and protic than hexane, the solvent will become a less good solvent for the ligand chains which will have a tendency to come together and induce the stacking of the platelets. Finally, a recently described orientational ordering of the ligands could rationalize our experimental findings. As described in section 1.5.4, ordering of the surfactant coating the nanoparticles can induce a strong attraction between them and hence provoke the destabilization of the colloidal dispersion [79, 80]. This interpretation is consistent with the fact that increasing the ligand concentration decreases the colloidal stability since the phase transition only occurs when the density of the surface ligand is high enough. In [80], the transition temperature increases with surface coverage. Hence, at constant temperature, increasing the surface coverage could lead to the onset of the phase transition.

## 2.5 Effect of water on the colloidal stability

Other factors can also affect the colloidal stability such as the ambient atmosphere in which the dispersions are manipulated. We observed that dispersions kept in a moisture-free environment are more stable. Figure S3 shows a picture of two samples of the same platelet dispersion: one kept in a glovebox and one kept under ambient conditions. The sample in the glovebox keeps its translucent aspect and no sign of precipitate or turbidity was observed over several weeks. Hence, away from air moisture, the platelets remain well dispersed in solution and do not aggregate. In contrast, the colloidal dispersion kept under ambient conditions is much less stable. Either water or oxygen can play a role on the colloidal stability of the platelets. Oxygen could form a CdO layer on the platelet surface but this would be visible in the UV-Vis absorbance spectra which is not the case here. In order to prove that trace water has indeed a strong effect on the colloidal stability, we prepared water saturated hexane by mixing hexane and water using a vortex mixer and taking the organic phase. In the glove box, the stability of a platelet dispersion with the wet hexane was compared to the one made with hexane dried over molecular sieves. The dry hexane dispersion is stable while the wet hexane dispersion has precipitated.

Traces of water in the solvent can influence the friction property of the nanoparticles as already documented in the case of ZnSe nanorods in apolar solvents [96, 97]. In addition, Israelachvili's group showed, using a surface force apparatus, that a dispersion of colloidal nanocrystals in an apolar solvent is destabilized upon water exposure through the effects of a long-range attraction and a short-range adhesion. Water pockets form between the surfactant and the surface of the nanoparticles which enhance the capillary forces between the nanoparticles and, hence, destabilize the dispersion. This interpretation rationalizes the lack of long-term stability of the NPL dispersions in air and the higher stability observed in dry atmosphere but was initially made for oleylamine capped ZnS nanorods. Since oleylamine is a labile L-type ligand, water can easily replace it at the surface of nanocrystals. In our case, X-type ligand are thought to be more tightly bound to the cadmium surface atom. Recently, NMR studies have shown that small



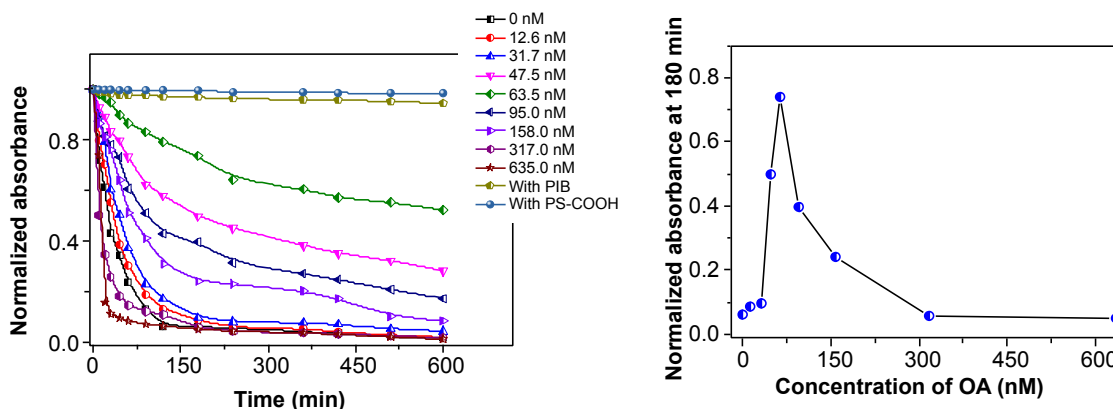


Figure 2.4: Left: normalized absorbance at 400 nm of a colloidal dispersion of CdSe nanoplatelets as a function of time for different added oleic acid concentrations and for PIB polymer (polyisobutylenesuccinimide). Right: normalized absorbance at 510 nm after 3 hours as a function of added oleic acid concentration. In all cases, the concentration in NPL is 0.4 mg/ml.

amounts of alcohol can strip carboxylic acid ligand from semi-conducting nanocrystal surfaces through a proton exchange [116]. This mechanism should also hold with water molecules and a similar reaction between carboxylic acid and water should take place leading to the destabilization of the dispersion.

## 2.6 Stabilization by polymers

In order to circumvent the lack of stability of as-synthesized NPL, we investigated the use of adsorbing polymers which would act as a protective barrier against coagulation. We first used a polyisobutylenesuccinimide (PIB) polymer which has already been proven efficient for stabilizing colloidal dispersions in non-polar solvents [117–119]. Adding a small quantity of this polymer to a stacked dispersion of NPL immediately yields a transparent solution and much more stable dispersions were obtained by adding minute amounts of polymer (Figure 2.4). Unfortunately, this polymer has a strong quenching effect on the fluorescence of the platelets and drastically reduces their quantum yield. Furthermore, the platelets are chemically unstable in presence of PIB in solution, as they slowly dissolve on the time scale of months. This precludes the use of this polymer for long-term colloidal stabilization of CdSe nanoplatelets.

Inspired by a recent report [120] proving the efficiency of polymer coating to control the steric stabilization of nanocrystals, we coated our NPL with carboxylic acid terminated polystyrene (see methods for the synthesis). Since the polymer is not soluble in hexane, we used THF instead. Two different polymers of molar mass 1700 and 2500 g/mol were used and gave very similar results. Figure 2.5 shows that these polymers stabilize very well the dispersion since the absorbance is almost constant on the studied time scale. In contrast, OA coated platelets aggregate in THF, though slower

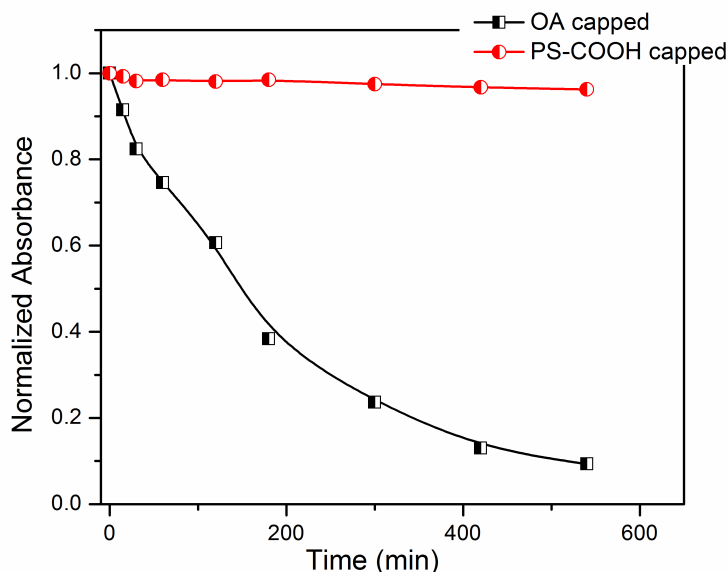


Figure 2.5: Normalized absorption at 400 nm of NPLs dispersions in THF as a function of time for two different ligands: oleic acid or polystyrene. The platelet dispersion was 0.8 mg/mL. The molar mass of the PS was 2500 g/mol. Similar results were obtained with 1700 g/mol.

than in hexane. This is due to smaller van der Waals attraction between CdSe through THF than through hexane ( $A_{THF} = 7.58$  [52]). Importantly, the polymer coating does not quench the fluorescence of the nanoplatelets and fluorescence is still observed in dispersions of PS coated NPLs. To explain the observed stabilization, we can calculate an order of magnitude of the grafted polymer thickness. We expect the polymer length to be around twice the coil radius of the polymer in good solvent given by the formula  $R_g = 0.275 \times M_w^{0.5}$  as described in ref [121]. This yields a thickness of 2.2 nm and 2.75 nm for the 1700 and 2500 g/mol polymer respectively. Hence, we see that the thickness of the polymer grafting can not explain the increased stability of the platelets in solution since it is the same for the small polymer and for oleic acid. However, the polymer is not perfectly mono-disperse and some large chains may induce a long range repulsion. Another explanation could be that the brush is much denser in the case of the polystyrene than in the case of the oleic acid which makes the short range repulsion stronger. Finally, it is possible that the polymer shell is less permeable to water, which improves the stability of the dispersion. The fact that two ligand brushes with similar thickness but different structures behave in a such a different fashion is surprising and will be the subject of further attention.

## 2.7 A dipole moment in the nanoplatelets ?

As described previously, van der Waals interaction alone seem too weak to induce the stacking we observed. In the past, dipolar interaction (section 1.5.1) was found to be important to explain the self-assembly of other semi-conducting nanoparticles. Motivated by these results on rods and spheres, we suspected that dipolar attraction could explain some of our results and hence tried to measure a dipolar moment in CdSe nanoplatelets. To do so, we performed two kinds of experiments. Electro-optics measurements consist in imposing an electric field to a dispersion and measure to optical response of the media using microscopy in polarized light. If anisotropic nanoparticles couple to the field and align in a preferential direction, the birefringence of the media increases which is easily detected. The  $\Delta n$  vs  $E$  curve, where  $\Delta n$  is the difference of birefringence when the  $E$  field is on as compared to  $E = 0$  can then yield quantitative information on the direction and magnitude of the dipole. Such experiments have been conducted by Dr Ivan Dozov at the lab and the results are currently being processed. They show that a dipolar moment is indeed present in CdSe NPLs but its value and direction still need to be determined. This is confirmed by recent SAXS experiment under electric field. Here, the 2D X-ray scattering patterns are recorded under different electric fields. When no field is present, the 2D pattern is isotropic since there is no preferential orientation of the NPLs in solution. If the platelets align, the pattern becomes anisotropic with an excess of scattering perpendicular to the orientation direction. Figure 2.6 shows radial profiles at the scattering vector corresponding to the peaks of small NPLs stacks ( $q \simeq 0.1 \text{ \AA}^{-1}$ ) with and without electric field. We notice a small difference between the two patterns showing a weak alignment of the NPLs under electric field. This change is reversible and isotropic patterns are recovered when the field is switched off. These results need to be confirmed and quantified more thoroughly but we can safely conclude for now that CdSe NPL indeed display a electric dipole which may induce important inter-particle attraction.

## 2.8 Effect of self-assembly on optical properties

### 2.8.1 Phonon coupling in stacks of CdSe Nanoplatelets

Stacking has been shown to influence the optical properties of NPLs. Due to their very small Stokes shifts, a photon emitted can be re-absorbed by a neighboring platelets within a stack. This radiative energy transfer was proposed to explain the emergence of the longitudinal optical phonon replica of the band-edge exciton at low temperature [122] (Figure 2.7). Since this emission line is red-shifted as compared to the band-edge emission, it can not be re-absorbed by a neighboring platelet. This hypothesis is strengthened by the fact that the emission wavelength does not depend on the separation distance between the NPLs which can be tuned through ligand exchange. Furthermore, this interpretation is supported by a basic model predicting an increase in the relative intensity of the phonon replica versus band edge emission as the lateral dimension of the NPLs increases.

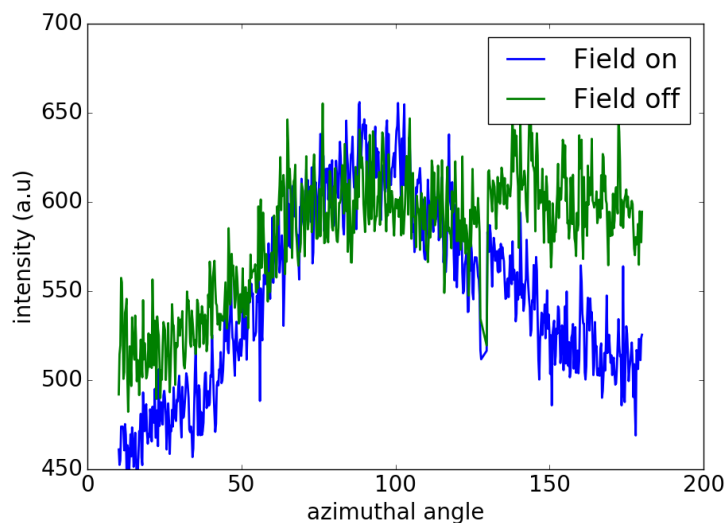


Figure 2.6: Azimuthal profile of SAXS patterns of a dispersion of NPLs with or without field, showing a small orientational order.

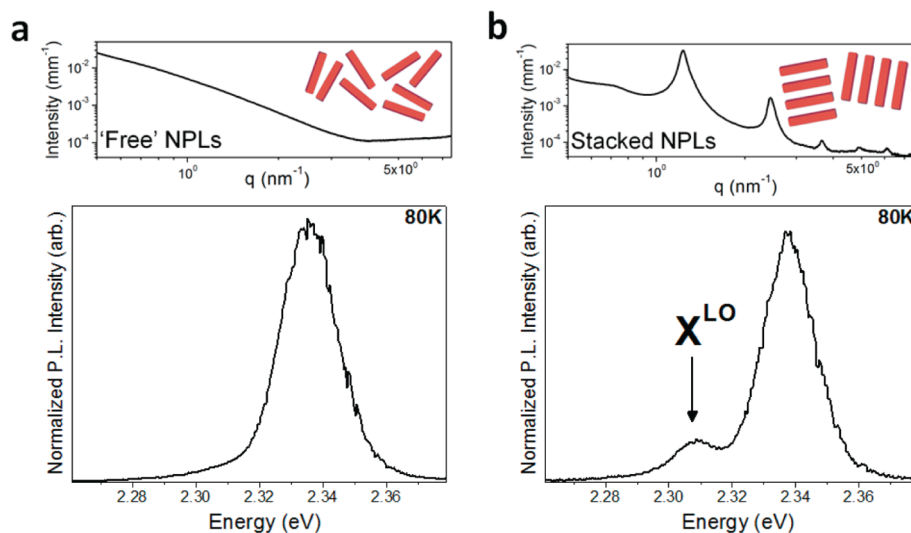


Figure 2.7: Apparition of a phonon  $X^{LO}$  line at cryogenic temperatures due to the stacking of CdSe nanoplatelets. Top panels show SAXS patterns of non-stacked and stacked NPLs. Bottom panels show the emission spectra in the two cases. Reprinted from ref [122].

## 2.9 Conclusion

We have examined the colloidal stability of CdSe nanoplatelets in a non-polar solvent and shown that when coated by their native ligands, they undergo stacking, which leads to their colloidal destabilization. The flocculation kinetics depends on several parameters such as the concentration in platelets, the chain length of the ligand and its concentration. We succeeded in obtaining stable dispersions through exchange of the native ligand with a short polystyrene polymer. Control over the dispersion state of these NPLs is key for a more comprehensive study of their optical properties and their processing for future applications. A better understanding of the stability of these dispersions will be achieved through the quantitative description of inter-particle colloidal forces between these anisotropic particles in non-aqueous media.

# Self-assembly of CdSe nanoplatelets into anisotropic superparticles

## 3.1 Introduction

In the previous chapter, we have shown that upon aging CdSe NPLs have a strong tendency towards stacking. However, this precipitation is uncontrolled and the precipitate is only structured on short length scales. Here, we show that the addition of an anti-solvent to a stable dispersion of CdSe nanoplatelets in hexane triggers the formation of anisotropic supra-crystals whose length can reach several micrometers. The platelets stack in a 1D-fashion one on top of each other and exhibit a columnar order within the superparticle floating freely in solution. Furthermore, the platelets are all oriented perpendicular to the long axis of the needle and hence, they display polarized light emission.

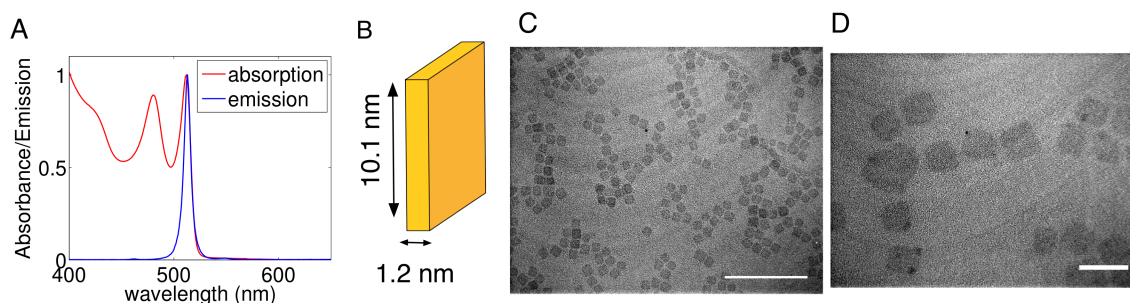


**Figure 3.1:** A) Absorption and emission spectra of the CdSe nanoplatelets. B) Schematic representation of the nano-platelets. C) and D) TEM images. Scale bars measure 100 nm and 20 nm respectively.

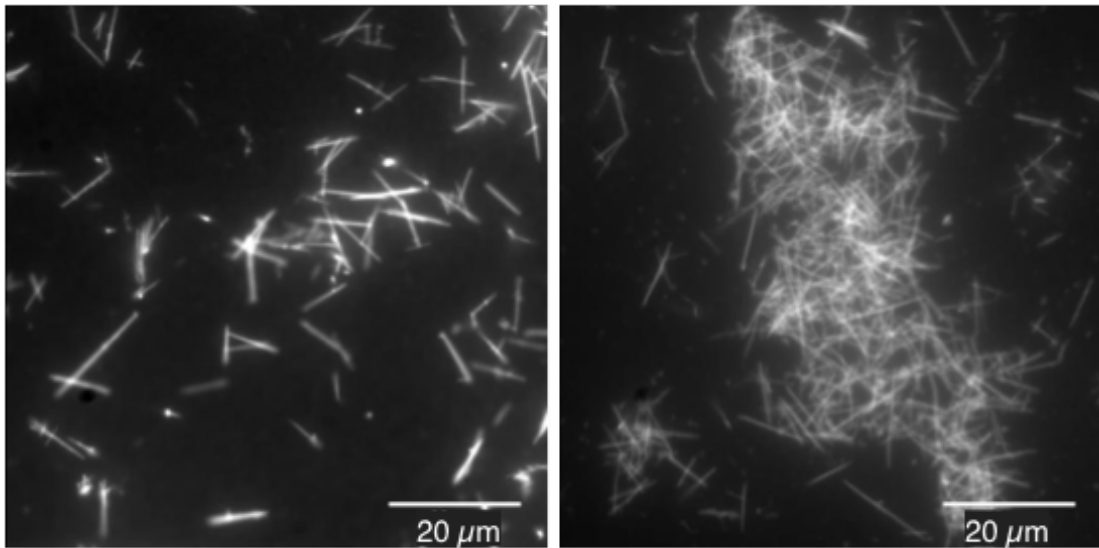


Figure 3.2: Fluorescence microscopy of the super-particles deposited on a glass slide.

## 3.2 Results and discussion

We synthesized CdSe nanoplatelets as described in the methods section following a modification of a previously reported synthesis [11, 12]. After purification, we obtain a dispersion of NPs the absorption and emission spectra of which are shown on Figure 3.1. The two sharp maxima at 513 nm and 480 nm in the absorption spectrum correspond respectively to the electron-heavy hole and electron-light hole transitions due to the quantum confinement of the electron/hole pair in the potential well created by the limited thickness of the platelets. As no other peak is visible, the dispersion only contained one population of 4 MLs CdSe NPs. The large excess of oleic acid added at the end of the synthesis ensures that these ligands coat the faces of the NPs. Electron microscopy investigation of the NPs (Figure 3.2) shows that they have a roughly square shape with a monodisperse size distribution. The edges measure on average 10.1 nm with a standard deviation of 1.15 nm (based on measurement of 300 nanoparticles).

When a small amount of ethanol is added to the dispersion of NPs in hexane, the solution becomes slightly turbid after a few seconds, indicating the presence of large particles which scatter light. Fluorescence optical microscopy observation of the dispersion indicates the presence of long anisotropic particles free-floating in solution (Figure 3.2).

These highly fluorescent superparticles (SPs) can reach 20  $\mu\text{m}$  in length while their width is beyond the resolution of the optical set-up. Transmission Electron Microscopy confirms the formation of anisotropic SPs composed of individual nanoplatelets. TEM images of fresh (a few hours) samples display fiber-like superparticles composed of a few subunits separated by regions where the density of nanoparticles is smaller (Figure 3.3). In some cases, kinks are visible at these places. However, in TEM images of aged (a few months) samples, long defect-less needles are observed. We suspect the defects to



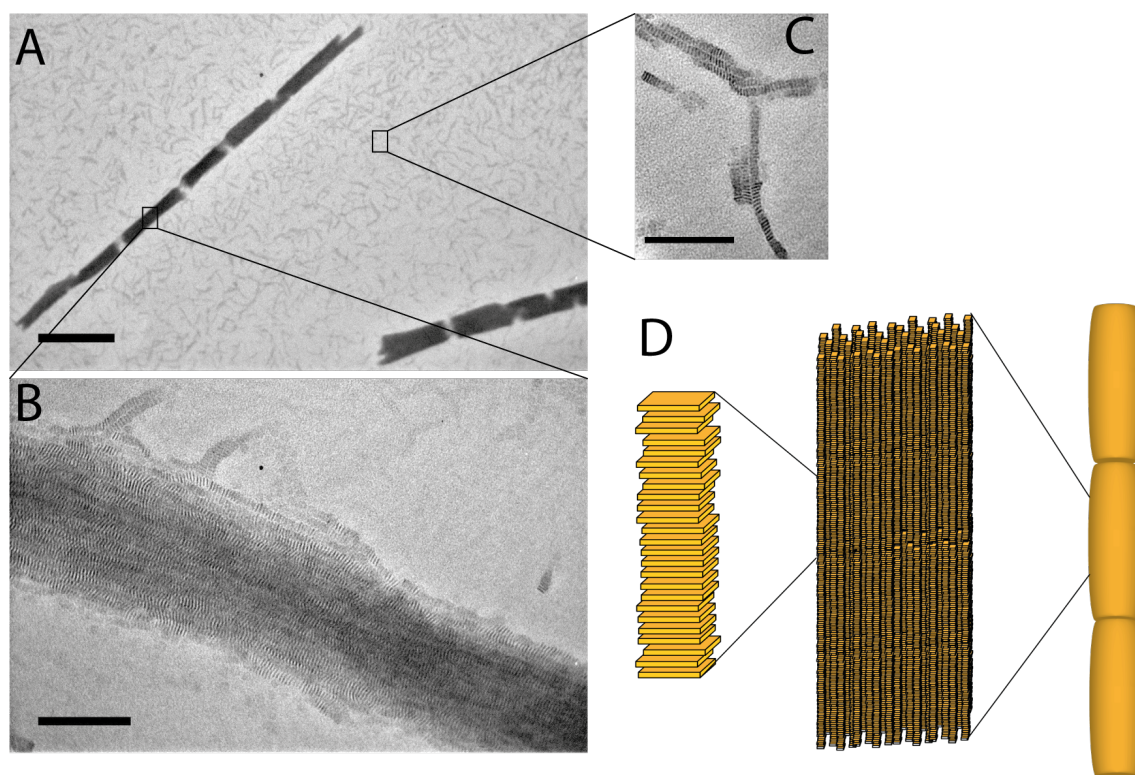
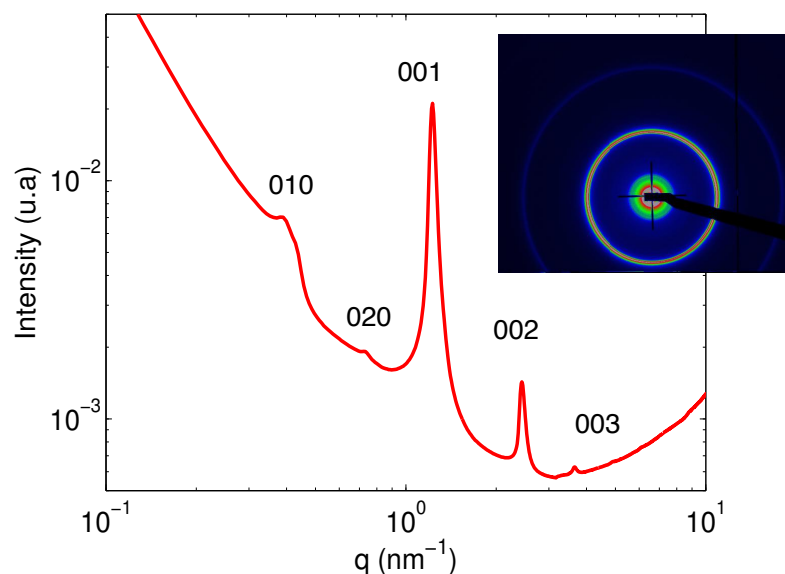


Figure 3.3: Images of the superparticles A) Low magnification image showing an entire superparticle. Scale bar is 1  $\mu\text{m}$ . B) Higher magnification image showing the stacking of the nanoplatelets within a superparticle. Scale bar is 100 nm. C) Subunits which can be seen besides the superparticles. Scale bar is 100 nm. D) Scheme representing the hierarchical structure of the superparticles.



**Figure 3.4:** Small Angle X-ray Scattering pattern of the superparticles in a glass capillary. Inset: image of the scattered intensity in false colors.

arise from a drying instability occurring during the preparation of the TEM grid. This difference might be due to the fact that long-term rearrangements of platelets within the aged SPs provide them with a higher density and rigidity, which prevents them from breaking upon drying constraints.

Within the SPs, the nanoplatelets are organized in a highly aligned columnar structure where the principal axis is perpendicular to the plane of the nanoplatelets. In the two lateral directions, between 10 and 20 columns of stacked NPs stand side by side within the superparticles whose widths are comprised between 150 and 300 nm. Based upon these dimensions, we can infer that each SP is made of  $\simeq 10^6$  nanoplatelets. We note that, besides the superparticles, smaller ensembles consisting of a more limited number of stacked nanoplatelets (from 5 to 100) are also visible on the TEM grid (Figure 3.3.c).

To further characterize the order within the superparticles, synchrotron Small Angle X-ray Scattering (SAXS) experiments were performed. Figure 3.4 shows a SAXS pattern of the dispersion of SPs. The pattern being isotropic, there is no preferential orientation of the micro-needles in solution.

A series of three Bragg peaks is visible at wave vectors  $q = 1.228, 2.445$  and  $3.651 \text{ nm}^{-1}$  corresponding to the 001, 002 and 003 stacking reflections of a columnar structure with period 5.11 nm. At smaller wave-vectors, two less intense peaks are observed at  $q = 0.390$  and  $0.733 \text{ nm}^{-1}$ . These peaks correspond to a period of 16.1 nm and can therefore be attributed to lateral ordering of the nanoplatelet columns within the superparticles. Since the order is of much longer range in the 001 direction than in the perpendicular plane, the corresponding Bragg peaks are much more intense. The SAXS pattern thus confirms the TEM examination of the sample and is consistent with a columnar structure where positional order is much more long-ranged in the principal direction of the

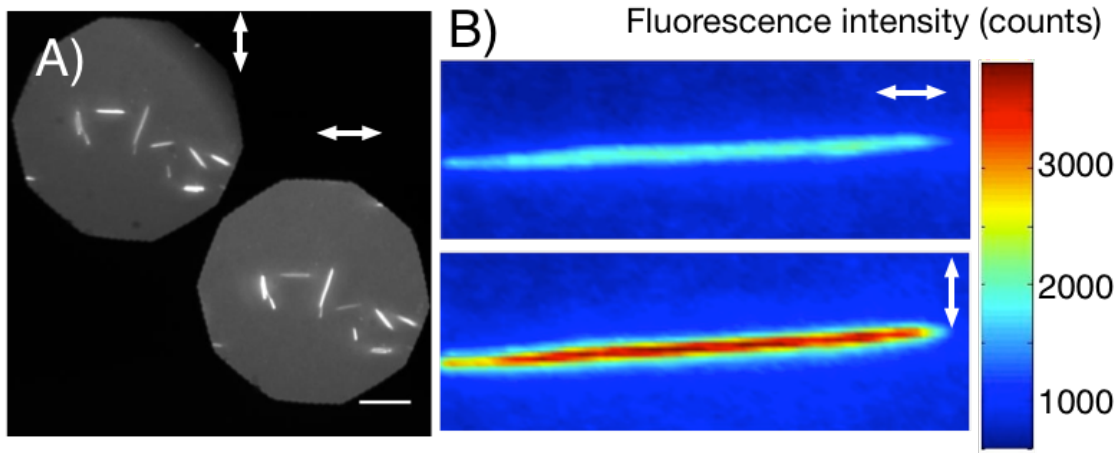


Figure 3.5: A) Epifluorescence measurement of microneedles as a function of the polarization direction. Scale bar is  $15 \mu\text{m}$ . B) Fluorescence intensity in false color for a single microneedle depending on the polarization direction. Scale bar is  $10 \mu\text{m}$ .

superparticle.

Finally, we studied the polarization of the emission of the superparticles. Since the nanoplatelets are anisotropic, we expect that they emit light polarized in their plane. To test this prediction, the platelets need to be oriented perpendicular to a substrate. Because all the nanoplatelets, in a given superparticle, stand oriented perpendicular to the principal direction of the microneedle, the light emitted by the superparticles should be linearly polarized.

We used an epifluorescence set-up comprising a polarizing beam splitter which allowed us to visualize on the same image both horizontal and vertical components of the light emitted by the superparticles. As seen on Figure 3.5, the needles oriented perpendicular to the polarizer appear brighter than those oriented parallel to it. The light emitted by the superparticles is strongly polarized in the direction perpendicular to their long axis. This also shows that an individual nanoplatelet emits light polarized in its plane. Since we collect half of the light intensity polarized in the plane of the platelets, the degree of polarization can be quantified by a polarization factor  $r = (2I_{\perp} - I_{\parallel}) / (2I_{\perp} + I_{\parallel})$  where  $I_{\parallel}$  is the intensity polarized parallel to the needles. This factor reaches 71% for the superparticle on Figure 5.b. This value is of the same order of magnitude as the polarization factor measured on individual quantum dots [123] and a certain degree of depolarization is probably due to some orientation disorder of the nanoplatelets within the superparticles. Recently, a polarization factor of 86% has been measured on superparticles of CdSe quantum rods [124] but, in this case, the measurement was made at a fixed wavelength corresponding to the maximum photoluminescence of the rods whereas we measured an intensity averaged on all the wavelengths passing through the dichroic mirror.

We now turn to the discussion of the formation of the superparticles. The precise

mechanism by which the superparticles form is still under systematic investigation and will be the topic of a future publication. Nevertheless, we already report here that several key factors influence the quality of the superparticles, in terms of aspect ratio and degree of orientational order. First, the shape of the nanoplatelets is a crucial parameter. Only nanoplatelets with well defined edges self-assemble into superparticles. Also, the cross-section of the nanoplatelets has to be square and not rectangular to yield long superparticles. This is likely a simple geometrical effect; perfectly square nanoplatelets pack more efficiently into dense superparticles than particles of more complicated shapes.

Second, the assembly pathway is also of importance. As mentioned above, the formation of these superparticles is triggered by the addition of ethanol to a hexane solution of nanoplatelets. Ethanol is indeed known to induce aggregation of colloidal nanocrystals in apolar solvent. It has been shown by NMR that ethanol molecules replace oleic acid at the surface of quantum dots [116], which affects the interaction potential between the surfaces of the platelets. The steric repulsion imposed by the oleic acid brush is then suppressed and the nanoplatelets can approach each other more closely. Another effect could also explain why the addition of ethanol leads to the formation of the superparticles. Ethanol is a bad solvent for the aliphatic chain of oleic acid. Hence, when the proportion of ethanol is increased, contact between the brushes of two different platelets will be energetically favored. In other terms, particle/particle contacts (via the bound ligands) are more and more favored as the proportion of bad solvent is increased. The SAXS measurements yield a stacking period of 5.1 nm within the superparticles. With a thickness of 1.2 nm for the platelet, we can deduce that the surfaces of the platelets are 3.9 nm apart. This distance is consistent with the presence of oleic acid molecules at the surface of the nanoplatelets since their complete replacement by ethanol would yield a smaller stacking period. On the other hand, a fully stretched oleic acid molecule is 2.5 nm long, which shows that the aliphatic chains are either interdigitated or collapsed.

We also noted that the amount of ethanol needed to obtain the superparticles varies from batch to batch and depends on the purification protocol of the nanoplatelet dispersion. This is likely due to the variation of the quantity of free oleic acid present in the dispersion at the end of the purification process. As described in the previous chapter, adding oleic acid tends to stabilize the dispersion and delays the onset of NP aggregation.

Finally, we can draw an analogy between these architectures and supra-molecular assemblies of planar  $\pi$ -conjugated molecules which also self-assemble into long anisotropic belts [125–127]. More than their similar structures, these assemblies share also a common synthetic pathway since they are both obtained through addition of an anti-solvent to a solution of dispersed building blocks. A major difference lies in the fact that the nanoplatelets used here are one order of magnitude larger in size. Molecules being small (as compared to nanoparticles), their diffusion is fast and the system can explore numerous configurations until it finds the minimum of free energy. In other terms, these systems are, most of the time, at thermodynamic equilibrium and activation barriers, which need to be overcome to reach equilibrium, are of the order of magnitude of thermal activation. On the contrary, nanoparticles being around 10 times larger, their dynamics is markedly slower and they easily get trapped in glassy states which do not correspond to a global free energy minimum [29]. These out-of-equilibrium configurations can persist

indefinitely, compared to experimental time scales because thermal activation energy is not high enough to overcome the activation barriers leading to more stable configurations. Hence, controlling the self-assembly of nanoparticles requires a careful attention to all the steps of the process from the synthesis to the final assembly.

### **3.3 Conclusion**

In conclusion, we have devised a simple way to organize CdSe nanoplatelets into highly anisotropic micronic superparticles through the destabilization of a colloidal solution by addition of an antisolvent. These superparticles are composed of around  $10^6$  individual nanoparticles and the ordered stacking of the nanoplatelets leads to anisotropic optical properties which could be, in the future, exploited in optoelectronic devices such as LEDs [128].



# Hybrid polymer nanoplatelet films

## 4.1 Introduction

Hybrid materials made of anisotropic metallic or semi-conducting nanoparticles (NPs) dispersed in a polymer matrix have become an exciting class of nanocomposites with promising applications in electronics and optics. For example, the alignment of such materials can improve current transport in electronic devices or modulate the response in optical devices [129, 130]. However, two key points have to be addressed for this purpose. Firstly, a homogeneous dispersion of inorganic nanoparticles in polymeric templates is rather hard to achieve and most often requires surface modification [131–134]. Secondly, the macroscopic orientation of the material, which is required to exploit the anisotropic properties of the individual particles, must be controlled. To date, the orientation of the NPs in polymer matrices is mostly restricted to thin films. For example, nanoparticle alignment could be obtained by stretching a thermoplastic polymer at a temperature close to  $T_g$  or by applying an electric field during solvent casting [130, 135–137]. In all cases, the orientation is irreversible, which precludes applications in opto-mechanical devices, for instance. We describe here how we achieved both a homogeneous dispersion of NPs in a thick film and the reversibility of the orientation in a composite material comprised of CdSe nanoplatelets (NPLs) dispersed within a classical thermoplastic elastomer matrix. To obtain a homogeneous composite material, we carefully adapted the BCP to the oleic acid ligand grafted on the NPLs. The polymer matrix that we have chosen is a commercial thermoplastic elastomer made of Styrene-Butadiene-Styrene (SBS) whose central block is of chemical nature and polarity close to those of oleic acid (Figure 4.1). This chapter is adapted from [4], most of the work has been performed by Dr Emmanuel Beaudoin.

## 4.2 Results and discussion

A crucial advantage of such a matrix is the possibility to stretch it up to high strain levels in a reversible way at room temperature. We prepared homogeneous CdSe/SBS composite films with a CdSe volume fraction of 10% where both the SBS lamellar mi-



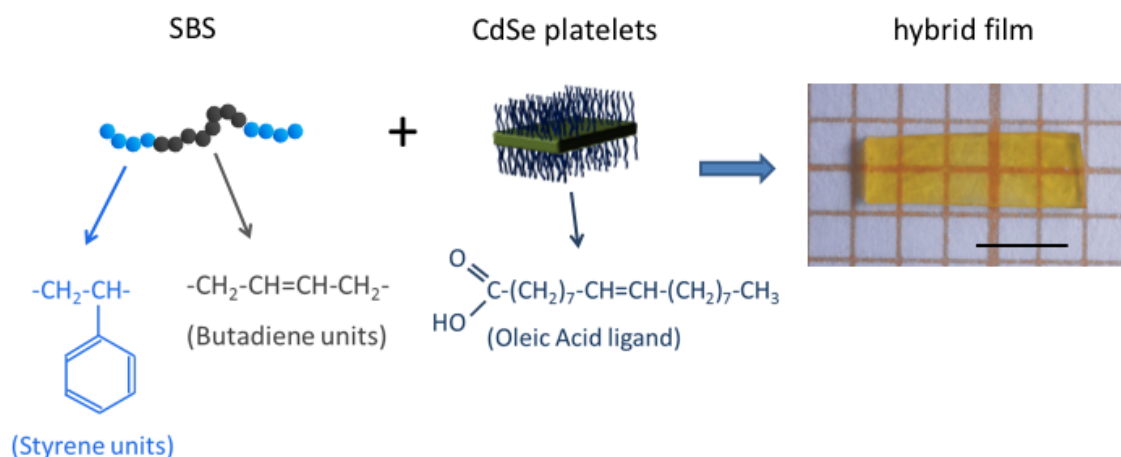


**Figure 4.1:** Components of the hybrid film. Left: schematic representation of a SBS copolymer chain. Center: schematic representation of a CdSe nanoplatelet covered with ligands. Right: photography of the hybrid film (scale bar is 2 mm).

crostructure and the CdSe NPL spectroscopic properties are preserved. The structural properties of these hybrid films were first studied by Transmission Electron Microscopy (TEM) (Figure 4.2a). The TEM images, which display light and dark grey bands corresponding to PS and PB domains respectively, clearly confirm the lamellar morphology of the SBS microstructure. Despite the high load in inorganic nanoparticles, the SBS microstructure in the hybrid films is therefore not much altered compared to that of the pure block copolymer. CdSe platelets have a strong electronic density but are very thin, which explains why the only particles clearly observed on the TEM images are those seen edge-on. Moreover, close inspection of the TEM images reveals that the CdSe platelets are mostly located in the PB domains, which was expected because of the chemical similarity of OA with PB. Very occasionally, a few platelets can be seen in the PS domains, possibly because of some ligand loss during the film preparation (see below). Furthermore, the images show that the platelets self-assemble in short stacks. Indeed, CdSe platelets naturally tend to stack when brought in an unfriendly environment, such as an anti-solvent, in order to maximize ligand-ligand interactions [3, 122]. At this stage, it appears clearly that the growth of the stacks is limited by the rigid PS microdomains.

The lamellar morphology of the hybrid films is confirmed by their Small-angle X-ray Scattering (SAXS) patterns (Figure 4.2.b) that display diffraction peaks whose positions are in 1:2:3:4 ratios. Moreover, the widths of the (001) peaks without and with particles remain comparable. However, close inspection of the diffractograms shows that the position of the (001) peak shifts from  $0.175 \text{ nm}^{-1}$  for pure SBS to  $0.155 \text{ nm}^{-1}$  for the composite material, which corresponds to an increase in the period of the microstructure from 36 nm without nanoplatelets, to 40 nm in presence of nanoplatelets. This 10% increase in the lamellar period agrees with the volume fraction of CdSe in the film and confirms that the platelets are well dispersed within the microstructure. Platelet stacking is also detected in reciprocal space at intermediate wave vectors in the SAXS patterns.

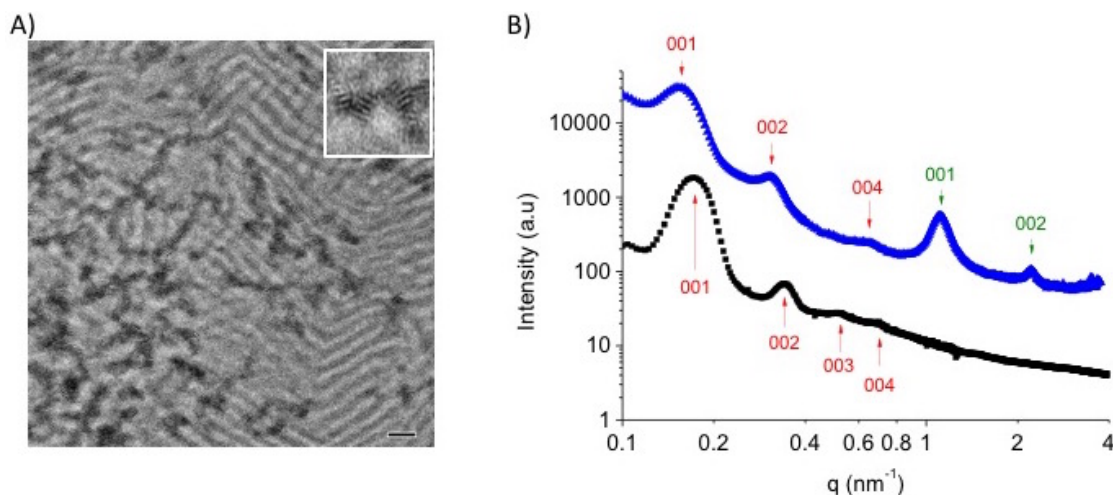


Figure 4.2: Structure of the hybrid material. (a) TEM image of the composite film. Scale bar is 50 nm. Inset is a 3 magnification on NPLs. (b) SAXS diagram of a pure SBS film (square) and of the composite film (triangle). The reflections arising from the lamellar microstructure of the SBS template are indicated in red whereas the reflections due to the NPL stacking are indicated in green.

Two scattering peaks are observed at  $q = 1.1 \text{ nm}^{-1}$  and  $q = 2.2 \text{ nm}^{-1}$ , and correspond to the 001 and 002 reflections of the platelet short stacks. The stacking period of 5.7 nm indicates a 4.5 nm gap between inorganic platelets, in agreement with the presence of almost fully stretched oleic acid molecules on both sides of the NPL. The reflections of both the lamellar microstructure and the platelets stacks are completely isotropic, indicating no preferential orientation in the unstretched films.

Composite films observed by optical fluorescence microscopy display homogeneous fluorescence intensities on the whole field of view, at the micrometer scale, which definitely rules out the presence of macroscopic aggregates (Figure 4.3a-c). Very importantly, the spectroscopic properties of CdSe nanoplatelets are essentially preserved in the composite films. In all samples, the band-edge exciton emission of the nanoplatelets gives rise to a sharp peak at 519 nm (Figure 4.3.b). This value is slightly but significantly higher than the value of 513 nm recorded for the same platelets dispersed in toluene. It has been previously shown that such energy shifts may arise from changes in the effective size of the nanocrystals due to ligand loss or to ligand exchange reactions. [138] These modifications of the surface of the particles are usually also responsible for deep-trap emission at higher wavelengths ( $\approx 650 \text{ nm}$ ) because of an increase in surface defects [138, 139]. Therefore, the reparation of the films. The CdSe/SBS composite films can easily be stretched up to around 100-150%.

The influence of stretching on the structure of the hybrid films was investigated by X-ray scattering (Figure 4.4). At 100% deformation, almost no scattering signal can be detected when the X-ray beam is perpendicular to the film. In contrast, very anisotropic signals are observed at both small and intermediate wave vectors when the X-ray beam

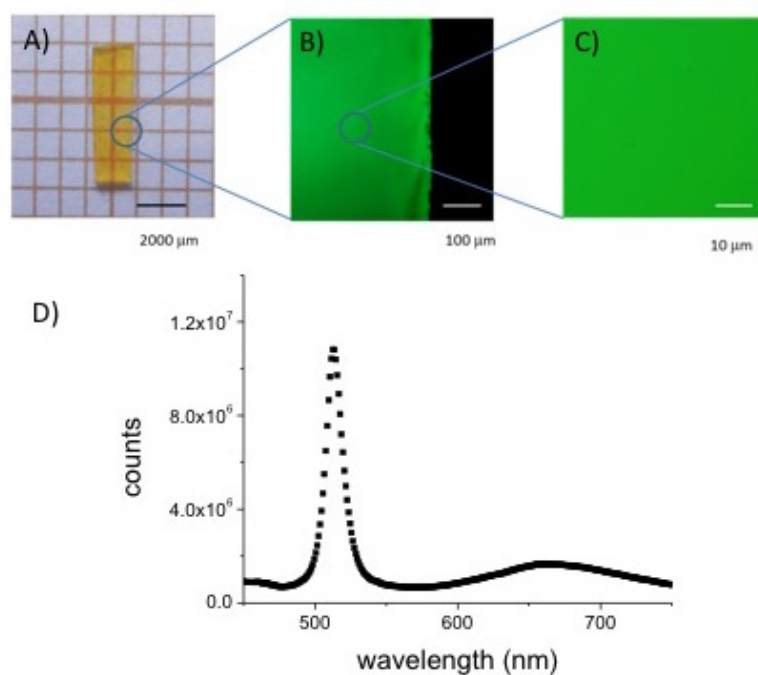


Figure 4.3: Optical properties of the hybrid material at rest. (a) Photograph of the composite film and (b) and (c) optical fluorescence microscopy images of the same film with FITC filter, at different magnifications. (d) Fluorescence spectrum of the same film with excitation at 400 nm.

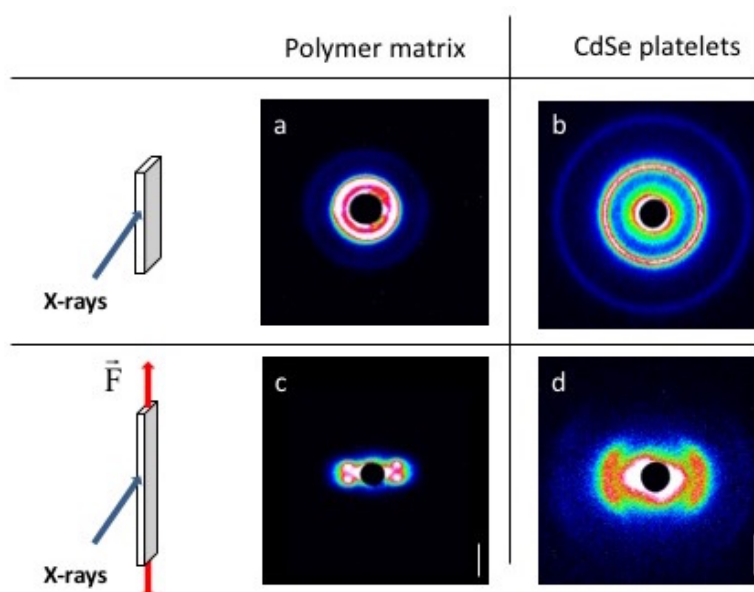


Figure 4.4: Alignment of the hybrid material by stretching: SAXS patterns of the composite film. (a) Scattering from the microdomains of the SBS copolymer at small  $q$ -range, without strain. (b) Scattering from the stacks of NPLs at intermediate  $q$ -range, without strain. (c) Scattering from the micro-domains of the SBS copolymer at small  $q$ -range, 100% strain. (d) Scattering from the stacks of NPLs at intermediate  $q$ -range, 100% strain. Scale bars on figures c and d measure  $0.2$  and  $1 \text{ nm}^{-1}$ , respectively.

is parallel to the film. The anisotropy of the SAXS pattern proves that the layers of the block copolymer orient parallel to the film surface. Such orientation is also observed for the pure SBS films. The peak splitting (see Figure 4.4.c) has already been reported in the literature for SBS copolymers and was attributed to a zig-zag texture of the lamellar phase [140, 141]. This texture arises from a mechanical instability upon stretching where lamellar domains alternately reorient at some angle with respect to the stretching direction. X-ray scattering at intermediate q-range (Figure 4.4.d), shows that the platelets align parallel to the lamellar domains (i.e. the platelet normals align parallel to the layer normals). The zig-zag texture also induces a splitting of the stacking reflections of the platelets. The angular spread of the stacking reflections suggests that the platelets are well aligned and it can be used to quantify the orientation degree of the NPLs by calculating the nematic order parameter  $S$  [142]. This parameter is 0 for unaligned objects and 1 for perfectly aligned particles. The nematic order parameter  $S$  of the platelets reaches here values of the order of  $S \approx 0.6$  at 100% strain, which is quite comparable to the orientational order of usual liquid crystals for instance. The CdSe NPLs are only weakly confined since their dimensions ( $\approx 10$  nm) are smaller than the thickness ( $\approx 20$  nm) of the PB domains of the lamellar microstructure. Therefore, the mechanism of orientational coupling of the nanoplatelets with the lamellar matrix may not be purely due to the steric confinement of the NPLs within the lamellar microstructure. Upon stretching, both the layers and the PB chains align parallel to the stretching direction. Then, the CdSe platelets are likely to align parallel to the PB chains in order to avoid altering their conformation.

The photoluminescence of stretched films is highly anisotropic, in contrast with that of unstretched films which is completely isotropic (Figure 4.5). This can readily be observed visually with a fluorescence microscope equipped with a polarizer. These observations confirm the fact that the fluorescence light is polarized in the plane of the nanoplatelets [3]. The anisotropy of fluorescence can also be quantified by measuring the photoluminescence intensity with a fluorescence spectrometer using an analyzer placed after the sample. When the analyzer axis is set parallel (resp. perpendicular) to the film, a fluorescence intensity  $I_{\parallel}$  (resp.  $I_{\perp}$ ) is measured. The anisotropy is usually quantified by the ratio  $r = (I_{\perp} - I_{\parallel}) / (2I_{\parallel} + I_{\perp})$  [143]. This parameter  $r$  increases from 0 for the film at rest to  $\approx -0.25$  for the film at 100% strain. A simple model (see supplementary materials of [4]) gives  $r = -S/2$ , so that  $S \approx 0.50$ , in fair agreement with the value ( $S \approx 0.60$ ) previously obtained by X-ray scattering. This confirms that film stretching gives rise to a strong orientation of the nanoplatelets and a highly anisotropic photoluminescence, with light emission polarized parallel to the film. The level of anisotropy depends on the strain and the samples become again isotropic when the stress is removed and deformation relaxes.

### 4.3 Conclusion

Homogeneous dispersion of semiconducting nanoplatelets in a thick film was achieved by carefully selecting a thermoplastic BCP matrix compatible with the ligand brush grafted on the nanoparticles. Moreover, the tendency of CdSe NPLs to stacking is lim-

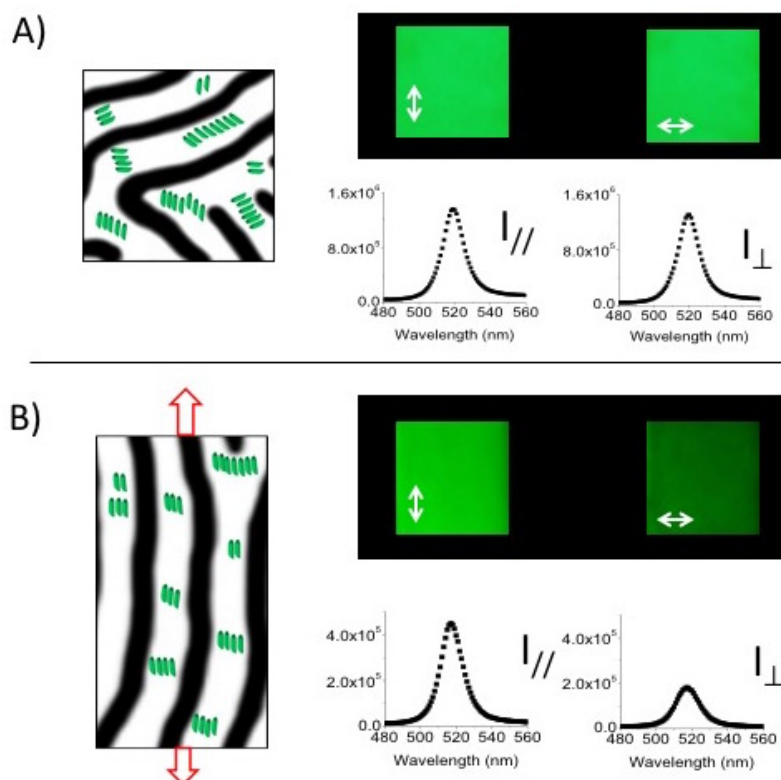


Figure 4.5: Effect of stretching on the fluorescence properties of the hybrid material: schematic representation of a composite film, optical microscopy and emission spectra of, (a) film at rest showing isotropic photoluminescence; (b) stretched film (100% strain) showing anisotropic photoluminescence. The white arrows represent the direction of the analyzer.

ited by the confinement within the PB domains of the BCP structure at the microscopic scale, resulting in optically homogeneous composite materials. Stretching these composites provides an easy way of controlling particle orientation. This alignment is reversible as relaxing the samples immediately restores the initial isotropic distribution of the nanoplatelets. From a fundamental point of view, this allows investigating in detail the NPL anisotropic physical properties, as was shown above in the case of photoluminescence. From a more applied point of view, polarization effects are useful for modulating the optical response (absorption and/or photoemission) in materials. For example, the polarized photoemission of aligned CdSe NPLs could prove useful for emitters in lasers [144], because the concentration of the emission in a single polarization state may reduce the operating power. More generally, the present approach may be also applied to other types of composite films comprised of nanosheets, such as graphene or clays, whose mechanical or barrier properties strongly depend on filler orientation.



# CdSe Nanoplatelets Polymers

## 5.1 Introduction

In a previous chapter, we have seen that a fast destabilization of a NPL colloidal dispersion yielded very anisotropic needles with lateral dimensions measuring around 200 nm (tens of NPLs). Here, we show that slow drying of a NPL colloid yield threads with a lateral extension limited to one nanoplatelet. These objects share many features with living polymers with, in this case, the monomer being a nanoplatelet. Examples of spontaneous assembly of metallic colloidal particles in one-dimensional (1D) polymer-like structures have been reported recently. The most common geometry is (possibly branched) chains that are called “plasmonic polymers” since they give rise to a shift in the plasmon resonance of the nanocrystals. The spontaneous assembly of particles into chains was achieved by chemical cross-linking, physical attraction between ligands, or oriented attachment of nanocrystals [145–149]. The aggregation number of these polymeric assemblies is usually comprised between 5 and 20. However, there is not to date any such report of polymeric 1-D assembly for colloidal quantum wells.

## 5.2 Results and discussion

Here, we demonstrate a simple strategy to induce the self-assembly of CdSe NPL into micron-long threads by adding small amounts of oleic acid (OA) to a NPL dispersion, followed by slow drying. Once the threads are formed during drying, they can be easily redispersed. The concentration of added oleic acid is a critical factor that controls the assembly and the length of the threads. The fluorescence of the nanoplatelets is not quenched during their assembly and the threads, either dried on a substrate or redispersed in solution, are visible by fluorescence microscopy. Furthermore, the threads can be used as seeds for further growth like in living polymers where monomers can be added to reactive ends of an already polymerized chain. 4-monolayer (ML), almost square CdSe NPL were synthesized as described in section A.1.1. An excess of oleic acid is injected at the end of the synthesis so that all faces of the NPL are fully covered by

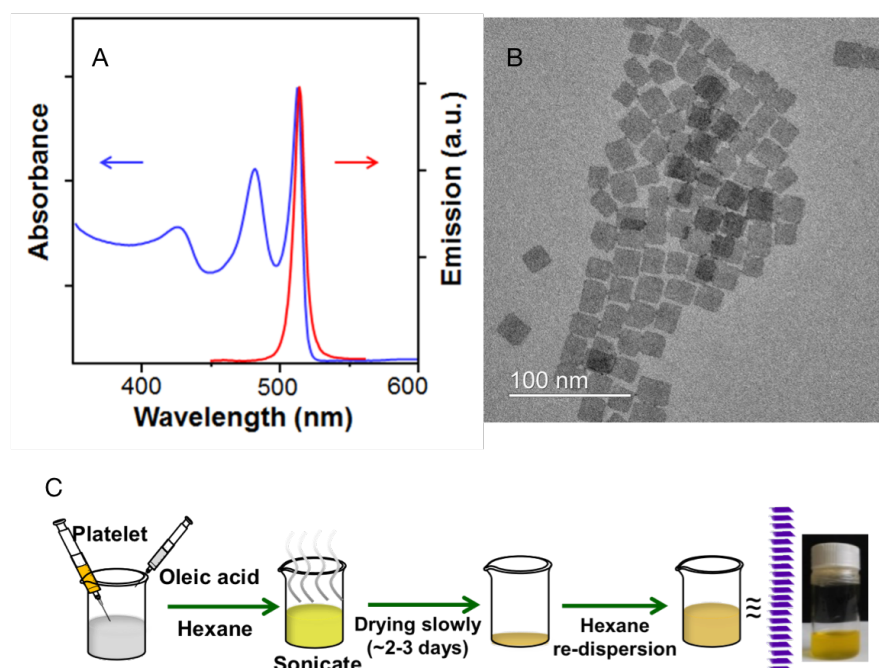
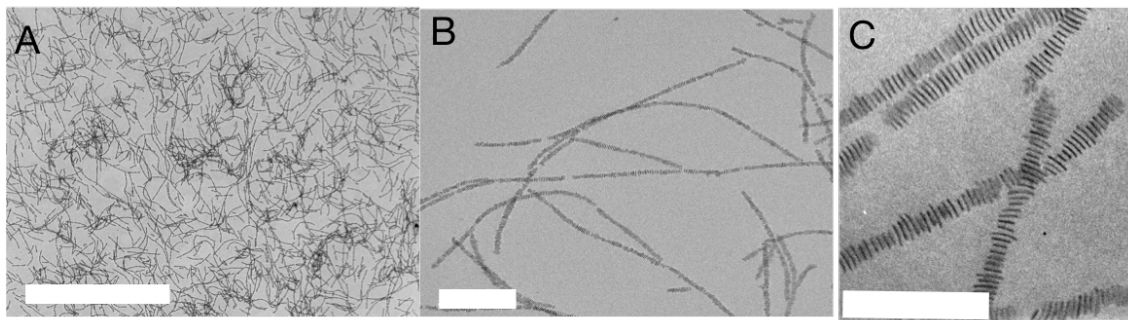


Figure 5.1: A) UV-VIS absorbance and emission spectra and B) TEM images of NPLs solutions used for the self-assembly. C) Scheme of the procedure for preparing self-assembled threads of CdSe platelets.

ligands. After thorough purification through repeated precipitation/redispersion cycles, the NPL were dispersed in hexane. The absorption and emission spectra (Figure) show that only one 4ML population was found in solution. Moreover, the transmission electron microscopy (TEM) images (Figure 5.1.b) of the platelets showed that the 4 ML NPL are square with  $\approx 18$  nm edges.

CdSe NPL self-assembly was achieved at ambient conditions through a two-step process (Figure 5.1.c). First, a small quantity of oleic acid was added to the NPL dispersion in hexane. Since we identified the OA concentration as a critical parameter (see below), we ensured by IR spectroscopy that no free OA was present in solution prior to this addition and that all the OA was bound to the surface of the NPL. Afterwards, the dispersion was slowly dried by leaving the vial open. The complete drying of the solvent took between 2 and 3 days. At the end of the drying process, a yellow deposit was visible at the bottom of the vial and could easily be re-dispersed though gentle stirring. A slightly turbid dispersion was then obtained (Figure 5.1.c, photograph), indicating the presence of large objects scattering light in solution. Electron microscopy observation of these dispersions dried on a carbon-coated TEM grid reveals the presence of self-assembled threads (Figure 5.2). The length of the threads reached up to several micrometers while they were composed of a single platelet along their transverse dimensions. Hence, the NPLs are only stacked face to face and no edge-to-edge stacking was observed. This con-



**Figure 5.2:** (A) and (B): lower and higher magnification TEM images of threads of 4 ML square platelets. (C) High-resolution TEM image of the threads showing the face to face stacking of CdSe platelets. Scale bars: (A)  $5\ \mu\text{m}$ , (B)  $200\ \text{nm}$ , (C)  $20\ \text{nm}$

trasts with our previous report of micrometer needles (see chapter 3) where both types of stacking were observed simultaneously.

The small-angle X-ray scattering (SAXS) pattern of the dispersion (Figure 5.3) displays several features consistent with the threaded structure observed by TEM. An intense peak at a scattering vector  $q^* = 1.23\ \text{nm}^{-1}$  arises from the stacking of the platelets with a period  $d = 2\pi/q^* = 5.1\ \text{nm}$  within the CdSe threads. Both SAXS measurements and high-resolution TEM images show that the NP are stacked in threads with a period of  $5.1\ \text{nm}$ . Since the platelet thickness is  $1.2\ \text{nm}$ , the faces of neighboring platelets are  $3.9\ \text{nm}$  apart. This separation is due to oleic acid molecules bound to the faces of the NPL. However, the length of a fully-stretched oleic acid chain is  $2.5\ \text{nm}$  and therefore, the oleic acid brush must be partially inter-digitated, as already reported. Interestingly, the fluorescence of CdSe NPL is not quenched by their self-assembly and the threads on a glass substrate are easily detected by fluorescence microscopy (Figure 5.3).

Although the lateral spatial resolution of the confocal microscope is of the order of  $200\ \text{nm}$ , we can clearly see the elongated character of the threads using this technique. Another interesting feature, shown by both the electron and fluorescence microscopies, is the absence of individual NPL in solution besides the threads. All the platelets take part in the self-assembly process and none are present as “monomers” in solution. Due to their large aspect ratio, these threads are not completely straight and appear somewhat flexible. The threads therefore share similarities with giant wormlike micelles observed in some surfactant [150] or block copolymers [151] solutions. A noticeable difference being that, in the case of surfactant micelles, monomers (i.e. single surfactant molecules) are continuously exchanged between the solution and the aggregates whereas here, relatively large parts of the threads detach and re-attach dynamically. This is visible on figure 5.4 where a thread fragment measuring around  $250\ \text{nm}$  long (and hence made of around 50 NPLs) separates from a large thread and then re-merges with it after drifting in solution for a few seconds.

By tuning the amount of added oleic acid, it is possible to control precisely the mean thread length (Figure 5.5). Without any further addition of oleic acid, single platelets

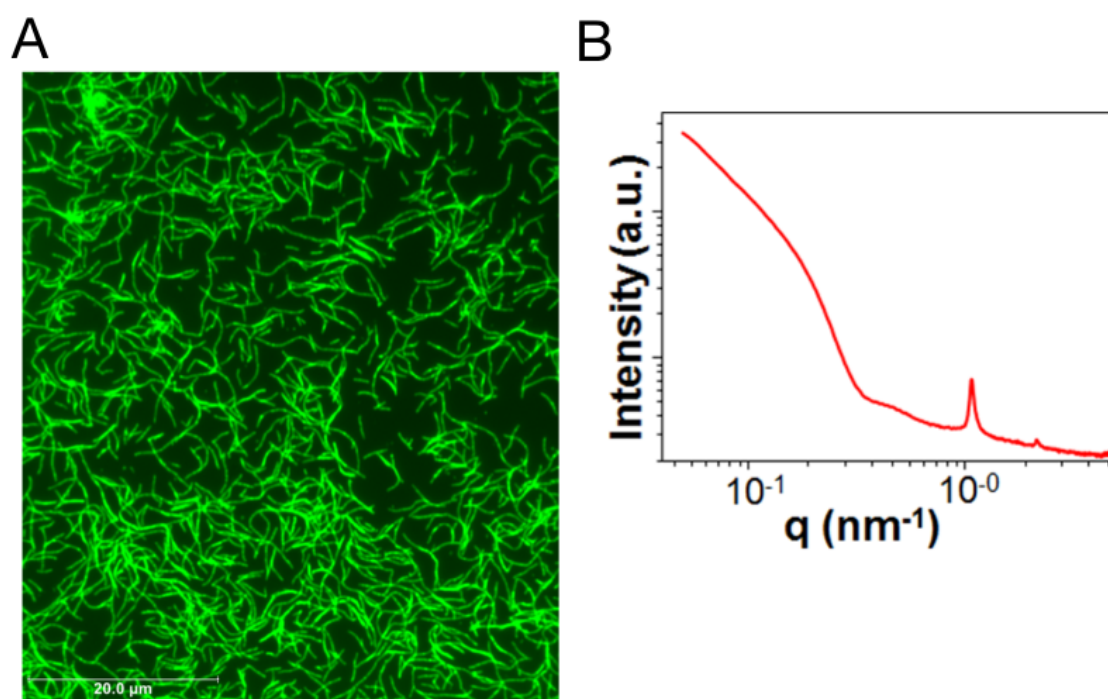


Figure 5.3: A) Fluorescence microscopy images of the threads deposited from solution on a cover slip. (B) Small angle X-ray scattering curve of the thread dispersion.

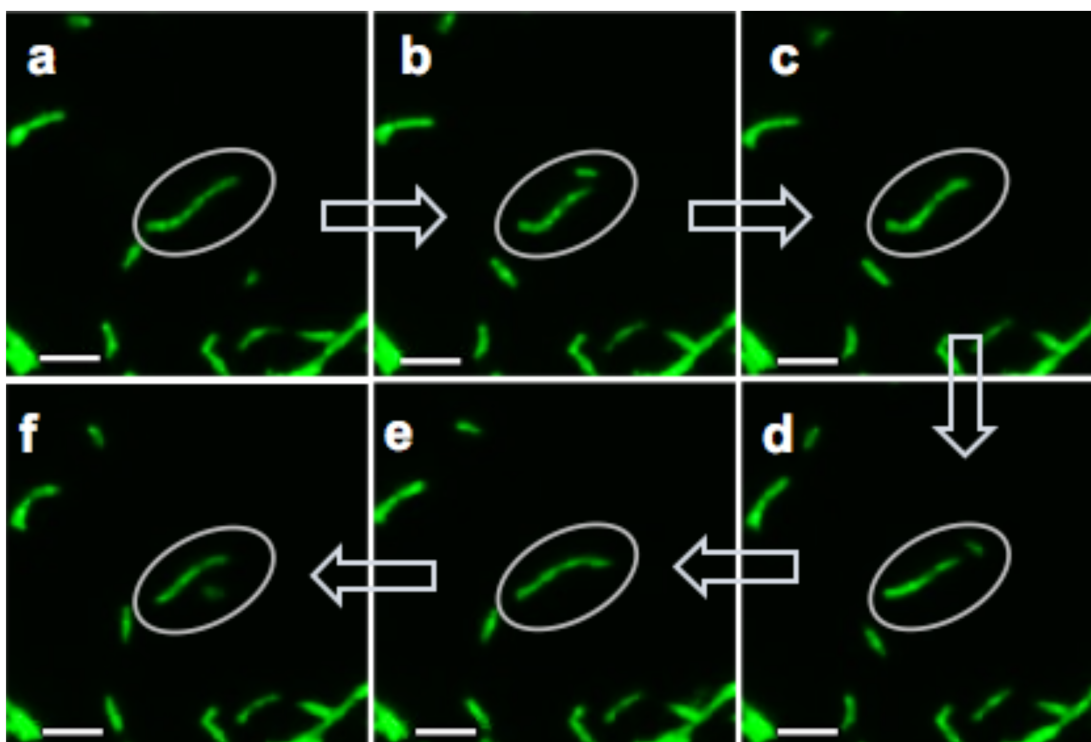
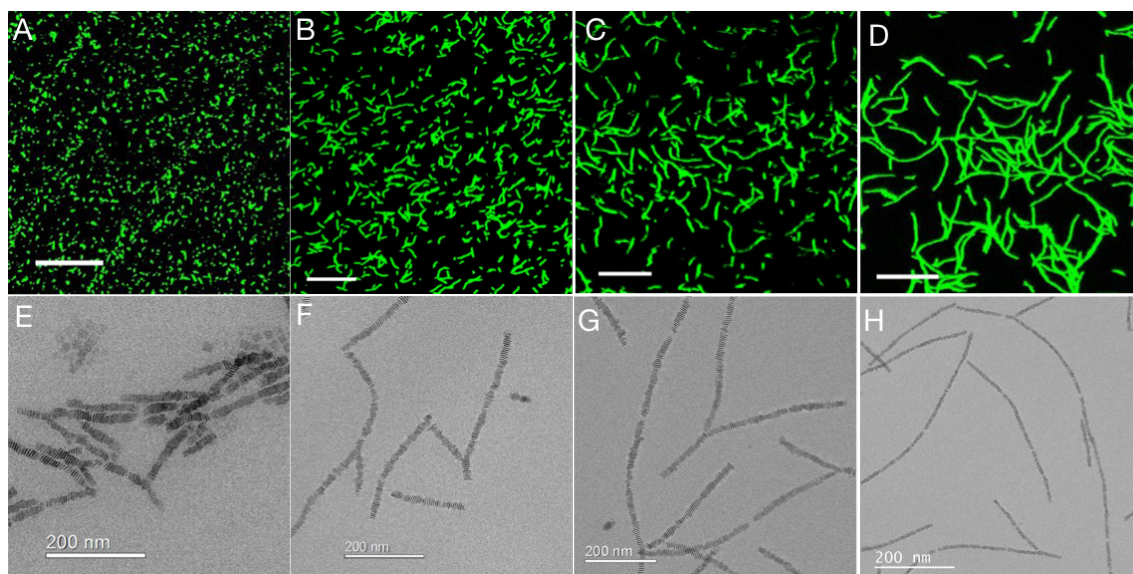


Figure 5.4: Image sequence showing the breaking and recombining of a threads under thermal agitation.





**Figure 5.5:** Evolution of threads of square CdSe platelets using different concentrations of added OA. (A-D) Confocal Fluorescence microscopy images of the threads obtained with different concentrations of OA, 6 mM, 16 mM, 32 mM, and 48 mM, respectively. (scale bars: 5  $\mu\text{m}$ ). (E-H) Corresponding TEM images of CdSe threads. (scale bars: 200 nm)

and very short platelet stacks are found in suspension. For an oleic acid concentration of 6 mM, the CdSe NPL stack and form small threads of length 100-200 nm. The length of the threads further increases up to a mean length of 1.4  $\mu\text{m}$  for  $[\text{OA}]=48$  mM. This dependence of thread length on added oleic acid concentration is also clearly observed by fluorescence confocal microscopy although the threads of smallest size only appear as small bright spots since they are smaller than the lateral resolution of the microscope (Figure 5.5.a-d). After reaching a maximum for an oleic acid concentration of 48 mM, further ligand addition resulted in the precipitation of the colloid. Whatever their length, the width of the CdSe threads always remained equal to the edge length of the platelets.

A key factor influencing the self-assembly of NPL into threads is the monodispersity in shape of the initial NPL: a well-defined square NPL shape is required for self-assembly. Irregular platelets, formed through small changes in reaction temperature or annealing time, led to very short stacks or even to random aggregates. Hence, the self-assembly process is not highly tolerant to small deviations in the shape of the nanoparticles. While the results presented here were obtained with 4 ML nanoplatelets, we achieved similar outcome with thicker 5 ML with a board-like geometry. In this case, the platelets have two lateral dimensions (Figure 5.6): the shorter one is around 7 nm and the larger one around 20 nm. As shown in Figure 5.6, TEM examination of samples made of 5 ML platelets and prepared in a similar fashion also display threaded structures.

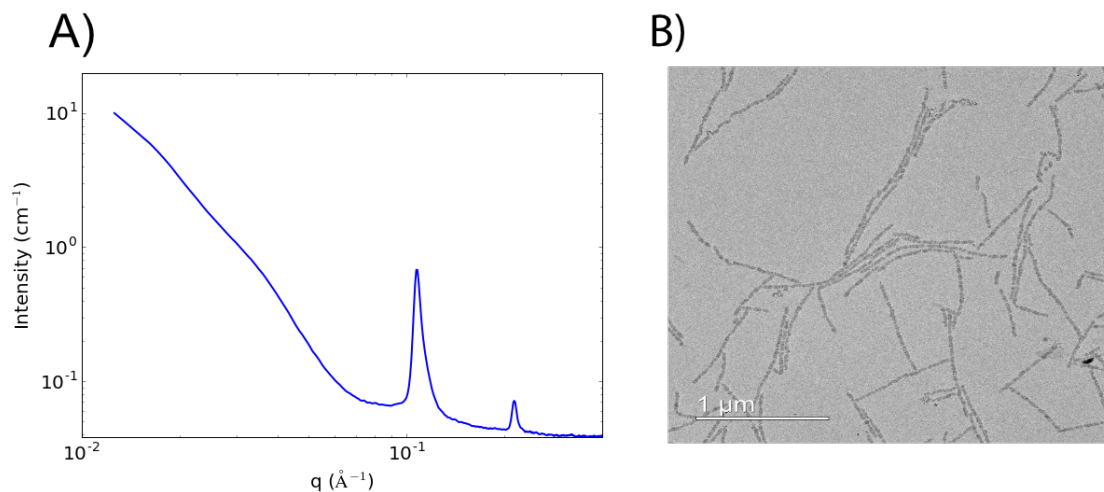


Figure 5.6: Characterization of living threads made of 5ML NPLs: A) SAXS pattern showing the lamellar structure of the threads. B) TEM image showing the threads.

We now turn to the mechanism by which self-assembly occurs and we try to propose a physical explanation to the influence of OA concentration on the thread length. If we consider a simple model of one-dimensional self-assembly induced by a favorable interaction between the NPL (monomers), there is a critical concentration,  $c^*$ , beyond which self-assembly occurs [52]. In a previous chapter, we have shown that CdSe NPL dispersions are not colloidal stable indefinitely and that the precipitation time decreases with increasing concentration. Hence, we can also define another concentration,  $c_p$ , at which the dispersion becomes unstable and precipitates without self-organizing. Upon drying, the concentration of the dispersion increases and the relative values of  $c^*$  and  $c_p$  will govern the behavior of the suspension. If  $c_p < c^*$ , the first concentration reached upon drying is  $c_p$ . Hence, the dispersion will precipitate and no threads are seen upon re-dispersion. If  $c^* < c_p$ , self-assembly will occur before aggregation and threads will form. Upon further evaporation, these threads will precipitate but they will still be present and visible when new solvent will be added. This simple model explains the different experimental features observed here. We previously showed that the oleic acid concentration could tune the colloidal stability of NPL dispersions and an optimum OA concentration was found. Below this optimum, increasing [OA] leads to more stable dispersions (hence higher  $c_p$ ) while further increase beyond leads to lower stability (smaller  $c_p$ ). This explains the experimental trends observed. With higher [OA],  $c_p$  increases and becomes larger than  $c^*$ . Hence,  $c^*$  is reached before  $c_p$  during drying and self-assembly occurs before precipitation. Within the same modeling framework, the size of the threads is expected to scale with NPL concentration. This is consistent with larger threads being observed for higher oleic acid concentrations.

In the field of macromolecular synthesis, the expression “living” usually refers to re-



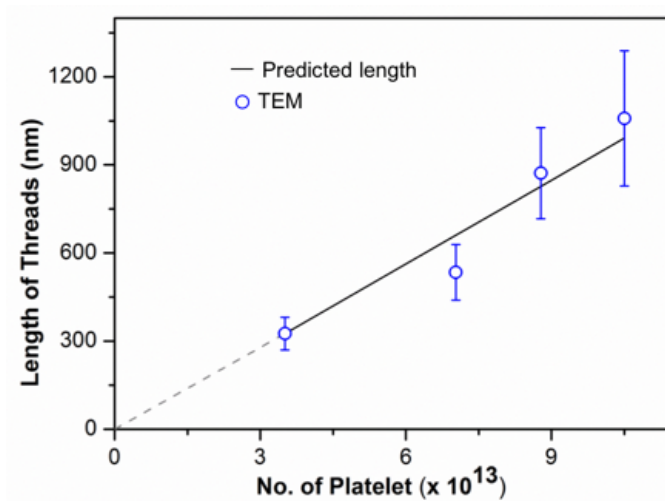


Figure 5.7: A) Length polydispersity distributions of CdSe NP threads for different concentrations of added OA. B) Dependence of the thread average length on the concentration of OA added to the platelet solution in hexane.

active macromolecules which can grow when supplementary monomers are added in solution [152, 153]. Since the chain ends are reactive, new monomers attach to existing chains and the mean chain length (polymerization degree) increases while the number of macromolecules remains constant. In order to investigate whether the CdSe NPL threads feature this property, we prepared "small" ( $\approx 300$  nm) threads, re-dispersed them in a solution of free platelets and slowly evaporated the solvent. If the new NPLs only attach to the existing threads and do not form new threads, the contour length will increase by an amount proportional to  $C_{\text{NPL}}/n_0$  where  $C_{\text{NPL}}$  is the concentration of NPL added and  $n_0$  is the initial number of threads in solution. Hence if we plot the contour length as a function of the quantity of added NPLs we should obtain a straight line. This is actually what is observed (Figure 5.7); the threads grew to an extent simply predictable from the amount of added NPL. Of course, the bonds between the NPLs within the threads are weaker than covalent bonds in traditional living polymers. This is why some parts may detach under the effect of thermal agitation as described previously. We are situated in an intermediate case between wormlike micelles and covalent living polymers. In wormlike micelles, the aggregates break and detach very fast since the bonding energy is well below  $kT$ ; these structures do not persist over observable timescales. For higher energy covalent bond strength, like in living molecular polymers, the structure is fixed while the ends are still reactive. Our system shares similarities with both types of self-assembled structure due to the intermediate energy which bonds the building blocks together.

### 5.3 Conclusion

In conclusion, we have developed a simple method to self-assemble CdSe nanoplatelets into long flexible threads through slow evaporation of colloidal solutions. These threads are composed of hundreds to thousands of individual platelets. We can control the average number of platelets per threads with the concentration of added oleic acid or through subsequent re-growth of existing threads. We expect this control over their self-assembly to yield interesting developments in the study of emerging properties in ensembles of NPL. In principle, the simple procedure described here could also be potentially generalized to other systems of 2-dimensional colloidal nanocrystals.



## Twisted Threads

In the previous chapter, we described how long threads composed of CdSe nanoplatelets can be synthesized through the slow drying of colloidal dispersions. We showed that the content of oleic acid was an important factor affecting the final length of the threads. Here, we show that adding oleic acid gradually during the formation of the threads leads to twisted threads with a well defined pitch. This discovery has been made by S. Jana during his post-doc and these results are not published yet. I present here the work performed on this topic and our current understanding of the twisting of these CdSe threads.

### 6.1 Formation and structure of twisted threads

We use 5ML nanoplatelets synthesized as described in the experimental section. Figure 6.1 shows absorbance and emission spectra of the NPLs dispersion after purification. The characteristic features of this NPL population (emission peak at 550 nm, absorbance peaks at 550 and 518 nm) are visible and substantiate the purity of the sample. Electron microscopy shows that the NPLs are board-like, with mean lateral dimensions of 7 and 22 nm.

A drying scheme similar to the one described in the previous chapter was used here. However, instead of introducing a tunable quantity of oleic acid before drying of the colloidal dispersion, the total quantity was divided in equal amounts and added at regular intervals in the dispersion *during* drying. For example, for a total amount of OA of 18  $\mu\text{L}$ , 6  $\mu\text{L}$  is added at the start of the drying process, 6  $\mu\text{L}$  after one third of the total solution volume is evaporated (usually corresponding to one day of drying) and the remaining 6  $\mu\text{L}$  after 2/3 of the solution is evaporated. Afterwards, the precipitate is re-dispersed in hexane. TEM examination of the resulting product shows the presence of long threads (Figure 6.2) with a typical size ranging from 1 to 2  $\mu\text{m}$ . Closer observation reveals that the threads are twisted. Instead of stacking face to face with their edges parallel, a given NPL in a thread is shifted by a small angle with respect to the previous NPL in the same thread. As a result, a spatial periodicity appears along the thread. The

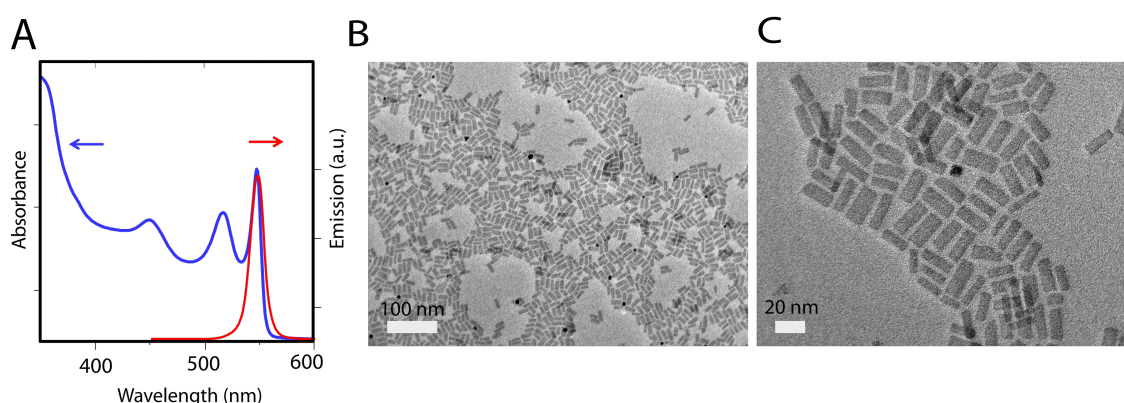


**Figure 6.1:** A) Absorption and emission spectra of the 5 ML NPL dispersion used for the self-assembly of twisted stacks. B) Representative TEM images of the NPL.

typical distance over which a full rotation is achieved (pitch) is around 400 nm.

Figure 6.3 shows the SAXS pattern of a dispersion of twisted threads which exhibits two peaks at respectively  $0.1075$  and  $0.2141 \text{ \AA}^{-1}$  corresponding to a center-to-center distance of 5.84 nm. With this distance in mind, we can deduce that there are around 70 NPLs in one pitch and the mean rotation between two adjacent NPLs is  $5^\circ$ . Electron tomography (Figure 6.2.E) on an individual thread reveals details in their structure, confirming the twisted nature of the thread. We can also notice the presence of vacancy defects in the stack i.e. places where it seems to lack one platelet. It is also visible that the shift between two adjacent platelets within a thread is not constant. In some thread portions, the platelets are almost not shifted whereas fast rotation is observed in other portions.

In order to assess the chirality of the threads, we performed circular dichroism experiments. We did not detect any optical activity in the visible range showing that threads dispersions are racemic mixtures with equal concentration of right and left handed threads. This shows that there is no preferential chirality in the self-assembly process and that whether a given thread is left or right handed is determined by initial fluctuations with equal probability.

As previously observed for straight threads, the overall quantity of oleic acid in the media influences the length of the threads. In Figure 6.4, TEM micrographs of twisted threads with two different oleic acid concentrations are shown. It is obvious that large OA concentrations induce the formation of much larger threads. For a volume of  $18 \mu\text{L}$ , added in three times, small twisted threads with a length below  $1 \mu\text{m}$  are visible whereas very long threads of several microns can be formed with a larger quantity of oleic ( $45 \mu\text{L}$ , also added in three equal portions during the drying).

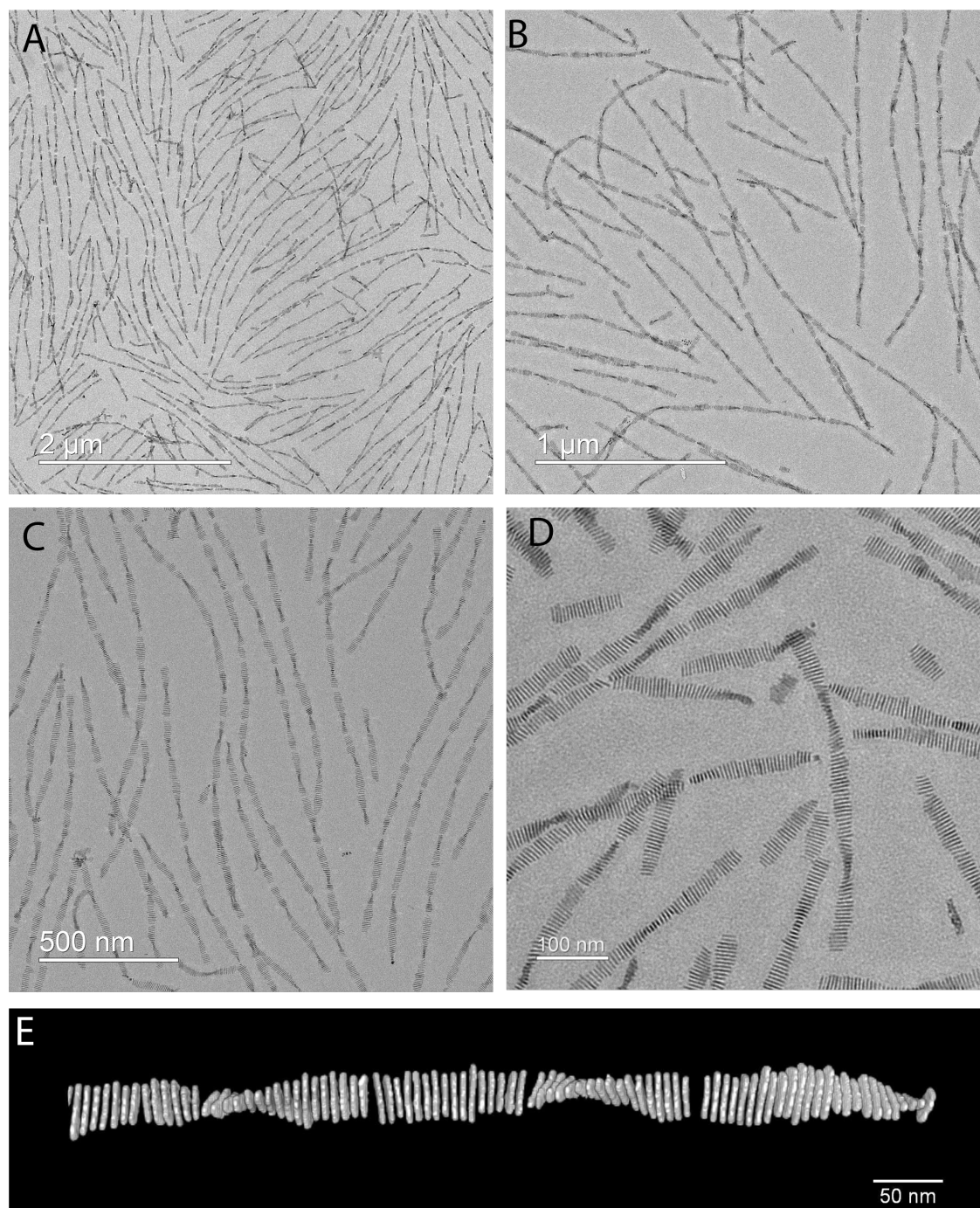


Figure 6.2: A-D) Transmission electron microscopy of twisted thread obtained after drying of a 5 monolayers “board-like” nanoplatelets dispersion at different magnification. E) Electron tomography image of a single twisted thread obtained by Dr M. De Frutos at LPS by acquisition of numerous conventional TEM images at different tilt angle followed by reconstruction.

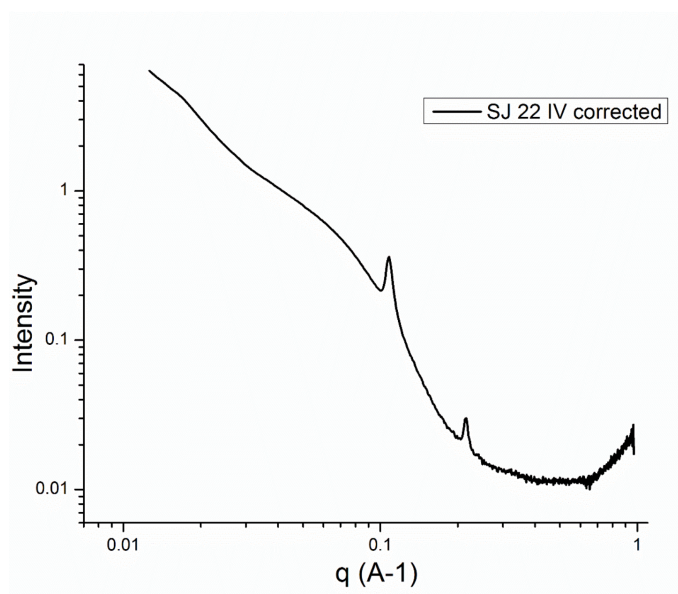


Figure 6.3: Small angle X-ray scattering pattern of a twisted threads.

## 6.2 Formation mechanism

We analyzed the structure of the threads by SAXS and TEM at different steps of the self-assembly process in order to get insight into their formation mechanism. Figure 6.5 shows TEM images of the threads after one third of the solution (first step) is evaporated (before the second addition of oleic acid), after two thirds of the solution is evaporated (second step) and the final product after re-dispersion. We notice that, at the first step, threads are already present in solution but they are *not* twisted. In contrast, some threads at the second step are twisted but we do not observe a regular pitch like in the final state where we recover a structure already described previously. Careful examination of TEM images of the second step (not shown) suggest that twisting starts to occur at random locations in some threads but not all threads are twisted. SAXS patterns of the three different solutions are presented on Figure 6.6. The two peaks indicating the stacking of the NPLs are present at all the stages of the formation and their positions do not move. The only differences are noticed at smaller wavevectors. As the twisting proceeds, the scattered intensity at low  $q$  diminishes while it increases at intermediate  $q$  comprised between  $0.07$  and  $0.1 \text{ \AA}^{-1}$ . Altogether, these results suggest that the twisted threads form through the deformation of existing straight threads under the combined effect of oleic acid addition and evaporation.

## 6.3 Twisting of individual nanoplatelets

In order to disentangle the effects of drying and oleic acid addition, we conducted control experiments where increasing amounts of oleic acid are added to a dispersion of



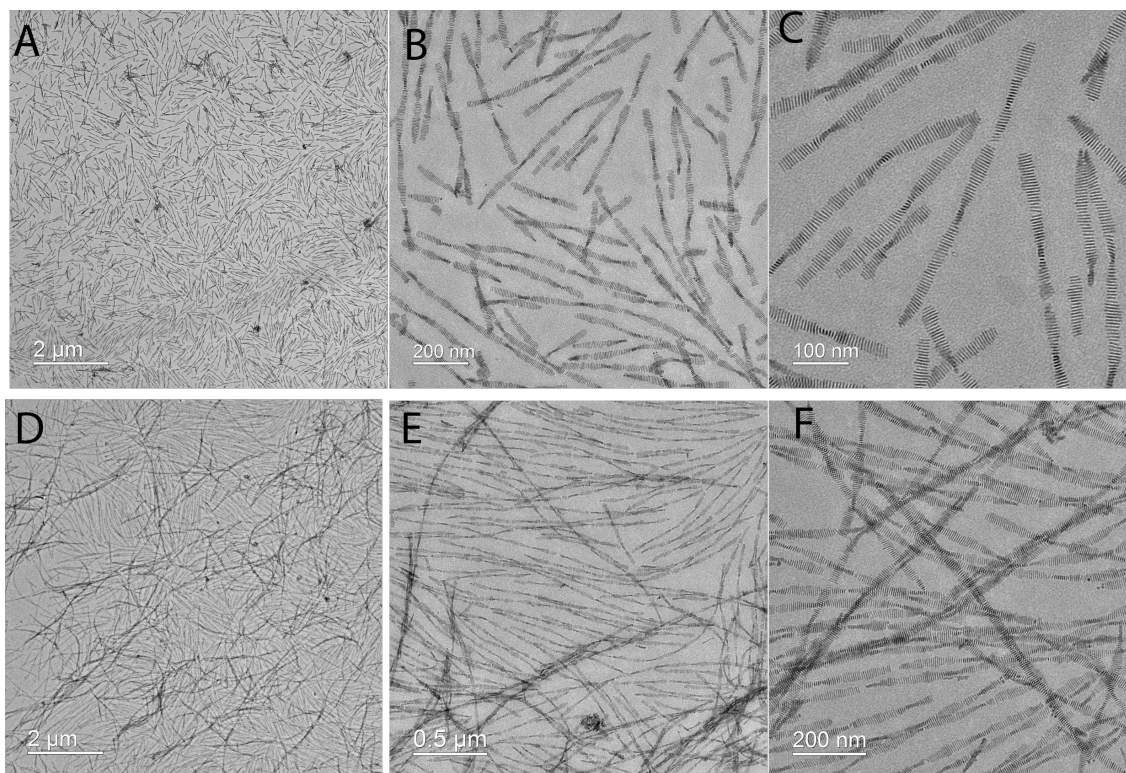


Figure 6.4: Effect of the total amount of oleic acid added to the dispersion on the length of twisted threads. A, B and C) Total amount of  $18 \mu\text{L}$  of OA added to the dispersion. D, E and F) Total amount of  $45 \mu\text{L}$  added to the dispersion.

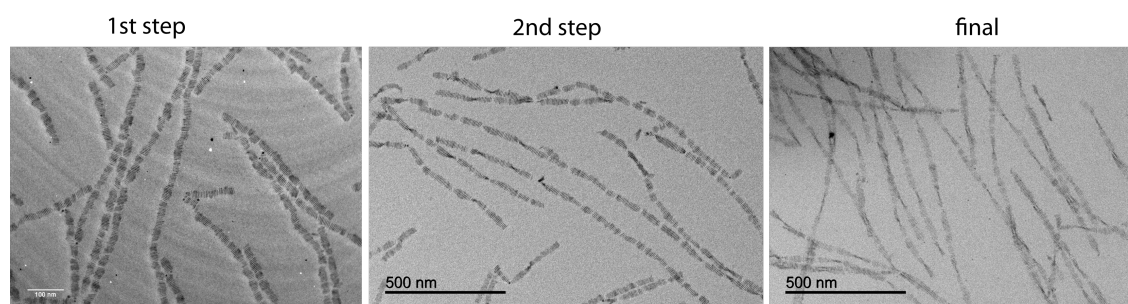


Figure 6.5: TEM images of threads during and at the end of their formation. The first step corresponds to the point where one third of the solution has dried, just prior the second addition of OA. The second step is when two third of the solution has dried. The final state designate the threads re-dispersed in hexane.

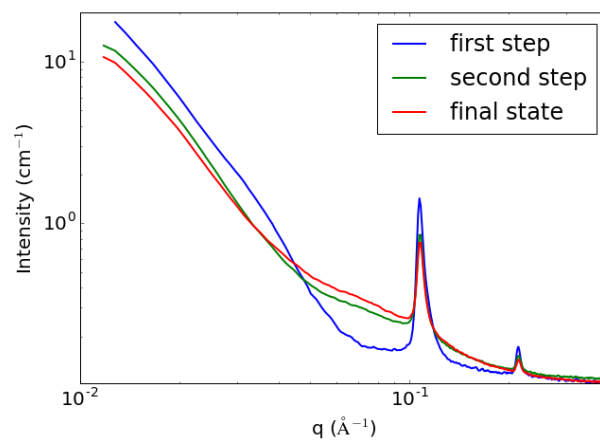


Figure 6.6: SAXS patterns of the thread dispersion for the different formation steps.

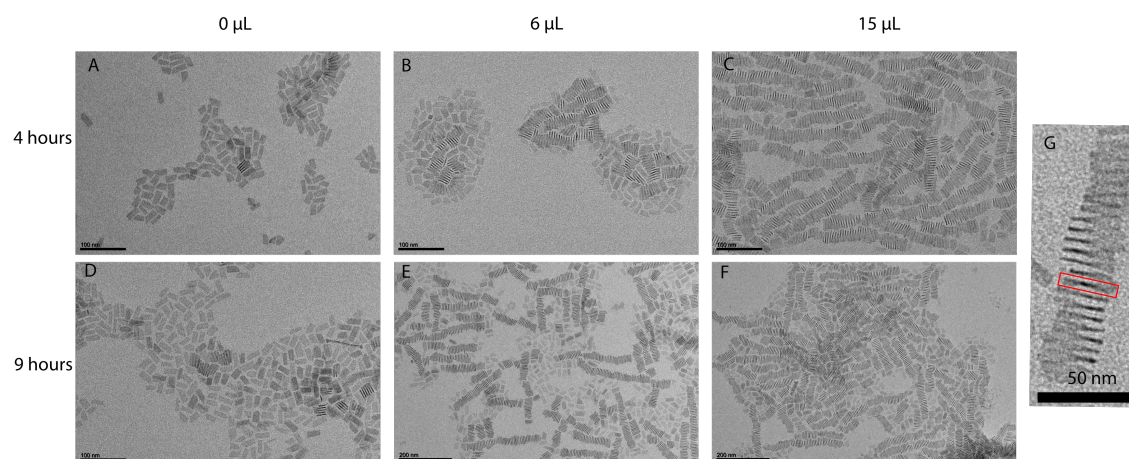


Figure 6.7: TEM images of NPLs as a function of time and volume of oleic acid added to the dispersion.

NPLs without drying. Figure 6.7 shows TEM images of NPLs with different amounts of oleic acid at two different times: 4 and 9 hours after the addition. When no oleic acid is added (Figure 6.7.A.), flat individual NPLs laying with their transverse direction perpendicular to the substrate. As the amount of oleic acid increases, we observe that some NPLs twist. In this twisted configuration two parts of the same platelet have orthogonal transverse direction. One part still has its transverse direction perpendicular to the substrate but another part has its transverse direction parallel to the carbon foil of the TEM grid. This structure is clearly visible on Figure 6.7.G. In some cases, three different parts of the NPLs are visible, the two extremities have the same transverse directions whereas the center is perpendicular (see red rectangle in Figure 6.7.G). The relative proportion of the two different orientations within a single NPL varies. Some are divided in two halves with perpendicular transverse directions whereas in some cases, only a small fraction of the NPL is twisted.

As the amount of oleic acid increases, the proportion of twisted NPLs increases. 4 hours after the addition of 15  $\mu\text{L}$  of oleic acid, almost all the NPLs are twisted. For a given volume of oleic acid, the proportion of twisted NPLs increases with time showing that the twisting is not immediate. Moreover, the twisting is concomitant with a loss of colloidal stability of the dispersion. It is noteworthy that we could not observe isolated twisted NPLs by TEM. Twisted NPLs are all stacked one on top of each other into short piles comprising a few tens of NPLs. These two facts add up to suggest that twisting is induced by the interaction between two (or three) neighboring NPLs. The role of oleic acid seems to speed up the twisting process, since the proportion of twisted NPLs is increasing with time whatever the acid content. Moreover, it has been noted by S. Ithurria in her PhD thesis that this twisting occurs over months even in purified dispersion of NPLs [154].

## 6.4 Discussion

The physical origin of the striking phenomena observed in this chapter can not be maintained with certainty today but we can discuss it in light of the experimental facts described earlier. On the twisting of the individual NPLs, we previously noticed that thinner 3 ML NPLs also have a strong tendency towards bending. As described in [20], NPLs with large lateral extensions fold into nanotubes. In this case, the folding always occurs along the [110] direction irrespective of the crystallographic orientation of the NPLs edges. The formation of these folded and twisted structures points towards an asymmetric source of strain. This is at first surprising since the top and the bottom of the NPLs are equivalent. There is a plane of symmetry in the NPLs which is normal to the [001] direction. However, the orientation of the Cd-Se bonds between the surface Cd atom and the neighboring Se atoms are rotated by  $90^\circ$  between the top and bottom planes. Hence, surface strain induced could easily deform these NPLs. For example, if the oleic acid at the surface adopt a particular orientation with respect to the CdSe crystal lattice (and hence the surface Cd-Se bonds), this will deform the surface bonds.

This deformation will propagate into the thin crystal and could yield to various twisting/bending phenomena. The precise deformation direction and scale will depend on the orientation of the ligand lattice and the extent to which the ligand-metal affect the other atoms in the NPLs.

Surface stress induced deformation of nanocrystals has already been held responsible for the emergence of dipoles in semi-conducting nanocrystals as described in the introduction chapter of this thesis. Previous studies have also reported variations of lattice parameters and size dependent distortion caused by surface effects. For example, lattice expansion in copper nanocrystals was rationalized using a surface pressure model [155]. In this case, the temperature dependence of gas adsorption at the surface of the nanoparticles was found to explain the expansion of the lattice in a quantitative fashion. In CdSe wurtzite colloidal nanocrystals, EXAFS and X-ray diffraction experiments showed variations of the lattice parameters as a function of size. These results were explained by surface stress caused by the adsorbed ligands [156]. In these cases, the nanoparticles are spherical and surface stress induces compression or elongation of the lattice. Here, a 2D material with high anisotropy is concerned and it is likely that surface stress will convert into elastic deformation of the material. In free-standing graphene, thermal fluctuations induce a roughening of the surface with out-of-plane deviations which can reach 1 nm [157]. In our case, the observed deformations are much more important and our material is five times thicker than graphene. This suggests that the energy scale at play is significantly larger but a more reliable order of magnitude estimation would necessitate further modeling efforts.

We could also relate the twisting deformation to the ligand surface phase transition already mentioned in the context of colloidal stability[79, 80]. Since twisting occurs upon addition of oleic acid, one could argue that it is related to a phase transition occurring at the surface of the particle. The temperature at which the phase transition happens has been shown to increase with surface coverage. It is thus possible that, at constant (ambient) temperature an ordering transition occurs when increasing surface ligand concentration. Upon ordering in a preferential direction with respect to the crystal lattice, the ligand would have a much more cumulative effect on the surface stress than in a disorganized state where the random orientations would cancel out. The surface phase transition also induces a strong short range attraction which would explain the precipitation observed jointly with the twisting.

We now discuss the twisting observed in the NPLs threads which could have several physical origins. We had first thought that a dipolar moment having an in-plane component tilted with respect to the edges added to a component parallel to the transverse direction would yield such an helical structure. The idea was that, in order to minimize the dipolar interaction energy, the in-plane dipole would align in an ferromagnetic fashion and hence lead to a tilt between adjacent NPLs. In order to check this hypothesis, H.H. Wensik conducted calculations in order to find ground-states for such a system of  $N$  spins interacting with a dipolar interaction. To do so, he wrote the total poten-

tial energy of  $N$  stacks on a lattice and found the ground states corresponding to this energy using a Monte-Carlo scheme <sup>1</sup>. In none of the ground states, an helical configuration with a mesoscopic pitch is found. However, such configurations are observed when one takes into account a pair interaction between NPLs composed of a dipolar term favoring untwisted aligned spins added to a screened electrostatic repulsion. Both interaction potentials are long ranged but with dissimilar spatial variations. This leads to helical ground states with pitches ranging from 10 to 100 NPLs, i.e. the same order of magnitude as our experimental findings. In this hypothesis, adding oleic acid would play on the electrostatic potential by reducing the charges at the surface of the NPLs. Finally, we could argue that the twisting of the threads comes from the twisting of the individual NPLs also occurring upon addition of oleic acid. In this hypothesis, NPLs in a thread could be “locked” in their flat configuration by their neighbors and the twisting of the threads would be a mean to relax elastic energy. Definitely choosing between these different hypothesis will necessitate further experiments and simulations.

## 6.5 Conclusion

We have shown that adding ligand gradually to a drying board-like NPLs dispersion leads to twisted threads with a pitch of around 400 nm. The length of the threads can be controlled by the total amount of oleic acid but the pitch is, for now, difficult to tune. We have also shown that individual nanoplatelets twist under the effect of oleic addition. These surprising results question the influence of ligand induced surface strain on the bending of nanometer objects, a topic which has received scarce attention yet.

---

<sup>1</sup>Personnal communication from R. Wensik



# Bibliography

1. Abécassis, B. Three-Dimensional Self Assembly of Semiconducting Colloidal Nanocrystals: From Fundamental Forces to Collective Optical Properties. *ChemPhysChem* **17**, 618–631 (2016).
2. Jana, S. *et al.* Stacking and Colloidal Stability of CdSe Nanoplatelets. *Langmuir* **31**, 10532–10539 (2015).
3. Abécassis, B., Tessier, M. D., Davidson, P. & Dubertret, B. Self-Assembly of CdSe Nanoplatelets into Giant Micrometer-Scale Needles Emitting Polarized Light. *Nano Lett.* **14**, 710–715 (2014).
4. Beaudoin, E., Abecassis, B., Constantin, D., Degrouard, J. & Davidson, P. Strain-controlled fluorescence polarization in a CdSe nanoplatelet–block copolymer composite. *Chem. Commun.* **51**, 4051–4054 (2015).
5. Yin, Y. & Alivisatos, a. P. Colloidal nanocrystal synthesis and the organic-inorganic interface. *Nature* **437**, 664–70 (2005).
6. Murray, C. B., Noms, D. J. & Bawendi, M. G. Synthesis and Characterization of Nearly Monodisperse CdE (E = S, Se, Te) Semiconductor Nanocrystallites. *J. Am. Chem. Soc.* **115**, 8706–8715 (1993).
7. Fox, M. *Optical Properties of Solids* 2 edition. 416 pp. (Oxford University Press, Oxford ; New York, 2010).
8. Lhuillier, E. *et al.* Two-Dimensional Colloidal Metal Chalcogenides Semiconductors: Synthesis, Spectroscopy, and Applications. *Acc. Chem. Res.* **48**, 22–30 (2015).
9. Wang, F. *et al.* Two-Dimensional Semiconductor Nanocrystals: Properties, Templated Formation, and Magic-Size Nanocluster Intermediates. *Acc. Chem. Res.* **48**, 13–21 (2015).
10. Bouet, C. *et al.* Flat Colloidal Semiconductor Nanoplatelets. *Chem. Mater.* **25**, 1262–1271 (2013).
11. Ithurria, S. & Dubertret, B. Quasi 2D colloidal CdSe platelets with thicknesses controlled at the atomic level. *J. Am. Chem. Soc.* **130**, 16504–5 (2008).
12. Ithurria, S. *et al.* Colloidal nanoplatelets with two-dimensional electronic structure. *Nat Mater* **10**, 936–41 (2011).



13. Joo, J., Son, J. S., Kwon, S. G., Yu, J. H. & Hyeon, T. Low-Temperature Solution-Phase Synthesis of Quantum Well Structured CdSe Nanoribbons. *J. Am. Chem. Soc.* **128**, 5632–5633 (2006).
14. Son, J. S. *et al.* Dimension-Controlled Synthesis of CdS Nanocrystals: From 0D Quantum Dots to 2D Nanoplates. *Small* **8**, 2394–2402 (2012).
15. Son, J. S. *et al.* Large-Scale Soft Colloidal Template Synthesis of 1.4 nm Thick CdSe Nanosheets. *Angew. Chem. Int. Ed.* **48**, 6861–6864 (2009).
16. Liu, Y.-H., Wang, F., Wang, Y., Gibbons, P. C. & Buhro, W. E. Lamellar Assembly of Cadmium Selenide Nanoclusters into Quantum Belts. *J. Am. Chem. Soc.* **133**, 17005–17013 (2011).
17. Green, M. L. H. A new approach to the formal classification of covalent compounds of the elements. *Journal of Organometallic Chemistry* **500**, 127–148 (1995).
18. Anderson, N. C., Hendricks, M. P., Choi, J. J. & Owen, J. S. Ligand Exchange and the Stoichiometry of Metal Chalcogenide Nanocrystals: Spectroscopic Observation of Facile Metal-Carboxylate Displacement and Binding. *J. Am. Chem. Soc.* **135**, 18536–18548 (2013).
19. Owen, J. The coordination chemistry of nanocrystal surfaces. *Science* **347**, 615–616 (2015).
20. Bouet, C. *et al.* Two-Dimensional Growth of CdSe Nanocrystals, from Nanoplatelets to Nanosheets. *Chem. Mater.* **25**, 639–645 (2013).
21. Tessier, M. D., Javaux, C., Maksimovic, I., Loriette, V. & Dubertret, B. Spectroscopy of Single CdSe Nanoplatelets. *ACS Nano* **6**, 6751–6758 (2012).
22. Achtstein, A. W. *et al.* Electronic Structure and Exciton-Phonon Interaction in Two-Dimensional Colloidal CdSe Nanosheets. *Nano Lett.* **12**, 3151–3157 (2012).
23. Pelton, M., Ithurria, S., Schaller, R. D., Dolzhenkov, D. S. & Talapin, D. V. Carrier Cooling in Colloidal Quantum Wells. *Nano Lett.* **12**, 6158–6163 (2012).
24. Biadala, L. *et al.* Recombination Dynamics of Band Edge Excitons in Quasi-Two-Dimensional CdSe Nanoplatelets. *Nano Lett.* **14**, 1134–1139 (2014).
25. Lehn, J.-M. Toward Self-Organization and Complex Matter. *Science* **295**, 2400–2403 (2002).
26. Whitesides, G. M. & Grzybowski, B. Self-Assembly at All Scales. *Science* **295**, 2418–2421 (2002).
27. Glotzer, S. C. & Solomon, M. J. Anisotropy of building blocks and their assembly into complex structures. *Nat. Mater.* **6**, 557–562 (2007).
28. Shevchenko, E. V. & Talapin, D. V. in *Semiconductor Nanocrystal Quantum Dots* (ed Rogach, D. A. L.) 119–169 (Springer Vienna, 2008).
29. Min, Y., Akbulut, M., Kristiansen, K., Golan, Y. & Israelachvili, J. The role of interparticle and external forces in nanoparticle assembly. *Nat. Mater.* **7**, 527–538 (2008).
30. Zhang, H., Edwards, E. W., Wang, D. & Möhwald, H. Directing the self-assembly of nanocrystals beyond colloidal crystallization. *Phys. Chem. Chem. Phys.* **8**, 3288–3299 (2006).
31. Vanmaekelbergh, D. Self-assembly of colloidal nanocrystals as route to novel classes of nanostructured materials. *Nano Today* **6**, 419–437 (2011).

32. Gao, Y. & Tang, Z. Design and Application of Inorganic Nanoparticle Superstructures: Current Status and Future challenges. *Small* **7**, 2133–2146 (2011).
33. Wang, L., Xu, L., Kuang, H., Xu, C. & Kotov, N. A. Dynamic Nanoparticle Assemblies. *Acc. Chem. Res.* **45**, 1916–1926 (2012).
34. Zhang, S.-Y., Regulacio, M. D. & Han, M.-Y. Self-assembly of colloidal one-dimensional nanocrystals. *Chem. Soc. Rev.* **43**, 2301–2323 (2014).
35. Kim, J. K., Yang, S. Y., Lee, Y. & Kim, Y. Functional nanomaterials based on block copolymer self-assembly. *Prog. Polym. Sci.* **35**, 1325–1349 (2010).
36. Taheri, S. M., Fischer, S. & Foerster, S. Routes to Nanoparticle-Polymer Superlattices. *Polymers* **3**, 662–673 (2011).
37. Nozik, A. J. *et al.* Semiconductor Quantum Dots and Quantum Dot Arrays and Applications of Multiple Exciton Generation to Third-Generation Photovoltaic Solar Cells. *Chem. Rev.* **110**, 6873–6890 (2010).
38. Zhang, G. *et al.* Semiconductor nanostructure-based photovoltaic solar cells. *Nanoscale* **3**, 2430–2443 (2011).
39. Quan, Z., Valentin-Bromberg, L., Loc, W. S. & Fang, J. Self-Assembly of Lead Chalcogenide Nanocrystals. *Chem.-Asian J.* **6**, 1126–1136 (2011).
40. Kim, J.-Y. & Kotov, N. A. Charge Transport Dilemma of Solution-Processed Nanomaterials. *Chem. Mater.* **26**, 134–152 (2014).
41. Bishop, K. J. M., Wilmer, C. E., Soh, S. & Grzybowski, B. A. Nanoscale Forces and Their Uses in Self-Assembly. *Small* **5**, 1600–1630 (2009).
42. Batista, C. A. S., Larson, R. G. & Kotov, N. A. Nonadditivity of nanoparticle interactions. *Science* **350**, 1242477 (2015).
43. Schmidt, M. E., Blanton, S. A., Hines, M. A. & Guyot-Sionnest, P. Polar CdSe nanocrystals: Implications for electronic structure. *J. Chem. Phys.* **106**, 5254–5259 (1997).
44. Blanton, S. A., Leheny, R. L., Hines, M. A. & Guyot-Sionnest, P. Dielectric Dispersion Measurements of CdSe Nanocrystal Colloids: Observation of a Permanent Dipole Moment. *Phys. Rev. Lett.* **79**, 865–868 (1997).
45. Shim, M. & Guyot-Sionnest, P. Permanent dipole moment and charges in colloidal semiconductor quantum dots. *J. Chem. Phys.* **111**, 6955–6964 (1999).
46. Huong, N. Q. & Birman, J. L. Origin of polarization in polar nanocrystals. *J. Chem. Phys.* **108**, 1769–1772 (1998).
47. Shanbhag, S. & Kotov, N. A. On the Origin of a Permanent Dipole Moment in Nanocrystals with a Cubic Crystal Lattice: Effects of Truncation, Stabilizers, and Medium for CdS Tetrahedral Homologues. *J. Phys. Chem. B* **110**, 12211–12217 (2006).
48. Li, L.-s. & Alivisatos, A. P. Origin and Scaling of the Permanent Dipole Moment in CdSe Nanorods. *Phys. Rev. Lett.* **90**, 097402 (2003).
49. Nann, T. & Schneider, J. Origin of permanent electric dipole moments in wurtzite nanocrystals. *Chem. Phys. Lett.* **384**, 150–152 (2004).

50. Cho, K.-S., Talapin, D. V., Gaschler, W. & Murray, C. B. Designing PbSe Nanowires and Nanorings through Oriented Attachment of Nanoparticles. *J. Am. Chem. Soc.* **127**, 7140–7147 (2005).
51. Talapin, D. V., Shevchenko, E. V., Murray, C. B., Titov, A. V. & Král, P. Dipole-Dipole Interactions in Nanoparticle Superlattices. *Nano Lett.* **7**, 1213–1219 (2007).
52. Israelachvili, J. N. *Intermolecular and Surface Forces* (Academic Press, 2010).
53. Rabani, E. An interatomic pair potential for cadmium selenide. *J. Chem. Phys.* **116**, 258–262 (2002).
54. Baskin, A., Lo, W.-Y. & Kral, P. Clusters and Lattices of Particles Stabilized by Dipolar Coupling. *Acs Nano* **6**, 6083–6090 (2012).
55. Parsegian, V. A. *Van der Waals Forces: A Handbook for Biologists, Chemists, Engineers, and Physicists* (Cambridge University Press, New York, 2005).
56. Bergström, L. Hamaker constants of inorganic materials. *Adv. Colloid Interface Sci.* **70**, 125–169 (1997).
57. Striolo, A. *et al.* Molecular Weight, Osmotic Second Virial Coefficient, and Extinction Coefficient of Colloidal CdSe Nanocrystals. *J. Phys. Chem. B* **106**, 5500–5505 (2002).
58. Walker, D. A., Kowalczyk, B., de la Cruz, M. O. & Grzybowski, B. A. Electrostatics at the nanoscale. *Nanoscale* **3**, 1316–1344 (2011).
59. Morrison, I. D. Electrical charges in nonaqueous media. *Colloids Surf. Physicochem. Eng. Asp.* **71**, 1–37 (1993).
60. Lyklema, J. Principles of interactions in non-aqueous electrolyte solutions. *Curr. Opin. Colloid Interface Sci.* **18**, 116–128 (2013).
61. Hsu, M. F., Dufresne, E. R. & Weitz, D. A. Charge Stabilization in Nonpolar Solvents. *Langmuir* **21**, 4881–4887 (2005).
62. Shilov, V. N., Borkovskaja, Y. B. & Dukhin, A. S. Electroacoustic theory for concentrated colloids with overlapped DLs at arbitrary  $\kappa a$ : I. Application to nanocolloids and nonaqueous colloids. *J. Colloid Interface Sci.* **277**, 347–358 (2004).
63. Doane, T. L., Chuang, C.-H., Hill, R. J. & Burda, C. Nanoparticle  $\zeta$  - Potentials. *Acc. Chem. Res.* **45**, 317–326 (2012).
64. Bhattacharjee, S. & Elimelech, M. Surface Element Integration: A Novel Technique for Evaluation of DLVO Interaction between a Particle and a Flat Plate. *Journal of Colloid and Interface Science* **193**, 273–285 (1997).
65. Owen, J. S., Park, J., Trudeau, P.-E. & Alivisatos, a. P. Reaction chemistry and ligand exchange at cadmium-selenide nanocrystal surfaces. *J. Am. Chem. Soc.* **130**, 12279–81 (2008).
66. Fritzinger, B., Capek, R. K., Lambert, K., Martins, J. C. & Hens, Z. Utilizing Self-Exchange To Address the Binding of Carboxylic Acid Ligands to CdSe Quantum Dots. *J. Am. Chem. Soc.* **132**, 10195–10201 (2010).
67. Morris-Cohen, A. J., Donakowski, M. D., Knowles, K. E. & Weiss, E. A. The Effect of a Common Purification Procedure on the Chemical Composition of the Surfaces of CdSe Quantum Dots Synthesized with Trioctylphosphine Oxide. *J. Phys. Chem. C* **114**, 897–906 (2010).

68. Moreels, I., Fritzing, B., Martins, J. C. & Hens, Z. Surface Chemistry of Colloidal PbSe Nanocrystals. *J. Am. Chem. Soc.* **130**, 15081–15086 (2008).
69. Moreels, I. *et al.* Size-Tunable, Bright, and Stable PbS Quantum Dots: A Surface Chemistry Study. *ACS Nano* **5**, 2004–2012 (2011).
70. Shevchenko, E. V., Talapin, D. V., Kotov, N. A., O'Brien, S. & Murray, C. B. Structural diversity in binary nanoparticle superlattices. *Nature* **439**, 55–59 (2006).
71. Hesselink, F. T., Vrij, A. & Overbeek, J. T. G. Theory of the stabilization of dispersions by adsorbed macromolecules. II. Interaction between two flat particles. *J. Phys. Chem.* **75**, 2094–2103 (1971).
72. Tadros, T. F. Steric Stabilisation and Flocculation by Polymers. *Polym. J.* **23**, 683–696 (1991).
73. Derjaguin, B. V. Untersuchungen über die Reibung und Adhäsion, IV. *Colloid Polym. Sci.* **69**, 155–164 (1934).
74. Kim, J. U. & Matsen, M. W. Interaction between Polymer-Grafted Particles. *Macromolecules* **41**, 4435–4443 (2008).
75. Roan, J.-R. Attraction between Nanoparticles Induced by End-Grafted Homopolymers in Good Solvent. *Phys. Rev. Lett.* **86**, 1027–1030 (2001).
76. Matsen, M. W. Comment on Attraction between Nanoparticles Induced by End-Grafted Homopolymers in Good Solvent. *Phys. Rev. Lett.* **95**, 069801 (2005).
77. Rabani, E. & Egorov, S. A. Interactions between passivated nanoparticles in solutions: Beyond the continuum model. *J. Chem. Phys.* **115**, 3437–3440 (2001).
78. Rabani, E. & Egorov, S. A. Solvophobic and Solvophilic Effects on the Potential of Mean Force between Two Nanoparticles in Binary Mixtures. *Nano Lett.* **2**, 69–72 (2002).
79. Widmer-Cooper, A. & Geissler, P. Orientational Ordering of Passivating Ligands on CdS Nanorods in Solution Generates Strong Rod–Rod Interactions. *Nano Lett.* **14**, 57–65 (2014).
80. Widmer-Cooper, A. & Geissler, P. L. Ligand-Mediated Interactions between Nanoscale Surfaces Depend Sensitively and Nonlinearly on Temperature, Facet Dimensions, and Ligand Coverage. *ACS Nano* (2016).
81. Yang, Y., Qin, H. & Peng, X. Intramolecular Entropy and Size-Dependent Solution Properties of Nanocrystal–Ligands Complexes. *Nano Lett.* (2016).
82. Yang, Y. *et al.* Entropic Ligands for Nanocrystals: From Unexpected Solution Properties to Outstanding Processability. *Nano Lett.* (2016).
83. Jones, M. R., Macfarlane, R. J., Prigodich, A. E., Patel, P. C. & Mirkin, C. A. Nanoparticle Shape Anisotropy Dictates the Collective Behavior of Surface-Bound Ligands. *J. Am. Chem. Soc.* **133**, 18865–18869 (2011).
84. Glotzer, S. C. Nanotechnology: shape matters. *Nature* **481**, 450–452 (2012).
85. Lekkerkerker, H. N. W. & Tuinier, R. *Colloids and the Depletion Interaction* (Springer Science & Business Media, 2011).
86. Mason, T. G. Osmotically driven shape-dependent colloidal separations. *Phys. Rev. E* **66**, 060402 (2002).

87. Park, K., Koerner, H. & Vaia, R. A. Depletion-Induced Shape and Size Selection of Gold Nanoparticles. *Nano Lett.* **10**, 1433–1439 (2010).
88. Zhang, J., Lang, P. R., Meyer, M. & Dhont, J. K. G. Synthesis and Self-Assembly of Squarelike PbCrO<sub>4</sub> Nanoplatelets via Micelle-Mediated Depletion Attraction. *Langmuir* **29**, 4679–4687 (2013).
89. Baranov, D. *et al.* Assembly of Colloidal Semiconductor Nanorods in Solution by Depletion Attraction. *Nano Lett.* **10**, 743–749 (2010).
90. Bloomquist, C. R. & Shutt, R. S. Fine Particle Suspensions in Organic Liquids. *Ind. Eng. Chem.* **32**, 827–831 (1940).
91. Schatzberg, P. Solubilities of water in several normal alkanes from C<sub>7</sub> to C<sub>16</sub>. *J. Phys. Chem.* **67**, 776–779 (1963).
92. Li, L.-s., Marjanska, M., Park, G. H. J., Pines, A. & Alivisatos, A. P. Isotropic-liquid crystalline phase diagram of a CdSe nanorod solution. *J. Chem. Phys.* **120**, 1149 (2004).
93. Miszta, K. *et al.* Hierarchical self-assembly of suspended branched colloidal nanocrystals into superlattice structures. *Nat. Mater.* **10**, 872–876 (2011).
94. Roberts, G. S., Sanchez, R., Kemp, R., Wood, T. & Bartlett, P. Electrostatic Charging of Nonpolar Colloids by Reverse Micelles. *Langmuir* **24**, 6530–6541 (2008).
95. Gacek, M., Bergsman, D., Michor, E. & Berg, J. C. Effects of Trace Water on Charging of Silica Particles Dispersed in a Nonpolar Medium. *Langmuir* **28**, 11633–11638 (2012).
96. Godfrey Alig, A., Akbulut, M., Golan, Y. & Israelachvili, J. Forces between Surfactant-Coated ZnS Nanoparticles in Dodecane: Effect of Water. *Adv. Funct. Mater.* **16**, 2127–2134 (2006).
97. Min, Y., Akbulut, M., Prud'homme, R. K., Golan, Y. & Israelachvili, J. Frictional Properties of Surfactant-Coated Rod-Shaped Nanoparticles in Dry and Humid Dodecane †. *J. Phys. Chem. B* **112**, 14395–14401 (2008).
98. Guzelturk, B., Erdem, O., Olutas, M., Kelestemur, Y. & Demir, H. V. Stacking in Colloidal Nanoplatelets: Tuning Excitonic Properties. *ACS Nano* **8**, 12524–12533 (2014).
99. Wang, S. *et al.* Collective fluorescence enhancement in nanoparticle clusters. *Nat. Commun.* **2**, 364 (2011).
100. Nirmal, M. *et al.* Fluorescence intermittency in single cadmium selenide nanocrystals. *Nature* **383**, 802–804 (1996).
101. Shimizu, K. T. *et al.* Blinking statistics in single semiconductor nanocrystal quantum dots. *Phys. Rev. B* **63**, 205316 (2001).
102. Cichos, F., von Borczyskowski, C. & Orrit, M. Power-law intermittency of single emitters. *Curr. Opin. Colloid Interface Sci.* **12**, 272–284 (2007).
103. Frantsuzov, P., Kuno, M., Jankó, B. & Marcus, R. A. Universal emission intermittency in quantum dots, nanorods and nanowires. *Nat Phys* **4**, 519–522 (2008).
104. Peterson, J. J. & Nesbitt, D. J. Modified Power Law Behavior in Quantum Dot Blinking: A Novel Role for Biexcitons and Auger Ionization. *Nano Lett.* **9**, 338–345 (2009).
105. Yu, M. & Van Orden, A. Enhanced Fluorescence Intermittency of CdSe-ZnS Quantum-Dot Clusters. *Phys. Rev. Lett.* **97**, 237402 (2006).

106. Whitcomb, K. J., Ryan, D. P., Gelfand, M. P. & Van Orden, A. Blinking Statistics of Small Clusters of Semiconductor Nanocrystals. *J. Phys. Chem. C* **117**, 25761–25768 (2013).
107. Förster, T. Zwischenmolekulare Energiewanderung und Fluoreszenz. *Ann. Phys.* **437**, 55–75 (1948).
108. Guzelturk, B. *et al.* Nonradiative energy transfer in colloidal CdSe nanoplatelet films. *Nanoscale* **7**, 2545–2551 (2015).
109. Rowland, C. E. *et al.* Picosecond energy transfer and multiexciton transfer outpaces Auger recombination in binary CdSe nanoplatelet solids. *Nat. Mater.* **14**, 484–489 (2015).
110. Moreels, I. Colloidal nanoplatelets: Energy transfer is speeded up in 2D. *Nat. Mater.* **14**, 464–465 (2015).
111. Overbeek, J. T. G. in *Colloid Science* (ed Kruyt, H. R.) 278–301 (Elsevier: New York, 1951).
112. Smilgies, D.-M. Scherrer grain-size analysis adapted to grazing-incidence scattering with area detectors. *J. Appl. Crystallogr.* **42**, 1030–1034 (2009).
113. Guinier, A. & Fournet, G. *Small-angle scattering of X-rays* 288 pp. (Wiley, 1955).
114. Landau, L. D. & Lifshitz, E. M. *Statistical Physics, Third Edition, Part 1: Volume 5* 3 edition (Butterworth-Heinemann, Amsterdam u.a, 1980).
115. Tanford, C. Micelle shape and size. *J. Phys. Chem.* **76**, 3020–3024 (1972).
116. Hassinen, A. *et al.* Short-Chain Alcohols Strip X-Type Ligands and Quench the Luminescence of PbSe and CdSe Quantum Dots, Acetonitrile Does Not. *J. Am. Chem. Soc.* **134**, 20705–20712 (2012).
117. Morrison, I. D. & Ross, S. *Colloidal Dispersions: Suspensions, Emulsions, and Foams* (Wiley, 2002).
118. Buining, P. A., Veldhuizen, Y. S. J., Pathmamanoharan, C. & Lekkerkerker, H. N. W. Preparation of a non-aqueous dispersion of sterically stabilized boehmite rods. *Colloids Surf* **64**, 47–55 (1992).
119. Van Bruggen, M. P. B., van der Kooij, F. M. & Lekkerkerker, H. N. W. Liquid crystal phase transitions in dispersions of rod-like colloidal particles. *J. Phys.: Condens. Matter* **8**, 9451 (1996).
120. Ehlert, S. *et al.* Polymer Ligand Exchange to Control Stabilization and Compatibilization of Nanocrystals. *ACS Nano* **8**, 6114–6122 (2014).
121. Chevigny, C. *et al.* Controlled grafting of polystyrene on silica nanoparticles using NMP: a new route without free initiator to tune the grafted chain length. *Polym. Chem.* **2**, 567–571 (2011).
122. Tessier, M. D. *et al.* Phonon Line Emission Revealed by Self-Assembly of Colloidal Nanoplatelets. *ACS Nano* **7**, 3332–3340 (2013).
123. Hu, J. *et al.* Linearly polarized emission from colloidal semiconductor quantum rods. *Science* **292**, 2060–2063 (2001).
124. Wang, T., LaMontagne, D., Lynch, J., Zhuang, J. & Cao, Y. C. Colloidal superparticles from nanoparticle assembly. *Chem. Soc. Rev.* **42**, 2804 (2013).

125. Zang, L., Che, Y. & Moore, J. S. One-Dimensional Self-Assembly of Planar  $\pi$ -Conjugated Molecules: Adaptable Building Blocks for Organic Nanodevices. *Acc. Chem. Res.* **41**, 1596–1608 (2008).
126. Che, Y., Datar, A., Balakrishnan, K. & Zang, L. Ultralong Nanobelts Self-Assembled from an Asymmetric Perylene Tetracarboxylic Diimide. *J. Am. Chem. Soc.* **129**, 7234–7235 (2007).
127. Datar, A. *et al.* Linearly Polarized Emission of an Organic Semiconductor Nanobelt. *J. Phys. Chem. B.* **110**, 12327–12332 (2006).
128. Chen, Z., Nadal, B., Mahler, B., Aubin, H. & Dubertret, B. Quasi-2D Colloidal Semiconductor Nanoplatelets for Narrow Electroluminescence. *Adv. Funct. Mater.* **24**, 295–302 (2014).
129. Huynh, W. U., Dittmer, J. J. & Alivisatos, A. P. Hybrid nanorod-polymer solar cells. *Science* **295**, 2425–2427 (2002).
130. Perez-Juste, J., Pastoriza-Santos, I., Liz-Marzan, L. M. & Mulvaney, P. Gold nanorods: Synthesis, characterization and applications. *Coord. Chem. Rev.* **249**, 1870–1901 (2005).
131. Balazs, A. C., Emrick, T. & Russell, T. P. Nanoparticle polymer composites: Where two small worlds meet. *Science* **314**, 1107–1110 (2006).
132. Glogowski, E., Tangirala, R., Russell, T. P. & Emrick, T. Functionalization of nanoparticles for dispersion in polymers and assembly in fluids. *J. Polym. Sci. Part -Polym. Chem.* **44**, 5076–5086 (2006).
133. Lee, J., Sundar, V. C., Heine, J. R., Bawendi, M. G. & Jensen, K. F. Full color emission from II-VI semiconductor quantum dot-polymer composites. *Adv. Mater.* **12**, 1102–+ (2000).
134. Fischer, S., Salcher, A., Kornowski, A., Weller, H. & Forster, S. Completely Miscible Nanocomposites. *Angew. Chem.-Int. Ed.* **50**, 7811–7814 (2011).
135. Van der Zande, B. M. I., Pages, L., Hikmet, R. A. M. & van Blaaderen, A. Optical properties of aligned rod-shaped gold particles dispersed in poly(vinyl alcohol) films. *J. Phys. Chem. B* **103**, 5761–5767 (1999).
136. Gupta, S., Zhang, Q., Emrick, T. & Russell, T. P. Self-Corralling Nanorods under an Applied Electric Field. *Nano Lett.* **6**, 2066–2069 (2006).
137. Hore, M. J. A. & Composto, R. J. Functional Polymer Nanocomposites Enhanced by Nanorods. *Macromolecules* **47**, 875–887 (2014).
138. Kalyuzhny, G. & Murray, R. W. Ligand effects on optical properties of CdSe nanocrystals. *J. Phys. Chem. B* **109**, 7012–7021 (2005).
139. Cordero, S. R., Carson, P. J., Estabrook, R. A., Strouse, G. F. & Buratto, S. K. Photo-activated luminescence of CdSe quantum dot monolayers. *J. Phys. Chem. B* **104**, 12137–12142 (2000).
140. Hashimoto, T. ; *et al.* *Adv Chem Ser* **176**, 257–275 (1979).
141. Huy, T. A., Adhikari, R. & Michler, G. H. Deformation behavior of styrene-block-butadiene-block-styrene triblock copolymers having different morphologies. *Polymer* **44**, 1247–1257 (2003).



142. Paineau, E. *et al.* In-situ SAXS Study of Aqueous Clay Suspensions Submitted to Alternating Current Electric Fields. *J. Phys. Chem. B* **116**, 13516–13524 (2012).
143. Lakowicz, J. R. *Principles of fluorescence spectroscopy* (Springer, Baltimore, USA, 2006).
144. She, C. *et al.* Low-Threshold Stimulated Emission Using Colloidal Quantum Wells. *Nano Lett.* **14**, 2772–2777 (2014).
145. DeVries, G. A. *et al.* Divalent metal nanoparticles. *Science* **315**, 358–361 (2007).
146. Wang, F., Richards, V. N., Shields, S. P. & Buhro, W. E. Kinetics and Mechanisms of Aggregative Nanocrystal Growth. *Chem. Mater.* **26**, 5–21 (2014).
147. Nie, Z. *et al.* Self-assembly of metal–polymer analogues of amphiphilic triblock copolymers. *Nat. Mater.* **6**, 609–614 (2007).
148. Caswell, K., Wilson, J. N., Bunz, U. H. & Murphy, C. J. Preferential end-to-end assembly of gold nanorods by biotin-streptavidin connectors. *J. Am. Chem. Soc.* **125**, 13914–13915 (2003).
149. Shanbhag, S., Tang, Z. & Kotov, N. A. Self-organization of Te nanorods into V-shaped assemblies: a Brownian dynamics study and experimental insights. *ACS nano* **1**, 126–132 (2007).
150. Khatory, A. *et al.* Entangled versus multiconnected network of wormlike micelles. *Langmuir* **9**, 933–939 (1993).
151. Won, Y.-Y., Davis, H. T. & Bates, F. S. Giant wormlike rubber micelles. *Science* **283**, 960–963 (1999).
152. Greer, S. C. Reversible polymerizations and aggregations. *Annu. Rev. Phys. Chem.* **53**, 173–200 (2002).
153. Wang, X. *et al.* Cylindrical Block Copolymer Micelles and Co-Micelles of Controlled Length and Architecture. *Science* **317**, 644–647 (2007).
154. Ithurria, S. *Synthèses et caractérisations de nanoparticules de semiconducteurs II-VI de géométries contrôlées* PhD thesis (Université Pierre et Marie Curie - Paris VI, 2010).
155. Champion, Y., Bernard, F., Millot, N. & Perriat, P. Surface adsorption effects on the lattice expansion of copper nanocrystals. *Applied Physics Letters* **86**, 231914 (2005).
156. Wu, P.-J., Stetsko, Y. P., Tsuei, K.-D., Dronyak, R. & Liang, K. S. Size dependence of tetrahedral bond lengths in CdSe nanocrystals. *Applied Physics Letters* **90**, 161911 (2007).
157. Meyer, J. C. *et al.* The structure of suspended graphene sheets. *Nature* **446**, 60–63 (2007).
158. Yang, Y. A., Wu, H., Williams, K. R. & Cao, Y. C. Synthesis of CdSe and CdTe Nanocrystals without Precursor Injection. *Angew. Chem. Int. Ed.* **44**, 6712–6715 (2005).
159. Imperor-Clerc, M. & Davidson, P. An X-ray scattering study of flow-aligned samples of a lyotropic liquid-crystalline hexagonal phase. *European Physical Journal B* **9**, 93–104 (1999).
160. Cassette, E. *et al.* Colloidal CdSe/CdS Dot-in-Plate Nanocrystals with 2D-Polarized Emission. *ACS Nano* **6**, 6741–6750 (2012).



# Experimental techniques

## A.1 Syntheses

### A.1.1 Nanoplatelets

The cadmium myristate salt was synthesized as described in detail elsewhere [158]. For the 4ML nanoplatelet synthesis : 0.234 g of cadmium myristate and 0.024 g of selenium powder were mixed with 30 mL of octadecene in a three-neck round-bottom flask equipped with a condenser, a septum and a temperature controller. Under magnetic agitation, the mixture was then degassed under vacuum for 30 minutes and heated from ambient temperature to 240°C. When the temperature reached 200°C (after about 6 min 30 s) 0.160 g of cadmium acetate (in powder) was added to the solution after having withdrawn the septum. When the salt is poured in the solution, the solution's color is yellow and starts to turn red. After 12 min at 240°C, heating was stopped and an excess of carboxylic acid was added. At this stage, the solution contained, as shown by UV-vis absorption, three populations of nanoparticles: platelets emitting at 460 nm, platelets emitting at 510 nm and quantum dots. To isolate platelets emitting at 510 nm, a series of selective precipitation/centrifugation steps was performed. The raw product was separated in two centrifuge tubes and 20 mL of ethanol was added to each of the tubes. After centrifugation for 10 min at 5000 tr/min, the supernatant contained quantum dots while the precipitate only contained platelets. The latter was re-dispersed in hexane and this solution was centrifuged at 3000 tr/min for 10 minutes. The supernatant only contained platelets emitting at 510 nm while the larger platelets emitting at 460 nm precipitated. At last, ethanol was added to the solution to make the platelets precipitate, the supernatant was discarded and the precipitate was redispersed in hexane. Finally, the platelets were precipitated and dried. For the 5ML NPL synthesis, the same protocol was applied by replacing cadmium myristate by cadmium oleate.

### A.1.2 Polystyrene synthesis

BlocBuilder MA and styrene were mixed together in a round-bottomed flask. The flask was equipped with a condenser. After 15 to 30 minutes of degassing by nitrogen bub-

bling, the temperature was raised to 120 °C and the polymerization was performed under inert atmosphere and magnetic stirring for 90 min. The polymer was isolated by precipitation in cold ethanol, recovered by filtration and dried under vacuum. The polystyrene (PS) was prepared using a Initiator/Styrene molar ratio of 1/19. At this stage, the obtained polymer is composed of a polystyrene chain, a carboxylic acid end and a nitroxide moiety. In order to eliminate the nitroxide, a thermo-labile group, end-capped polystyrene, the obtained polymer, was solubilized in tert-butylbenzene at about  $5 \cdot 10^{-2}$  M and introduced in a round-bottomed flask equipped with a condenser. Then, 5 equivalents of thiophenol with respect to the polymer were added to the solution. The temperature was raised to 130 °C for 4 hours. The carboxy-terminated polystyrene was isolated by precipitation in cold ethanol, recovered by filtration and dried under vacuum. The molar mass ( $M_n$ ) and dispersity ( $\mathcal{D}$ ) of the obtained PS were determined by size exclusion chromatography (SEC) using tetrahydrofuran as eluent. The  $M_n$  and  $\mathcal{D}$  values derived from calibration curve based on PS standards were  $1700 \text{ g}\cdot\text{mol}^{-1}$  and 1.10.

### A.1.3 Polymer ligand exchange procedure

In a typical exchange 4 mg of CdSe nanoplatelets were dissolved in 5 mL of THF. To the nanocrystal solution, 0.25 g of polystyrene-COOH in 2 mL of THF was added. After the two solutions were completely mixed, the solution was sonicated 30 min at 50 °C and 10 mL of ethanol was added for quantitative precipitation. The precipitate was separated by centrifugation and the supernatant was discarded and the precipitate was dissolved in 5 mL of THF. This procedure was repeated twice. Subsequently, ethanol was added slowly until precipitation occurs. The supernatant was discarded and the precipitate was dissolved in 5 mL of THF for further measurement.

### A.1.4 Composite synthesis

SBS is a triblock copolymer commercially available from PolymerSource (QC, Canada) with a narrow polydispersity index (PDI) of 1.04 and almost equal molecular weights of PS ( $39.7 \text{ kg}\cdot\text{mol}^{-1}$ ) and PB ( $41.0 \text{ kg}\cdot\text{mol}^{-1}$ ). This molecular weight composition leads to a microphase separation with a lamellar morphology. Mixtures with different concentrations of CdSe were prepared by adding different volumes of nanoplatelet suspension in hexane to 30 mg SBS in 1 ml toluene. The CdSe concentration was checked by the UV-visible absorption of the mixtures. Composite films were then obtained by solvent-casting. Annealing was performed for 12 hours at 110 °C under argon atmosphere. Hybrid films with typical thickness of 100 nm and diameter of 10 mm were prepared. Good dispersions with nanoplatelet volume fractions ranging from 2 to 20% were obtained. In this work, we focus on the results obtained with the intermediate volume fraction of 10%.

### A.1.5 Self-assembly of superparticles

To obtain the superparticles, 500  $\mu\text{L}$  of the nanoplatelet dispersion was first diluted by adding 250  $\mu\text{L}$  of hexane. Afterwards, 250  $\mu\text{L}$  of ethanol was added to the previous

solution. The quantity of ethanol to be added to the colloidal solution varied from nanoplatelet synthesis batch to batch but the volume fraction in ethanol in the final solution was always comprised between 30 and 50 %.

## A.2 Small Angle X-ray Scattering

SAXS experiments were performed on different instruments. Most of the experiments were performed at the SWING beamline of the SOLEIL synchrotron (Saint-Aubin, France), measurements were carried out using a fixed energy of 12 keV and three sample to detector positions (0.85, 1.07 and 6.56 m). The typical accessible range of scattering vector modulus  $q$  was 0.02-10 nm<sup>-1</sup> ( $q = \frac{4\pi}{\lambda} \sin(\theta)$ ), where  $2\theta$  is the scattering angle and  $\lambda = 1.033 \text{ \AA}$  the wavelength). Scattering patterns were recorded on an AVIEX 170170 CCD camera formed by four detectors and radially averaged. Two complementary samples, corresponding to stacks of NPL coated with decanoic and heptanoic acid were investigated using a laboratory set-up composed of an X-ray generator with a Mo target and a MAR detector.

Another laboratory set-up was used in the case of the composite films. In this case, We used a laboratory SAXS setup equipped with a rotating copper anode generator (wavelength  $\lambda = 0.154 \text{ nm}$ ) and an Osmic Ni/C multilayered optics [159] The sample to detector distance was 1.07 m for experiments at small scattering vectors and 0.41 m for experiments at medium scattering vectors. The accessible range of scattering vector modulus  $q$  was  $0.09 < q < 1.3 \text{ nm}^{-1}$  in the first case and  $0.25 < q < 3.5 \text{ nm}^{-1}$  in the second. The scattered X-rays were detected by a Princeton CCD camera and exposure times typically ranged from 5 to 15 minutes. 2-dimensional images are presented as such, whereas 1- dimensional  $I(q)$  curves of the scattered intensity versus  $q$  were obtained by angular averaging of the scattering patterns. Using well-documented procedures [142], the platelet alignment, quantified by the nematic order parameter  $S$ , was derived from the dependence versus azimuthal angle of the scattered intensity at fixed  $q$  value in the SAXS patterns.

## A.3 Electron microscopy

TEM samples were prepared by depositing a drop of the nanoparticle dispersion on a carbon coated copper grid and letting it dry in air. Two different microscopes were used: A TOPCON electron microscope at a voltage of 100 kV or a JEOL 1400 (120 kV).

In the case of the polymer films, Cross-sectional TEM specimens of 50 nm thickness were cut in the composite films using a Leica EM UC6/FC6cryo-ultramicrotome at -100°C and a 35-degree Diatome diamond knife. Cryosections were collected on Quantifoil S7/2 grids coated by a continuous thin carbon film. The sections were stained by exposure to OsO<sub>4</sub> vapor for 15 min. The specimens were examined with a JEOL JEM 2011 TEM using a 200kV acceleration voltage. Images were acquired using a Gatan ultrascan CCD camera. OsO<sub>4</sub> reacts preferentially with the unsaturated carbon double

bond in the polybutadiene block, which is why the PB regions appear darker than the PS ones in bright-field TEM images. Moreover, due to their high electronic density, CdSe platelets appear very dark.

## A.4 Other technical details

### A.4.1 Spectroscopy

UV VIS absorption spectra were acquired using a CARY 5000 spectrophotometer while a HORIBA JOBIN YVON FLUOROMAX 4 was used for fluorescence spectra.

### A.4.2 Zeta potential measurements

: Electrophoretic mobilities of platelets were measured using a Malvern Zeta sizer equipped with a dip-cell. Conversion from mobilities to  $\zeta$ -potential were made assuming the Huckel approximation i.e.  $\mu = \frac{\zeta \epsilon \epsilon_0}{\eta}$ .

### A.4.3 Colloidal stability

: The colloidal stability of the dispersions was assessed by measuring the absorbance of nanoplatelets at 400 nm using an Agilent Cary 5000 spectrophotometer. A weighted amount of platelet is dispersed in hexane through sonication until a clear solution is obtained. Absorbance spectra are then measured at regular intervals. The reported values were normalized to the starting optical density. Unless otherwise stated, all the studies were performed in hexane. During these experiments, no special care was taken to avoid contact with air.

### A.4.4 Fluorescence microscopy

In chapter 3, the nanoplatelet supraparticles contained in a thin glass capillary were imaged in epifluorescence through a 60x objective. The fluorescence is separated between the two polarization components which are both imaged on a CCD camera. More details on the optical set-up can be found in ref [160].

In chapter 5, the threads were imaged using a LEICA SP7 scanning confocal microscope with a 60x objective.

## Curriculum vitae

<b>Name</b>	Benjamin Abécassis
<b>Research ID</b>	B-5881-2008
<b>Date and place of birth</b>	15 mai 1978 in Chenove (21), France
<b>Nationality</b>	French
<b>Adress</b>	Laboratoire de Physique des Solides UMR 8502 - Batiment 510 Université Paris Sud 91405 Orsay, France
<b>Marital status</b>	Civil partnership, 2 kids (twins born in 2013)
<b>Phone</b>	+33 1 69 15 53 94
<b>email</b>	benjamin.abecassis@u-psud.fr
<b>web</b>	<a href="http://chercheurs.lps.u-psud.fr/abecassis/">http://chercheurs.lps.u-psud.fr/abecassis/</a>

### Education

**2003-2006:** PhD Ecole Polytechnique and french atomic commission (CEA), with highest honors. Supervisors: F. Testard and O. Spalla.

**2003:** Master of Science in Soft Matter, Université Paris 6. Internship at ANSTO, Sydney, Australia.

**2002:** Master of Engineering, Chimie Paristech, Paris. Internship at EDF China (Beijing and Laibin in Guang Xi)

**1999-2002:** Undergraduate studies in Chemistry at Chimie Paritech, selective chemical engineering college.

**1996-1999:** French “classes préparatoires”, intensive math, chemistry, physics for competitive entrance at “grandes écoles”.

### Positions

**since 12/2010 :** CNRS research fellow, Laboratoire de Physique des Solides, Orsay.

**09/2009-12/2010 :** Associate Researcher, MMN Lab (ESPCI, Paris), P. Tabeling’s group.



03/2008-08/2009 : Post-doctoral fellow at CEA LETI (Grenoble).

01/2007-12/2007 : Post-doctoral fellow at LPMCN, (Université de Lyon), L. Bocquet's group.

## Fellowships and awards

2012: Junior chair of LABEX Palm on the "Self-Assembly of quantum Nanoplatelets".

2012: CNRS Prime d'excellence scientifique (prize for scientific excellence).

2003-2006: PhD fellowship of the french atomic commission (CEA).

2003: Merit scholarship for Masters in science.

## Supervision of graduate students and postdoctoral fellows

- 2 post docs : Anaïs Lehoux (2013, now post doc in Japan) and Santanu Jana (2014-2016 and 2016-2018).
- 1 PhD student (Nicolo Castro : 2013-2016).
- 5 masters students.

## Teaching activities

from 2010: Teaching small angle scattering at ESPCI, Paris.

2009: Teaching sol-gel chemistry at Chimie Paritech.

2006: Teaching basic lab techniques at Université Paris 6. 2003: Oral interrogation in Chemistry "Classes Préparatoires".

## Collective responsibilities

- Since 2011: Organizer of the soft matter seminar of the Laboratoire de Physique des Solides (20 seminars per year).
- Responsible for several scientific instruments including a SAXS/WAXS instrument open to numerous users.

## Reviewing activities

- Reviewer for the following journals: *Science*, *Nature Communications*, *Advanced Functional Materials*, *Advanced Science*, *RSC Advances*, *Chemistry of Materials*, *Langmuir*, *Journal of Physical Chemistry*, *Nanoscale*, *Nano Research*, *Physical Chemistry Chemical Physics*, *Chemical Engineering Science*, *European Physics Letters*, *Physics of Fluids*.
- Reviewer of grants for the Polish funding agency, NWO (Dutch funding agency), the MICHEM Labex.

## Funding as principal investigator

- Marie Curie Individual Fellowship for S. Jana: 300 k€
- Junior Chair LABEX PALM: 250 k€
- “Young team” CNRS : 35 k€
- Attractivité Paris-Sud Orsay : 30 k€
- RTRA, Triangle de la physique : 35 k€

## List of publications and communications

### Publications

1. **Abécassis, B.**, Testard, F.\* , Zemb, T., Berthon, L. & Madic, C. Effect of n-Octanol on the Structure at the Supramolecular Scale of Concentrated Dimethyldioctylhexylethoxy-malonamide Extractant Solutions. *Langmuir* 6638-6644 (2003).
2. **Abécassis, B.\*** et al. Phase behavior, topology, and growth of neutral catanionic reverse micelles. *Langmuir* 22, 8017-28 (2006).
3. **Abécassis, B.\*** et al. Electrostatic control of spontaneous curvature in catanionic reverse micelles. *Langmuir* 23, 9983-9 (2007).
4. **Abécassis, B.**, Testard, F., Spalla, O.\* & Barboux, P. Probing in situ the nucleation and growth of gold nanoparticles by small-angle X-ray scattering. *Nano Lett.* 7, 1723-7 (2007).
5. **Abécassis, B.**, Cottin-Bizonne, C., Ybert, C., Ajdari, A. & Bocquet, L.\* Boosting migration of large particles by solute contrasts. *Nature Materials.* 7, 785-9 (2008). **Highlighted by D.C. Prieve in a News and Views.**
6. **Abécassis, B.**, Testard, F. & Spalla, O.\* Gold Nanoparticle Superlattice Crystallization Probed In Situ. *Phys. Rev. Lett.* 100, 115504 (2008).
7. Testard, F.\* , Bauduin, P., Martinet, L., **Abécassis, B.**, Berthon, L., Madic, C., & Zemb, T. Self-assembling properties of malonamide extractants used in separation processes. *Radiochim. Acta* 96, (2008).
8. **Abécassis, B.**, Cottin-Bizonne, C., Ybert, C., Ajdari, A. & Bocquet, L.\* Osmotic manipulation of particles for microfluidic applications. *New J. Phys.* 11, 075022 (2009).
9. **Abécassis, B.\*** , Testard, F. & Zemb, T. Gold nanoparticle synthesis in worm-like catanionic micelles: microstructure conservation and temperature induced recovery. *Soft Matter* 5, 974 (2009).

10. **Abécassis, B.**, Testard, F., Kong, Q., Francois, B. & Spalla, O. \* Influence of monomer feeding on a fast gold nanoparticles synthesis: time-resolved XANES and SAXS experiments. *Langmuir* 26, 13847-54 (2010).
11. Palacci, J., **Abécassis, B.**, Cottin-Bizonne, C., Ybert, C. & Bocquet, L. \* Colloidal Motility and Pattern Formation under Rectified Diffusiophoresis. *Phys. Rev. Lett.* 104, 138302 (2010).
12. Nghe, P., Terriac, E., Schneider, M., Li, Z.Z., Cloitre, M., **Abecassis, B.**, Tabeling, P. \*, Microfluidics and complex fluids. *Lab Chip* 11, 788-94 (2011).
13. **Abécassis, B.**\* et al. Aqueous suspensions of GdPO<sub>4</sub> nanorods: a paramagnetic mineral liquid crystal. *J. Phys. Chem. B* 116, 7590-5 (2012).
14. Tessier, M.D., Biadala, L., Bouet, C., Ithurria, S., **Abécassis, B.**, & Dubertret, B. \* Phonon Line Emission Revealed by Self-Assembly of Colloidal Nanoplatelets. *ACS Nano* 7, 3332-3340 (2013).
15. Bouet, C., Mahler, B., Nadal, B., **Abécassis, B.**, Tessier, M.D., Ithurria, S., Xu, X.Z., Dubertret, B. Two-Dimensional Growth of CdSe Nanocrystals, from Nanoplatelets to Nanosheets. *Chem. Mater.* 25, 639-645 (2013).
16. Pedetti, S., Nadal, B., Lhuillier, E., Mahler, B., Bouet, C., **Abécassis, B.**, Xu, X.Z., Dubertret, B. \*, Optimized synthesis of CdTe nanoplatelets and photo-response of CdTe nanoplatelets films. *Chem. Mater.* 25, 2455-2462 (2013).
17. **Abécassis, B.**\*, Tessier, M. D., Davidson, P. & Dubertret, B. Self-Assembly of CdSe Nanoplatelets into Giant Micrometer-Scale Needles Emitting Polarized Light. *Nano Lett.*, 14, 710-715, (2014).
18. Slyusarenko, K., Constantin, D. \*, **Abécassis, B.**, Davidson, P. & Chanéac, C. Infrared dichroism of gold nanorods controlled using a magnetically addressable mesophase. *J. Mater. Chem. C*, 2, 5087-5092 (2014).
19. Slyusarenko, K., **Abécassis, B.**, Davidson, P., Constantin, D., Morphology of gold nanoparticles determined by full-curve fitting of the light absorption spectrum. Comparison with X-ray scattering and electron microscopy data. *Nanoscale*, 6, 13527-13534, 2014.
20. E. Beaudoin\*, **B. Abécassis**, D. Constantin, J. Degrouard, P. Davidson. Strain-controlled fluorescence polarization in a CdSe nanoplatelet-block copolymer composite. *Chem. Commun.*, 51, 4051-4054, 2015.
21. **B. Abécassis\***, C. Bouet, C. Garnero, D. Constantin, N. Lequeux, S. Ithurria, B.

Dubertret, B. R. Pauw, D. Pontoni. Real-Time in Situ Probing of High-Temperature Quantum Dots Solution Synthesis. *Nano Letters*, 15, 4, 2015

22. S. Jana, T. Phan, C. Bouet, M.D. Tessier, P. Davidson, B. Dubertret, **B. Abécassis\*** Stacking and colloidal stability of CdSe nanoplatelets *Langmuir*, 31, 10532-10539, 2015.

23. G. Izzet\*, A. Macdonell, C. Rinfray, M. Piot, S. Renaudineau, E. Derat, **B. Abécassis**, C. Afonso, Anna Proust. Metal-directed self-assembly of a covalent polyoxometalate-based molecular triangle: using powerful analytical tools to probe the chemical structure of complex supramolecular assemblies. *Chemistry - A European Journal*. in press, 2015.

24. **B. Abécassis\***, Three-dimensional self assembly of semi-conducting colloidal nanocrystals: from fundamental forces to collective optical properties. Invited review *Chem Phys Chem* in press, 2016.

25. G. Izzet, **Benjamin Abécassis**, D. Brouri, M. Piot, B. Matt, C.Bo, S. Serapian and Anna Proust, Hierarchical self-assembly of polyoxometalate-based hybrids driven by metal coordination and electrostatic interactions: from discrete supramolecular species to nanoparticles-like assemblies, in press (J. Am. Chem. Soc.).

26. S. Jana, P. Davidson, **B. Abécassis\***. CdSe Nanoplatelets Living Polymers, under review (Angewandte Chemie, International Edition)

27. O.Taché, S. Rouziere, P. Joly, M. Salah Amara, B. Fleury, A. Thill, F. Testard, P. Launois, O. Spalla and **B. Abécassis\***, MOMAC: A SAXS/WAXS laboratory instrument dedicated to nanomaterials, submitted (Journal of Applied Crystallography)

## Oral communications

### Oral communications at international conferences

- Condensed matter day of the french Physical Society, Nancy, 2004.
- ECIS, (European Colloid and Interface Society), Geilo, Norway, 2005.
- French-German network, Goettingen, Germany, Décembre 2005.
- 80th American Chemical Society Symposium on Colloid and Interface Science , Boulder, USA, 2006.
- First european conference on microfluidics, Bologna, Italy, 2008.
- NANAX 6, Bad Hofgastein, Austria, 2014.
- MRS Spring Meeting, San Fransisco, 2015.
- Small Angle Scattering International Conference, Berlin, 2015.

### Oral communications at national conferences

- Journée de la matiere condensée, SFP, Nancy, 2005. - SOLEIL user Meeting, Palaiseau, 2015. - Rayons X et Matière, Grenoble, 2015.

### Poster

- Dynamic phenomena in soft matter, 16th ESRF user meeting, 2006.

- International Soft Matter Conference, Aix-La-Chapelle, 2007.
- Liquid Crystals french conference, Rennes, 2011.

#### **Seminars and workshops**

- Physique de la Matière Condensée, Ecole Polytechnique, 2006.
- Laboratoire du Futur (Rhodia/CNRS), Bordeaux, 2006.
- Oxford University, Theory of Soft and Biological Matter, Department of Chemistry, 2007.
- Matière et Système Complexe (MSC), Université Paris 7, 2007.
- C'nano Ile de France, 2008
- LIONS, CEA Saclay, 2008
- DTBS, LETI, CEA Grenoble, 2008
- Workshop on nano-micro fluidics, Lyon, 2008
- PMMH, ESPCI, Paris, 2008.
- MMC, ESPCI, Paris, Juillet 2009.
- Laboratoire de Physique des Solides, Université Paris 11, 2010.
- Colloque Bouyssy, Université Paris Sud, 2011.
- Laboratoire Photonique et Nanostructures, Marcoussis, France, 2012.
- LPEM, ESPCI, Paris, 2012.
- CREE Saint-Gobain, Cavaillon, France, 2013. - LPEM, ESPCI, Paris, 2014.
- CNAM, Paris, France, 2015. - LPEM, ESPCI, Paris, 2016.